

University of Windsor

Scholarship at UWindor

Electronic Theses and Dissertations

Theses, Dissertations, and Major Papers

1995

A study of thin solid organic films by Fourier transform surface-enhanced Raman scattering and atomic force microscopy.

Carol Ann. Jennings
University of Windsor

Follow this and additional works at: <https://scholar.uwindsor.ca/etd>

Recommended Citation

Jennings, Carol Ann., "A study of thin solid organic films by Fourier transform surface-enhanced Raman scattering and atomic force microscopy." (1995). *Electronic Theses and Dissertations*. 822.
<https://scholar.uwindsor.ca/etd/822>

This online database contains the full-text of PhD dissertations and Masters' theses of University of Windsor students from 1954 forward. These documents are made available for personal study and research purposes only, in accordance with the Canadian Copyright Act and the Creative Commons license—CC BY-NC-ND (Attribution, Non-Commercial, No Derivative Works). Under this license, works must always be attributed to the copyright holder (original author), cannot be used for any commercial purposes, and may not be altered. Any other use would require the permission of the copyright holder. Students may inquire about withdrawing their dissertation and/or thesis from this database. For additional inquiries, please contact the repository administrator via email (scholarship@uwindsor.ca) or by telephone at 519-253-3000ext. 3208.



National Library
of Canada

Bibliothèque nationale
du Canada

Acquisitions and
Bibliographic Services Branch

Direction des acquisitions et
des services bibliographiques

395 Wellington Street
Ottawa, Ontario
K1A 0N4

395, rue Wellington
Ottawa (Ontario)
K1A 0N4

Your file Votre référence

Our file Notre référence

NOTICE

The quality of this microform is heavily dependent upon the quality of the original thesis submitted for microfilming. Every effort has been made to ensure the highest quality of reproduction possible.

If pages are missing, contact the university which granted the degree.

Some pages may have indistinct print especially if the original pages were typed with a poor typewriter ribbon or if the university sent us an inferior photocopy.

Reproduction in full or in part of this microform is governed by the Canadian Copyright Act, R.S.C. 1970, c. C-30, and subsequent amendments.

AVIS

La qualité de cette microforme dépend grandement de la qualité de la thèse soumise au microfilmage. Nous avons tout fait pour assurer une qualité supérieure de reproduction.

S'il manque des pages, veuillez communiquer avec l'université qui a conféré le grade.

La qualité d'impression de certaines pages peut laisser à désirer, surtout si les pages originales ont été dactylographiées à l'aide d'un ruban usé ou si l'université nous a fait parvenir une photocopie de qualité inférieure.

La reproduction, même partielle, de cette microforme est soumise à la Loi canadienne sur le droit d'auteur, SRC 1970, c. C-30, et ses amendements subséquents.

Canada

**A STUDY OF THIN SOLID ORGANIC FILMS BY FOURIER TRANSFORM
SURFACE-ENHANCED RAMAN SCATTERING
AND ATOMIC FORCE MICROSCOPY**

by

Carol Ann Jennings

**A Dissertation
Submitted to the Faculty of Graduate Studies
and Research Through the Department of Chemistry and Biochemistry
in Partial Fulfillment of the Requirements
for the Degree of Doctor of Philosophy
at the University of Windsor**

Windsor, Ontario, Canada

1994

(c) 1994 Carol Ann Jennings



National Library
of Canada

Acquisitions and
Bibliographic Services Branch

395 Wellington Street
Ottawa, Ontario
K1A 0N4

Bibliothèque nationale
du Canada

Direction des acquisitions et
des services bibliographiques

395, rue Wellington
Ottawa (Ontario)
K1A 0N4

Your file Votre référence

Our file Notre référence

THE AUTHOR HAS GRANTED AN
IRREVOCABLE NON-EXCLUSIVE
LICENCE ALLOWING THE NATIONAL
LIBRARY OF CANADA TO
REPRODUCE, LOAN, DISTRIBUTE OR
SELL COPIES OF HIS/HER THESIS BY
ANY MEANS AND IN ANY FORM OR
FORMAT, MAKING THIS THESIS
AVAILABLE TO INTERESTED
PERSONS.

L'AUTEUR A ACCORDE UNE LICENCE
IRREVOCABLE ET NON EXCLUSIVE
PERMETTANT A LA BIBLIOTHEQUE
NATIONALE DU CANADA DE
REPRODUIRE, PRETER, DISTRIBUER
OU VENDRE DES COPIES DE SA
THESE DE QUELQUE MANIERE ET
SOUS QUELQUE FORME QUE CE SOIT
POUR METTRE DES EXEMPLAIRES DE
CETTE THESE A LA DISPOSITION DES
PERSONNE INTERESSEES.

THE AUTHOR RETAINS OWNERSHIP
OF THE COPYRIGHT IN HIS/HER
THESIS. NEITHER THE THESIS NOR
SUBSTANTIAL EXTRACTS FROM IT
MAY BE PRINTED OR OTHERWISE
REPRODUCED WITHOUT HIS/HER
PERMISSION.

L'AUTEUR CONSERVE LA PROPRIETE
DU DROIT D'AUTEUR QUI PROTEGE
SA THESE. NI LA THESE NI DES
EXTRAITS SUBSTANTIELS DE CELLE-
CI NE DOIVENT ETRE IMPRIMES OU
AUTREMENT REPRODUITS SANS SON
AUTORISATION.

ISBN 0-612-01456-8

Canada

Name CAROL ANN JENNINGS

Dissertation Abstracts International is arranged by broad, general subject categories. Please select the one subject which most nearly describes the content of your dissertation. Enter the corresponding four-digit code in the spaces provided.

PHYSICAL SCIENCES/CHEMISTRY/PHYSICAL
SUBJECT TERM

0494 U-M-I
SUBJECT CODE

Subject Categories

THE HUMANITIES AND SOCIAL SCIENCES

COMMUNICATIONS AND THE ARTS

Architecture 0729
Art History 0377
Art 0900
Cinema 0378
Dance 0357
Fine Arts 0373
Information Science 0723
Journalism 0391
Library Science 0399
Mass Communications 0708
Music 0413
Speech Communication 0459
Theater 0465

EDUCATION

General 0515
Administration 0514
Adult and Continuing 0516
Agricultural 0517
Art 0273
Bilingual and Multicultural 0282
Business 0688
Community College 0275
Curriculum and Instruction 0727
Early Childhood 0518
Elementary 0524
Finance 0277
Guidance and Counseling 0519
Health 0680
Higher 0745
History of 0520
Home Economics 0278
Industrial 0521
Language and Literature 0279
Mathematics 0280
Music 0522
Philosophy of 0998
Physical 0523

Psychology 0525
Reading 0535
Religious 0527
Sciences 0714
Secondary 0533
Social Sciences 0534
Sociology of 0340
Special 0529
Teacher Training 0530
Technology 0710
Tests and Measurements 0288
Vocational 0747

LANGUAGE, LITERATURE AND LINGUISTICS

Language 0679
General 0289
Ancient 0290
Linguistics 0291
Modern 0401
Literature 0294
General 0295
Classical 0297
Comparative 0298
Medieval 0316
Modern 0591
African 0305
American 0352
Asian 0355
Canadian (English) 0593
Canadian (French) 0311
English 0312
Germanic 0315
Latin American 0313
Middle Eastern 0314
Romance 0314
Slavic and East European 0314

PHILOSOPHY, RELIGION AND THEOLOGY

Philosophy 0422
Religion 0318
General 0321
Biblical Studies 0319
Clergy 0320
History of 0322
Philosophy of 0469
Theology 0323

SOCIAL SCIENCES

American Studies 0323
Anthropology 0324
Archaeology 0326
Cultural 0327
Physical 0310
Business Administration 0272
General 0770
Accounting 0454
Banking 0338
Management 0385
Marketing 0501
Canadian Studies 0503
Economics 0505
General 0508
Agricultural 0509
Commerce-Business 0510
Finance 0511
History 0358
Labor 0366
Theory 0351
Folklore 0578
Geography 0578
Gerontology 0578
History 0578
General 0578

Ancient 0579
Medieval 0581
Modern 0582
Black 0328
African 0331
Asia, Australia and Oceania 0332
Canadian 0334
European 0335
Latin American 0336
Middle Eastern 0337
United States 0585
History of Science 0398
Law 0615
Political Science 0616
General 0617
International Law and Relations 0814
Public Administration 0452
Recreation 0626
Social Work 0627
Sociology 0938
General 0631
Criminology and Penology 0628
Demography 0629
Ethnic and Racial Studies 0630
Individual and Family Studies 0700
Industrial and Labor Relations 0344
Public and Social Welfare 0709
Social Structure and Development 0999
Theory and Methods 0453
Transportation 0999
Urban and Regional Planning 0453
Women's Studies 0453

THE SCIENCES AND ENGINEERING

BIOLOGICAL SCIENCES

Agriculture 0473
General 0285
Agronomy 0475
Animal Culture and Nutrition 0476
Animal Pathology 0359
Food Science and Technology 0478
Forestry and Wildlife 0479
Plant Culture 0480
Plant Pathology 0817
Plant Physiology 0777
Range Management 0746
Wood Technology 0306
Biology 0287
General 0308
Anatomy 0309
Biostatistics 0379
Botany 0329
Cell 0353
Ecology 0369
Entomology 0793
Genetics 0410
Limnology 0307
Microbiology 0317
Molecular 0416
Neuroscience 0433
Oceanography 0821
Physiology 0778
Radiation 0472
Veterinary Science 0786
Zoology 0760
Biophysics 0425
General 0996
Medical 0996

Geodesy 0370
Geology 0372
Geophysics 0373
Hydrology 0388
Mineralogy 0411
Paleobotany 0345
Paleoecology 0426
Paleontology 0418
Paleozoology 0985
Palynology 0427
Physical Geography 0368
Physical Oceanography 0415

HEALTH AND ENVIRONMENTAL SCIENCES

Environmental Sciences 0768
Health Sciences 0566
General 0300
Audiology 0992
Chemotherapy 0567
Dentistry 0350
Education 0769
Hospital Management 0758
Human Development 0982
Immunology 0564
Medicine and Surgery 0347
Mental Health 0569
Nursing 0570
Nutrition 0380
Obstetrics and Gynecology 0354
Occupational Health and Therapy 0381
Ophthalmology 0571
Pathology 0419
Pharmacology 0572
Pharmacy 0382
Physical Therapy 0573
Public Health 0574
Radiology 0575
Recreation 0575

Speech Pathology 0460
Taxiology 0383
Home Economics 0386

PHYSICAL SCIENCES

Pure Sciences 0485
Chemistry 0749
General 0486
Agricultural 0487
Analytical 0488
Biochemistry 0738
Inorganic 0490
Nuclear 0491
Organic 0494
Physical 0495
Polymer 0754
Radiation 0405
Mathematics 0605
Physics 0986
General 0606
Acoustics 0608
Astronomy and Astrophysics 0748
Atmospheric Science 0607
Atomic 0798
Electronics and Electricity 0759
Elementary Particles and High Energy 0609
Fluid and Plasma 0610
Molecular 0752
Nuclear 0611
Optics 0463
Radiation 0346
Solid State 0984
Statistics 0984
Applied Sciences 0346
Applied Mechanics 0984
Computer Science 0984

Engineering 0537
General 0538
Aerospace 0539
Agricultural 0540
Automotive 0541
Biomedical 0542
Chemical 0543
Civil 0544
Electronics and Electrical 0348
Heat and Thermodynamics 0545
Hydraulic 0546
Industrial 0547
Marine 0794
Materials Science 0548
Mechanical 0743
Metallurgy 0551
Mining 0552
Nuclear 0549
Packaging 0765
Petroleum 0554
Sanitary and Municipal 0790
System Science 0428
Geotechnology 0796
Operations Research 0795
Plastics Technology 0994
Textile Technology 0994

PSYCHOLOGY

General 0621
Behavioral 0384
Clinical 0622
Developmental 0620
Experimental 0623
Industrial 0624
Personality 0625
Physiological 0989
Psychobiology 0349
Psychometrics 0632
Social 0451



ABSTRACT:

Fourier transform surface-enhanced Raman scattering (FT-SERS) in the near-infrared and atomic force microscopy (AFM) have been used to characterize thin solid organic films. The pigments studied were phthalocyanines and perylenes which have applications as charge generation materials in organic photoreceptors. Techniques for film preparation such as Langmuir-Blodgett (LB) deposition and vacuum evaporation are discussed. The literature was reviewed for FT-Raman spectroscopy, surface-enhanced Raman spectroscopy and atomic force microscopy. A model according to Gersten and Nitzan was applied and SERS enhancement factors in the near-IR were calculated for various metal hemi-spheroids. FT-Raman spectra were presented for thin vacuum evaporated films of titanyl phthalocyanine (TiOPc) and vanadyl phthalocyanine (VOPc) prepared on glass substrates held at a range of temperatures during deposition. The frequencies were assigned and different polymorphic forms were apparent. In order to improve the signal intensity, thin films were deposited on metal substrates which produced SERS in the near-IR. The substrates selected for FT-SERS were vacuum evaporated metal island films of copper and gold of 20 nm mass thickness prepared with the glass substrate held at 200°C. Thin films of 3 nm mass thickness of VOPc and 3,4:9,10-perylenetetracarboxylic dianhydride (PTCDA) were vacuum evaporated onto the metal island substrates and produced FT-SERS with an enhancement factor of approximately 100. Single Langmuir-Blodgett monolayers of phthalocyanines and perylenes on the metal island substrates gave FT-SERS. The FT-SERS spectra of vacuum evaporated films and LB monolayers were compared with visible laser excitation. Phthalocyanines and

perylene absorb in the visible region and produced surface-enhanced resonance Raman scattering (SERRS). The morphology and structure of single LB monolayers on mica and Si(111) wafers have been determined using atomic force microscopy. AFM results for a perylene on Si(111) showed good agreement with the orientation inferred from reflection-absorption infrared spectroscopy and transmission IR measurements.

ACKNOWLEDGEMENTS

I would like to express sincere thanks to my two supervisors: Dr. R. Aroca from the University of Windsor and Dr. G. J. Kovacs of the Xerox Research Centre of Canada.

Xerox Corporation should be acknowledged for financial support and its commitment to employee training and development. In particular, senior staff and area managers have been very supportive at XRCC. I also thank NSERC of Canada for financial support.

Dr. H. Mizes of Webster Research Center provided technical assistance and suggestions related to atomic force microscopy. Dr. K. Kjoller and Mr. C. Callahan of Digital Instruments are acknowledged for images obtained on the Nanoscope III MultiMode AFM. Mr. P. Gerroir of XRCC with Mr. J. Cole and Mr. D. Edgar of Nissei Sangyo supplied the field emission scanning electron micrograph of a gold film. Dr. C. Tripp of XRCC made the initial proposal for an FT-Raman system and gave useful advice. Mr. C. K. Hsaio of XRCC is acknowledged for his comments and assistance regarding the section on polymorphs of titanyl and vanadyl phthalocyanine. I thank Dr. T. Sluhs of Xerox for the X-ray powder diffraction patterns of titanyl phthalocyanine polymorphs.

Finally, I would like to thank my fiancé, family, friends and colleagues who provided moral support throughout this endeavor.

TABLE OF CONTENTS

	Page
Abstract	iii
Acknowledgements	v
List of Tables	viii
List of Figures	ix
List of Abbreviations	xiii
1. Introductory Remarks, Electrophotography and Objectives	
1. Introductory Remarks	1
2. Electrophotography and Organic Photoconductors	2
3. Objectives	11
<i>Chapter 1 References</i>	15
2. Experimental Techniques (Background): Film Deposition, Raman Spectroscopy and Atomic Force Microscopy	
1. Langmuir-Blodgett Films	16
2. Vacuum Evaporated Films	29
3. Raman Spectroscopy Theory	
3.1 Normal Raman	32
3.2 Polarizations of Light	38
3.3 Resonance Raman	41
3.4 FT-Raman	43
4. Atomic Force Microscopy	48
<i>Chapter 2 References</i>	54
3. Surface-Enhanced Raman Scattering (SERS) and Model Calculations of Enhancement Factors	
1. Introduction	62
2. Electromagnetic Theory for SERS	65
3. Non-Electromagnetic Theories for SERS	68
4. Distance and Coverage Dependence of SERS Enhancement Factor	73
5. Surface-Selection Rules	75
6. Model Calculations of SERS Enhancement Factors	80
<i>Chapter 3 References</i>	89
4. FT-Raman Spectroscopy of Thin Films of Titanyl Phthalocyanine and Vanadyl Phthalocyanine	
1. Introduction	93

	Page
2. Experimental	
2.1 Preparation of TiOPc, VOPc and Vacuum Evaporation of Films	99
2.2 X-Ray Powder Diffraction	100
2.3 FT-Raman Spectroscopy	101
3. Results and Discussion	101
4. Conclusions	113
<i>Chapter 4 References</i>	114
5. FT-SERS of Evaporated Films and Langmuir-Blodgett Monolayers	
1. Introduction	116
2. Experimental	120
2.1 Vacuum Evaporation of Metal Island Films and Thin Organic Films	122
2.2 Preparation of Nonmetallic Substrates	122
2.3 Preparation of Langmuir-Blodgett Films	123
2.4 Raman Systems and UV-Visible Spectrophotometer	125
3. Results and Discussion	131
3.1 SERS-active Surfaces for the Near-IR	138
3.2 UV-Vis absorption spectra of VOPc and PTCDA. FT-SERS on gold island films.	144
3.3 Comparison of Near-Infrared FT-SERS and Visible SERS for VOPc and PTCDA on gold films	147
3.4 FT-SERS of Thin Vacuum Evaporated VOPc Films on Cu Islands and Semiconductors	158
3.5 FT-SERS of Single LB Monolayers on Copper and Gold Island Films.	159
4. Conclusions	159
<i>Chapter 5 References</i>	
6. Spectroscopy and Atomic Force Microscopy of Langmuir-Blodgett Monolayers	
1. Introduction	162
2. Experimental Procedures	169
2.1 Preparation of Substrates and Langmuir-Blodgett Films	172
2.2 FTIR Spectrometer and Reflection-Absorption Measurements	172
2.3 Park Scientific AFM	173
2.4 Digital Instruments Nanoscope III SPM	173
3. Results and Discussion	194
4. Conclusions	195
<i>Chapter 6 References</i>	
7. Overall Summary and Conclusions. Future Outlook.	198
8. Appendices	203
9. Vita Auctoris	205

LIST OF TABLES

	Page
Table 3-1: Calculated Enhancement Factors for Ag, Au, Cu and Ni at various wavelengths.	85
Table 3-2: Calculated Enhancement Factors for Various Metals at 1064 nm.	86
Table 4-1: FT-Raman Frequencies of Selected TiOPc Polymorphs.	105
Table 4-2: FT-Raman Frequencies and Relative Intensities of VOPc films.	112
Table 5-1: Raman Frequencies and Intensities for vacuum evaporated VOPc and VOPc on Cu.	148

LIST OF FIGURES

	Page
Figure 1-1: A general structure of a photoreceptor showing the conductive substrate, blocking/adhesive layer, charge generator layer and charge transport layer.	7
Figure 1-2: Structure of organic charge generation materials: a) polyazo compound, b) a phthalocyanine, c) a perylene, d) squaraine	9
Figure 1-3: Structure of organic charge generation materials continued: e) dibromoanthanthrone, f) thioquinacridone, g) dithioketopyrrolopyrrole, h) imidazole perinone, i) bis (benzimidazole) perinone, j) pyranthrone	10
Figure 2-1: Schematic of Fromherz circular Langmuir-Blodgett trough. Molecules spread from syringe and compressed. Surface pressure measured using a Wilhelmy plate. Film lift device not shown.	19
Figure 2-2: Surface pressure-area isotherm for arachidic acid. Subphase pH=6.5 and 9.928×10^{-4} M CdCl ₂ . Gaseous phase at large area per molecule not shown. Four distinct phases apparent: liquid-expanded, condensed, solid and collapse.	24
Figure 2-3: a) X-type LB deposition onto a hydrophobic substrate b) Z-type LB deposition onto a hydrophilic substrate c) Y-type LB deposition onto a hydrophilic substrate by withdrawal and dipping.	27
Figure 2-4: Schematic of a typical vacuum evaporation experiment. An organic material or metal is heated in a vacuum chamber and deposited on a substrate. The mass thickness is followed with a quartz crystal thickness monitor.	31
Figure 2-5: Schematic showing vibrational energy levels and photons for elastic Rayleigh scattering, inelastic Stoke's and anti-Stoke's normal Raman scattering.	35
Figure 2-6: The four polarizations of light according to Porto for a ninety degree Raman scattering experiment. The propagation of the laser is along the z-axis. Collection of scattered light is along the x-axis. The four polarizations are: SS, SP, PS and PP. The terms inside the brackets describe the electric field vector of the laser and the electric field vector of the light analyzed after the sample.	40

	Page
Figure 3-1: Prolate hemi-spheroid geometry used for model calculations of SERS enhancement factors.	84
Figure 4-1: Molecular structure of a tetravalent metal-phthalocyanine such as titanyl phthalocyanine (TiOPc) or vanadyl phthalocyanine (VOPc).	96
Figure 4-2: X-ray powder diffraction patterns of TiOPc polymorphs (types I, II, III, & IV).	98
Figure 4-3: FT-Raman spectra of various polymorphs of TiOPc: a) 600 nm amorphous vacuum evaporated film b) type I powder in a melting point capillary tube c) 600 nm type II film and d) type IV powder in a melting point capillary tube	104
Figure 4-4: FT-Raman spectra of 100 nm thick vacuum evaporated TiOPc films prepared at various substrate temperatures.	108
Figure 4-5: FT-Raman spectra of 100 nm thick vacuum evaporated VOPc films prepared at various substrate temperatures.	111
Figure 5-1: Absorption spectrum of a 20 nm Au island film on glass.	128
Figure 5-2: Field emission scanning electron micrography of a 20 nm island film on glass.	130
Figure 5-3: Molecular structure of 3,4:9,10-perylenetetracarboxylic dianhydride (PTCDA).	133
Figure 5-4: Absorption spectrum of a 100 nm evaporated film of VOPc on glass.	135
Figure 5-5: Absorption spectrum of a 100 nm evaporated film of PTCDA on glass.	137
Figure 5-6: (a) FT-Raman spectrum of 200 nm film of VOPc and (b) FT-SERS of a 3 nm film of VOPc on 20 nm Au island film.	140
Figure 5-7: (a) FT-Raman spectrum of 200 nm PTCDA and (b) FT-SERS of 3 nm film of PTCDA on a 20 nm Au island film.	142
Figure 5-8: (a) FT-Raman spectrum of 200 nm VOPc on glass. Laser line 1064.1 nm. (b) SERRS spectrum of 3 nm VOPc on 20 nm Cu. Laser line 647.1 nm. (c) FT-SERS spectrum of 3 nm VOPc on 20 nm Cu. Laser line 1064.1 nm.	146

	Page
Figure 5-9: (a) FT-Raman spectrum of a single LB monolayer of CuTTPc on 20 nm Au. Laser line 1064.1 nm. (b) SERRS spectrum of a single LB monolayer of CuTTPc on 20 nm Au. Laser line 647.1 nm.	151
Figure 5-10: A mixed monolayer of 1:10 PcLuPct / arachidic acid. (a) FT-Raman spectrum on 20 nm Au. Laser line 1064.1 nm. (b) SERRS spectrum on 20 nm Au. Laser line 647.1 nm. (c) SERRS spectrum on 20 nm Cu. Laser line 647.1 nm.	154
Figure 5-11: (a) FT-SERS spectrum of a single LB monolayer of PPTCDE on 20 nm Au. Laser line 1064.1 nm. (b) SERRS spectrum of a single LB monolayer of PPTCDE on 20 nm Au. Laser line 514.5 nm.	156
Figure 6-1: Structures of Langmuir-Blodgett materials. (a) <i>N</i> -hexyl- <i>N'</i> -ethyl-3,4:9,10-perylenetetracarboxylic diimide (HPTCDE). (b) <i>N</i> -hexyl-3,4:9,10-perylenetetracarboxylic monoimide (HPTCO). (c) 1,4,8,11,15,18,22,25-octabutoxy-29H, 31H-phthalocyanine ((BuO) ₈ H ₂ Pc). (d) tetra- <i>tertiary</i> -butyl metal-free phthalocyanine ((t-bu) ₄ H ₂ Pc).	166
Figure 6-2: High resolution image of muscovite mica obtained on a Park Scientific AFM.	175
Figure 6-3: HPTCDE Langmuir-Blodgett monolayer scraped from the mica substrate when the applied force is too large. Park Scientific AFM image.	178
Figure 6-4: HPTCDE Langmuir-Blodgett monolayer on mica imaged with force of 10 nN. Three different heights were observed using the Park Scientific AFM.	180
Figure 6-5: FTIR spectra of HPTCDE in the carbonyl stretching region. The transmission and reflection spectra show the change in relative intensity of the symmetric and antisymmetric C=O stretches.	182
Figure 6-6: AFM image of HPTCDE Langmuir-Blodgett monolayer on Si(111) wafer. Nanoscope III SPM.	186
Figure 6-7: AFM image of HPTCO Langmuir-Blodgett monolayer on Si(111) wafer. Nanoscope III SPM.	188
Figure 6-8: AFM image of (BuO) ₈ H ₂ Pc Langmuir-Blodgett monolayer on Si(111) wafer. Nanoscope III SPM.	191

	Page
Figure 6-9: AFM image of (t-bu) ₄ H ₂ Pc Langmuir-Blodgett monolayer on Si(111) wafer. Nanoscope III SPM.	193

LIST OF ABBREVIATIONS

AFM	atomic force microscopy
ASR	atomic scale roughness
BTA	benzotriazole
(BuO)₈H₂Pc	1,4,8,11,15,18,22,25-octabutoxy-29H,31H-phthalocyanine
CCD	charge-coupled device
CGL	charge generator layer
CT	charge transfer
CT DNA	calf thymus deoxyribonucleic acid
CTL	charge transport layer
CTM	charge transport molecule
CuTTPc	copper tetra- <i>tertiary</i> -butyl-phthalocyanine
DOX	doxorubium
EF	enhancement factor
EM	electromagnetic
FAD	flavine adenine dinucleotide
FT	fourier transform
HPTCDE	<i>N</i> -hexyl- <i>N'</i> -ethyl-3,4:9,10-perylenetetracarboxylic diimide
HPTCO	<i>N</i> -hexyl-3,4:9,10-perylenetetracarboxylic monoimide
HOMO	highest occupied molecular orbital
HOPG	highly oriented pyrolytic graphite
LAM	longitudinal acoustic mode
LB	Langmuir-Blodgett
LUMO	lowest unoccupied molecular orbital
Nc	naphthalocyanine
Nd/YAG	neodymium doped yttrium-aluminum garnet
Nd/YLF	neodymium doped lithium fluoride
NEP	noise equivalent power
ORC	oxidation-reduction cycle
Pc	phthalocyanine
PcLuPct	4,4',4'',4'''-tetra- <i>tertiary</i> -butyl lutetium diphthalocyanine
PMT	photomultiplier tube
PTCDA	3,4:9,10-perylenetetracarboxylic dianhydride
PTCDI	perylenetetracarboxylic diimide
PDCI	<i>N</i> -octyl-3,4-perylene dicarboximide

PPTCDE	<i>N</i> -pentyl- <i>N</i> '-ethyl-3,4:9,10-perylenetetracarboxylic diimide
PTFE	polytetrafluoroethylene
RAIRS	reflection-absorption infrared spectroscopy
RR	resonance Raman
SEM	scanning electron microscopy
SERRS	surface-enhanced resonance Raman scattering
SERS	surface-enhanced Raman scattering
STM	scanning tunneling microscopy
TEM	transmission electron microscopy
TTA	tritolytriazole
(t-bu)₄H₂Pc	tetra- <i>tertiary</i> -butyl metal-free phthalocyanine
UHV	ultrahigh vacuum
XRPD	X-ray powder diffraction

CHAPTER 1: INTRODUCTORY REMARKS, ELECTROPHOTOGRAPHY, AND OBJECTIVES

1.1. INTRODUCTORY REMARKS

The work described here was made possible through the cooperation of the University of Windsor and Xerox Research Centre of Canada. This arrangement has been particularly attractive allowing the author to experience the best of both worlds. The material in this dissertation does not contain any Xerox proprietary information. The background related to electrophotography has been published in the external literature. The experimental chapters were cleared through the legal department and reviewed by scientific staff.

The first chapter explains why thin solid organic films are of interest scientifically and commercially. The objectives of the research are described later in this chapter. Chapter 2 is a general review of the main techniques used in the experimental section. The preparation of thin solid films by Langmuir-Blodgett (LB) deposition and vacuum evaporation are discussed in general terms. Instrumental considerations and theory are presented for Raman spectroscopy, resonance Raman (RR) spectroscopy and FT-Raman spectroscopy. Chapter 2 also contains information about atomic force microscopy (AFM) and an extensive literature review had been conducted prior to carrying out AFM experiments. Chapter 3 is a literature review and presentation of theories for surface-enhanced Raman scattering (SERS). Some model calculations were carried out in Chapter 3 to predict what sort of metals would be suitable to prepare island films for SERS in the near-IR region. Chapter 4 includes FT-

Raman studies carried out on thin vacuum evaporated films of vanadyl phthalocyanine (VOPc) and titanyl phthalocyanine (TiOPc) at various temperatures. In Chapter 5, vacuum evaporated metal island films of copper and gold are prepared and used as FT-SERS active substrates. Thin solid films of organic pigments were deposited on the metal island films by vacuum evaporation. Langmuir-Blodgett monolayers were also deposited on the metals. FT-SERS experiments were carried out using the 1064.1 nm Nd/YAG laser line and surface-enhanced resonance Raman scattering (SERRS) was obtained using visible laser excitation. Following the trend of moving from larger structures to smaller structures, Chapter 6 describes atomic force microscopy (AFM) of Langmuir-Blodgett monolayers on atomically flat substrates. The AFM results were complemented by infrared spectroscopy providing information on molecular orientation. Chapter 7 is an overall summary of the work and ideas on future areas for study are presented.

A brief overview of electrophotography follows and in particular the role of a photoreceptor. The materials used in the experimental section fall under the general category of phthalocyanines and perylenes. Specific compounds from both of the classes have been used in charge generator layers (CGLs) of photoreceptors.

1.2. ELECTROPHOTOGRAPHY AND ORGANIC PHOTO-CONDUCTORS

The inventor of electrophotography was Chester F. Carlson and the original work was described in his patent in 1942¹. This is an example of persistence as Carlson disclosed and demonstrated the crude process to 20 major corporations². There was a lack of interest but eventually development

was carried out at the Battelle Memorial Institute followed by the Halloid Company which became Xerox Corporation². The commercialized process became known as "xerography". Electrophotography is the technology underlying most copiers and printers.

The first step in the xerographic process is photoreceptor charging. Either positive or negative charges can be laid down on the surface of a photoreceptor depending on its composition by corona discharge. An opposite charge is present at the conductive substrate producing an electric field across the photoreceptor. The photoreceptor is imagewise exposed. It is important to couple the wavelength(s) of light for imaging with the spectral sensitivity of the photoreceptor. The areas of the photoreceptor which have been exposed to light discharge due to the creation of electron-hole pairs and charge transport. The areas which have not been exposed, retain the surface charge and replicate the optical image. The charge pattern is called a "latent image". The latent image is developed using charged toner. Toner typically contains pigmented particles in a thermoplastic. A two-component developer consists of carrier beads which transport and charge the toner particles. The electrostatic image on the photoreceptor is developed using toner. A piece of paper is transported and covers the developed area. A charge can be applied to the back of the paper during image transfer to attract the toner. The toner is fused to the paper by heat and/or pressure. The photoreceptor can be cleaned using a blade and any residual charge removed by an intense erase exposure.

A printer requires more computing power than a copier. A digital image is dumped from the computer to the printer. A laser light source projects an

image onto the photoreceptor surface. The lasers which are commonly used emit in the red to near-IR region and most xerographic printers use a rotating polygon². Copier and printer technology draws from many fields; physics, chemistry, engineering and computer science.

One general structure of a photoreceptor is presented in Figure 1-1. A conductive substrate is the starting point in the fabrication. Common substrates are aluminum drums or metallized polyester. A thin layer may be present which blocks charge injection from the conductive layer, smooths out the surface or functions as an adhesive for the next layer. The next layer is the charge generator layer (CGL). A photoactive material is present in a polymeric binder material. A dual-layer photoreceptor has a charge transport layer (CTL) separate from the CGL layer. The charge transport layer commonly contains a charge transport molecule within a polymeric matrix. There could also be an optional overcoat layer to provide abrasion resistance.

Coating techniques for solutions or pigment dispersion have been described³. Photoreceptor coatings are done under highly controlled conditions most commonly on a web or continuous roll format. The coating solution is pumped through a slot and delivered to the web. Important factors to consider are web speed, vibrations, drying conditions, cleanliness and the nature of the coating solution to minimize defects. The charge generator layer can be coated as a dispersion. The pigment particle size must be reduced by milling the pigment with binder in a solvent. There are many devices available to reduce particle size such as ball mills, roller mills, attritors and sand or salt mills³. A less common method for preparing charge generator layers is vacuum evaporation of pigments. Vacuum evaporation allows thin layers of controlled

thickness with few defects to be prepared. The downside is that the evaporated films are usually amorphous and have to be converted to a crystalline state either by heat or solvent treatment³. Methods for coating drums are dip coating, spraying and ring coating.

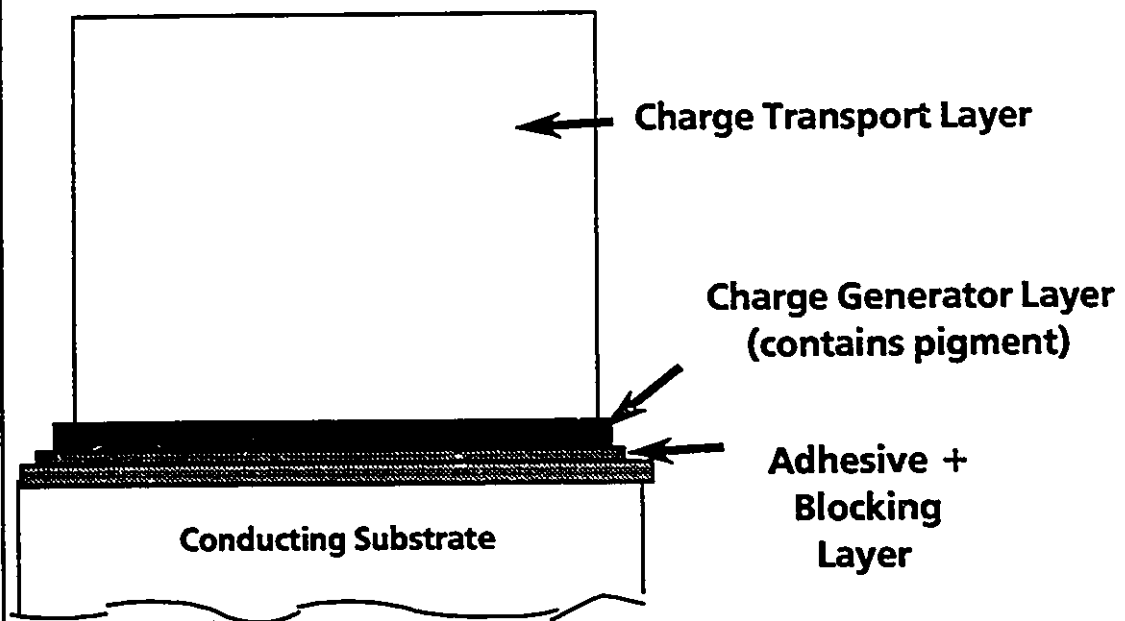
A brief review of organic charge generation materials will be presented. Many of these pigments exhibit polymorphism. The polymorphic form affects the physical properties. It is important to monitor particle size and morphology. The classes of materials are: aggregate materials such as thiapyrylium salts, polyazo compounds, phthalocyanines, squaraines, perylenes and other polycyclic aromatics including dibromoanthanthrone. Representative pigments are shown in Figures 1-2 and 1-3. Azo pigments are named according to the number of azo groups: bis, tris, tetrakis ... and are easily synthesized. A general phthalocyanine structure has a central atom(s) represented by M, where M=H₂, Cu, Mg, Zn, Pb, Sn, TiO, VO, Sn, ClAl, Cl₂Al, ClIn, (OH)₂Ge etc. Depending on the central atom(s), phthalocyanines can have absorbance in both the visible and near-IR regions. Perylenes are usually reddish in appearance and are diimides of 3,4:9,10-perylenetetracarboxylic acid. Squaraines that have aggregated in charge generations layers have absorption in the 400-1000 nm region³. Some further structures of polycyclic charge generation materials appear in Figure 1-3. The crystalline nature of the charge generation material is vital and the tendency to form molecular stacks. It can be seen that the charge generation materials are highly conjugated systems and a number of resonance structures can be drawn.

Two photogeneration mechanisms have been described². A singlet-state exciton can be produced by photon absorption. The electron and hole

Figure 1-1: A general structure of a photoreceptor showing the conductive substrate, blocking/adhesive layer, charge generator layer and charge transport layer.

Figure 1-1

A Photoreceptor Device



Figures 1-2 & 1-3:

Structures of organic charge generation materials^{3,4}: a) polyazo compound, b) a phthalocyanine, c) a perylene, d) a squaraine, e) dibromoanthanthrone, f) thioquinacridone, g) dithioketopyrrolopyrrole, h) imidazole perinone, i) bis(benzimidazole)perinone, j) pyranthrone

Figure 1-2

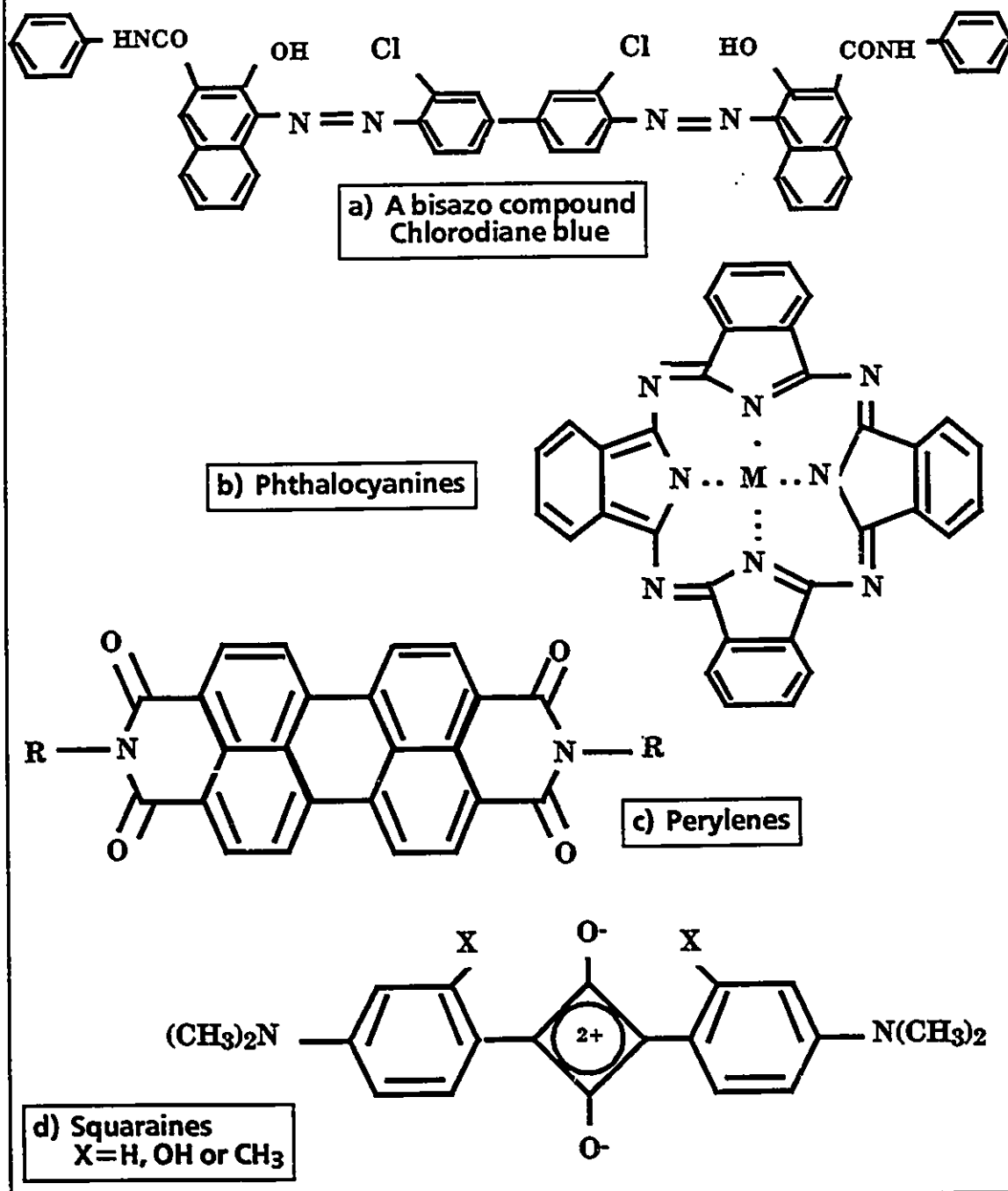
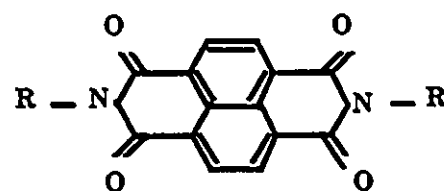
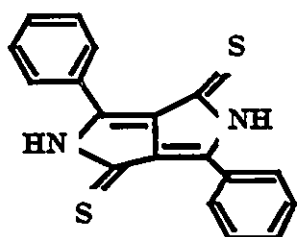
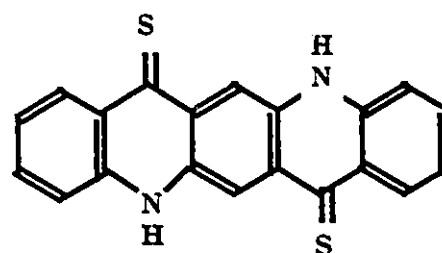
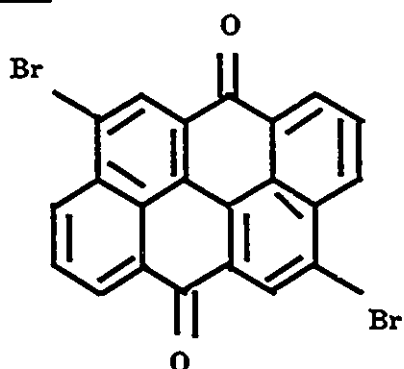
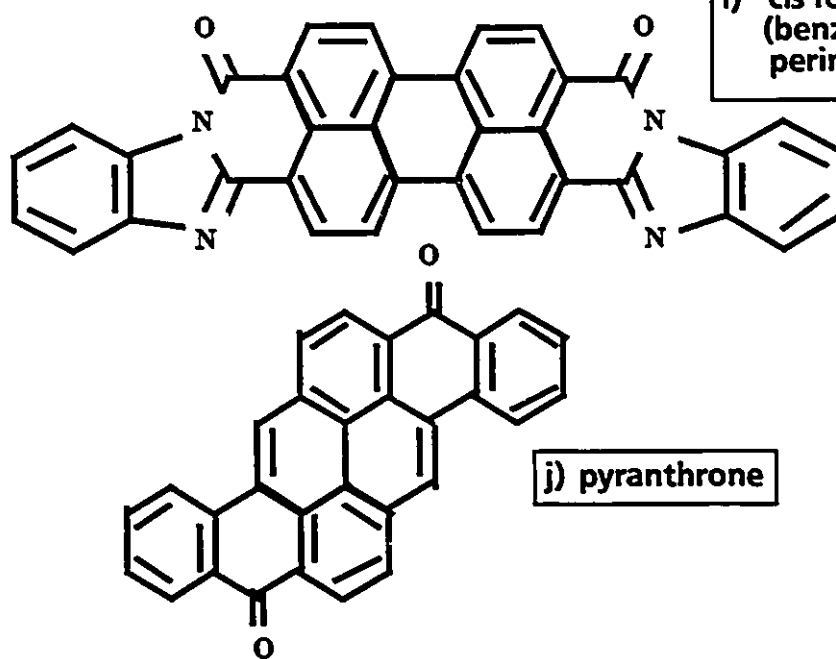


Figure 1-3

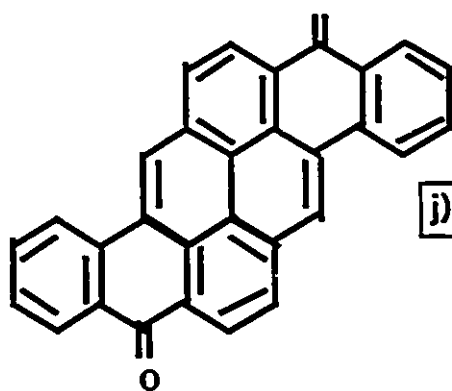


g) dithioketopyrrolopyrrole

h) imidazole perinone



j) pyranthrone



dissociate by an Onsager-like mechanism. Alternatively, the charge migrates to the pigment-particle surface and charge exchange occurs with a charge transport molecule. The charge transport layer (CTL) shown in Figure 1-1 usually consists of a molecular charge transport molecule doped in a polymer. Charge transport molecules (CTMs) are either hole transporting or electron transporting. The hole transport molecules are good electron donors while the electron transport molecules are good electron acceptors. Specific examples of CTMs can be found in the literature²⁻⁴. Some classes of materials used for hole transport include: arylalkanes, arylamines, hydrazones, poly(phenylene-vinylene)s, polysilylenes, polygermylenes, poly(*N*-vinylcarbazole) and pyrazolines. Examples of electron transport materials are: diphenylquinones, 2,4,7-fluorenone and (4-nitro-butoxycarbonyl-9-fluorenylidene) malonitrile.

Photoreceptors are often described by the energy required to discharge to 50% of the original voltage, $E_{1/2}$ having units of ergs/cm². Another parameter often quoted is the dark decay in units of volts/second. The photoreceptor is charged to a desired voltage, undergoes some dark decay and is photodischarged by the appropriate wavelength and intensity of light. A residual voltage remains which is erased by a strong exposure. In practice, a photoreceptor is cycled over a hundred thousand times. The trend has been to produce materials which are more robust and with near-IR photosensitivity for printer applications.

1.3. OBJECTIVES

This author had some previous experience characterizing bulk samples by FT-Raman spectroscopy. In most cases, the technique was relatively easy and reduced fluorescence. Good spectra could be obtained from a variety of

materials often with little or no sample preparation. The challenge was to be able to look at small quantities of material. The first objective of the experimental work was to investigate FT-Raman spectroscopy as a technique for obtaining vibrational information from thin solid films. The approach taken was to prepare vacuum evaporated films of titanyl phthalocyanine and vanadyl phthalocyanine 100 nm thick on glass held at various temperatures. The FT-Raman vibrational frequencies could be assigned to functional groups. Both TiOPc and VOPc exist in a number of polymorphic forms and these could be identified using FT-Raman spectroscopy based on the observed frequencies and relative intensities.

The next goal was to move to ultrathin Langmuir-Blodgett monolayers. Raman scattering from a single LB monolayer is extremely weak due to the small number of molecules and small Raman scattering cross section. Single LB monolayers have been measured using normal Raman spectroscopy with visible laser excitation and a charge-coupled device (CCD). Good FT-Raman spectra could not be obtained for single LB monolayers of phthalocyanines and perylenes with the system used here employing the 1064.1 nm Nd/YAG laser line and an InGaAs detector. Therefore, the objective was to find a way of increasing the FT-Raman signal from an LB monolayer. Since the materials of interest did not have any absorption in the near-IR, the resonance Raman effect could not be used to increase the signal intensity. The method selected to increase the signal intensity from single LB monolayers was Fourier transform surface-enhanced Raman scattering (FT-SERS).

In order to observe FT-SERS, it was necessary to find an appropriate substrate to enhance the Raman signal in the near-IR region for subsequent

deposition and detection of thin organic films. At the time this experimental work was initiated, other groups (cited later), were using electrochemically roughened metal electrodes and metal colloids for FT-SERS. It was decided that the path taken would be to prepare metal island films as FT-SERS active substrates. Computer calculations based on one of the theories for SERS were carried out to estimate enhancement factors for various metals in the near-IR. Vacuum evaporated copper and gold metal island films were prepared of various mass thicknesses. What remained was to demonstrate experimentally that FT-SERS could be obtained of thin organic films on the metal island structures. Initially pigments were vacuum evaporated to a mass thickness of 3 nm on the metal island films. Then single LB monolayers were transferred to the metal island substrates. The greatest enhancement was obtained using 20 nm thick metal island films that had been vacuum evaporated onto glass substrates held at 200°C.

A final objective was to learn about the morphology and structure of Langmuir-Blodgett monolayers of organic pigments using atomic force microscopy. Methods are needed to study aging, defects, domains and local structures in order for LB monolayers to have commercial applications. The structure of an extremely thin film does not necessarily correspond to that of the bulk material and it was thought that AFM would be useful for looking at different polymorphic forms. AFM does not require that the sample be conductive and dimensions ranging from microns to nanometers can be imaged. Initially it was believed that molecular resolution would be achieved but this was not the case. A review of the literature revealed many AFM papers about fatty acids and relatively few results reported for LB monolayers of aromatic organic molecules. Substrates had to be selected for AFM

experiments that were atomically flat and allowed LB film transfer. The best conditions had to be determined for imaging so that the LB monolayer was not scraped from the substrate.

At the time the AFM experiments were carried out, the University of Windsor and the Xerox Research Centre of Canada did not have an AFM instrument. Measurements were made on a Park Scientific AFM instrument at the Xerox Webster Research Center. The author also had the opportunity to take samples to the University of Toronto when representatives from Digital Instruments were visiting. As this dissertation neared completion, the Xerox Research Centre of Canada purchased an AFM instrument. Scanning probe microscopy opens up many possibilities not only for characterization but also in the area of building up structures from the bottom up by manipulating single atoms for instance.

Chapter 1: References

1. Carlson, C. F., U.S. Patent 2,297,691, 1942.
2. Pai, D. M.; Springett, B. E. *Rev. Mod. Phys.* 1993, 65(1), 163.
3. Borsenberger, P.M.; Weiss, D. S. in *Handbook of Imaging Materials*; Diamond, A. S. Ed.; Marcel Dekker, Inc., New York, 1991, pp. 379-446.
4. Borsenberger, P.M.; Weiss, D. S. in *Organic Photoreceptors for Imaging Systems*; Marcel Dekker, Inc., New York, 1993.

CHAPTER 2: EXPERIMENTAL TECHNIQUES (BACKGROUND): FILM DEPOSITION, RAMAN SPECTROSCOPY AND ATOMIC FORCE MICROSCOPY

2.1. LANGMUIR-BLODGETT FILMS

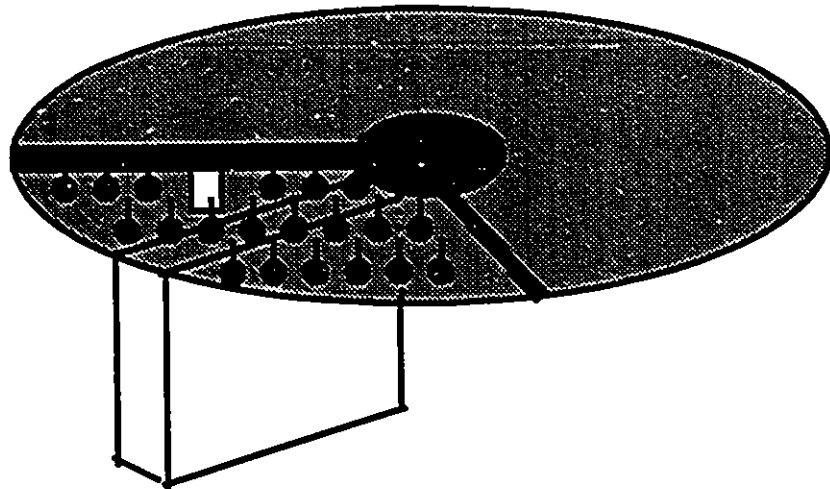
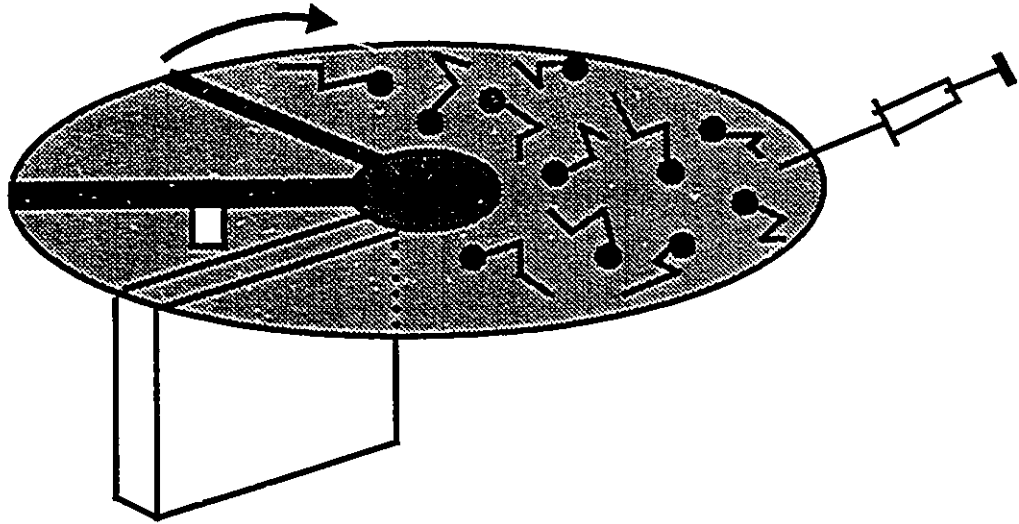
An historical perspective has been given concerning the development of Langmuir-Blodgett (LB) films¹⁻³. It was observed very early on that oil spread on water very thinly and had a calming effect on waves at sea. Lord Rayleigh suspected that olive oil on water had molecular thickness. The surface tension of water was lowered by contaminating oil. Agnes Pockels wrote to Rayleigh about her methods to measure molecular sizes. The set-up used by Pockels was very crude but has similarities to modern day LB troughs. A rectangular trough containing water was used, a tin barrier and a button was the disk to measure surface tension. Pockels produced the first isotherms which are plots of surface pressure versus area. Pockels noted that there were two distinct conditions. In the first situation, the displacement of the barrier had no effect on the surface tension. In the second one, any small change in the barrier markedly affected the surface tension. It is now known that this is due to changes in the orientation of the molecules and packing to form a solid-like state. Others¹ confirmed that materials were spreading to monolayer thickness. Non-polar oils did not behave the same way as polar ones. Irving Langmuir believed the molecular forces were short-ranged. Langmuir received a nobel prize in 1912 for his many contributions to surface science. Langmuir developed a surface film balance among other things. Katharine Blodgett was also on the research staff at General Electric and carried out much of the experimental work.

A monolayer on a liquid surface is a Langmuir film in contrast to built up monolayer assemblies on solid supports known as Langmuir-Blodgett films⁴. Six large international conferences involving LB films have taken place, the last was LB6, the 6th International Conference on Organized Molecular Films in 1993 in Trois-Rivières, Québec, Canada and the papers have been published⁵. An ACS journal exists which is called *Langmuir* and is dedicated to the study of surfaces and colloids.

An account of the steps to prepare a Langmuir-Blodgett film is given here with appropriate examples. The LB trough used in the experiments was a Fromherz trough⁶ shown in Figure 2-1. There are alternate trough designs available commercially which have been described in the literature¹, some of which are rectangular. The Fromherz trough has a circular design and consists of polytetrafluoroethylene (PTFE). Polytetrafluoroethylene is a good material because it can be cleaned using concentrated acid and is resistant to organic solvents. Cleaning of the trough was normally accomplished by soaking the entire PTFE surface with NOCHROMIX® (Godax Laboratories) in concentrated sulfuric acid. The acid was suctioned off using an aspirator with a PTFE tip. The trough was rinsed five times with Milli-Q water with one additional distillation (pH ~6.3). The cleanliness of the water subphase is extremely important for LB work. A laminar flow cabinet and enclosure were used with the trough. The trough was sitting on a terazzo vibration-free table.

The Fromherz trough has two movable barriers which allow a film to be transported if necessary. For the experiments reported here, one barrier was moved. There are two calibrations which were performed. The area enclosed

Figure 2-1: Schematic of Fromherz circular Langmuir-Blodgett trough. Molecules spread from syringe and compressed. Surface pressure measured using a Wilhelmy plate. Film lift device not shown.

Figure 2-1

between the two barriers was easily calibrated with a potentiometer. The total area of the trough was 366 cm². If the two barriers are moved to three and nine o'clock, the area should read 183 cm². The second calibration was for the surface pressure measurement. Surface tension, γ is defined in equation 2.1 where G is the surface free energy and S is the surface area. The temperature, pressure and concentration are kept constant.

$$\gamma = \left(\frac{\partial G}{\partial S} \right)_{T,P,n_i} \quad \text{equation 2.1}$$

Surface pressure, Π is the difference between the surface tension of the subphase only (γ) and with monolayer present (γ_0)¹⁻³.

$$\Pi = \gamma - \gamma_0 \quad \text{equation 2.2}$$

There are two techniques used to measure surface pressure, the Langmuir balance and the Wilhelmy method¹. The Langmuir balance has a float which separates an area of the subphase with monolayer present from a region of just water and for this reason is considered a differential method. The surface pressure exerted by the film moves the float until balanced by an equal force applied by a spring. A displacement transducer is used to measure the spring deflection. A Wilhelmy plate was used experimentally with the Fromherz trough. The material used for the plate was a clean piece of filter paper. There

are three forces involved when considering the Wilhelmy plate, gravity and surface tension act downward while buoyancy moves the plate upward. A force balance is given¹ by equation 2.3. The length, width and thickness of the plate are given by l , w and t . The density of the plate material is ρ_p and the density of the subphase which is usually water is ρ_L . The gravitational constant is g and the contact angle, θ is the angle the liquid makes with the Wilhelmy plate. The height of the plate immersed in liquid is h .

$$F = \rho_p g l w t + 2\gamma(t+w)\cos\theta - \rho_L t w h \quad \text{equation 2.3}$$

The plate was initially wetted by the water only and the pressure is adjusted to read zero with a potentiometer. The surface tension measured was the difference between the pure water and monolayer on the water. In this case a simple equation can be used and it is assumed $t \ll w$. The presence of a monolayer reduces the surface tension of pure water.

$$\Delta\gamma = \Delta F / 2w \quad \text{equation 2.4}$$

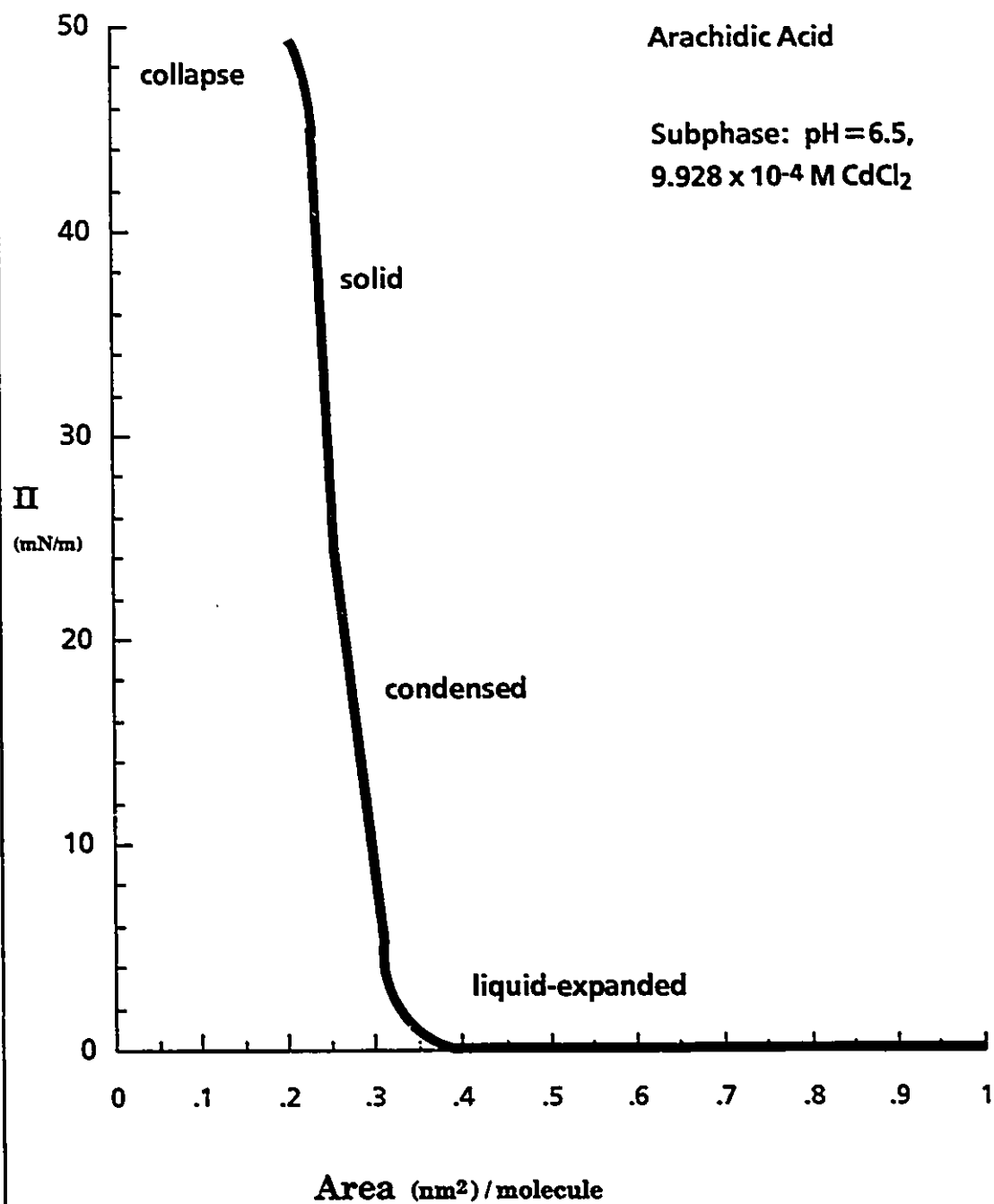
The calibration of the surface pressure measured by the Wilhelmy plate was carried out by adding a weight of known mass to the wire support for the plate. The area of the filter paper piece was such that the weight exerted a known force of 100 mN/m.

There are many types of materials that can be deposited as LB films^{1,2}. Fatty acids are one of the most common classes used for LB work. Fatty acids contain a polar head group and a long alkyl chain. On the water surface, fatty acids will orient so that the hydrophilic polar group is in the water with the hydrophobic tail pointing away from the water. LB films however, are not restricted to these classical types of films. The LB material is dissolved in a solvent which is immiscible with the water subphase. The materials which are discussed in later chapters, phthalocyanines and perylenes, are considered pigments in most instances because of their lack of solubility. However, solvents can be selected to provide a small amount of solubility at low concentrations on the order of 10^{-4} M. High purity solvents must be used for LB work so that contamination is not introduced. A known volume of LB material in solvent is introduced to the surface of the LB trough using a calibrated syringe. The solvent readily evaporates leaving the LB molecules on the surface of the trough.

As the moving barrier is compressed, surface pressure readings are collected from the Wilhelmy plate or Langmuir balance. A surface pressure versus area isotherm is collected in this manner. There are four regions in the isotherm for a classical LB material⁴. At very high areas, the molecules are spread apart and are in a gaseous state. As compression continues, the tails lift away from the water in the liquid-expanded region, followed by a region of constant slope in which the molecules are in a liquid-condensed state and finally a steeply sloping regime where the film is packed tightly and displays solid behavior. At high surface pressures collapse of the monolayer can occur. A typical surface pressure-area isotherm is shown in Figure 2-2.

Figure 2-2: Surface pressure-area isotherm for arachidic acid. Subphase pH=6.5 and 9.928×10^{-4} M CdCl_2 . Gaseous phase at large area per molecule not shown. Four distinct phases apparent: liquid-expanded, condensed, solid and collapse.

Figure 2-2

SURFACE PRESSURE - AREA ISOTHERM

Equation 2.5 was used to determine the area/molecule in Figure 2-2.

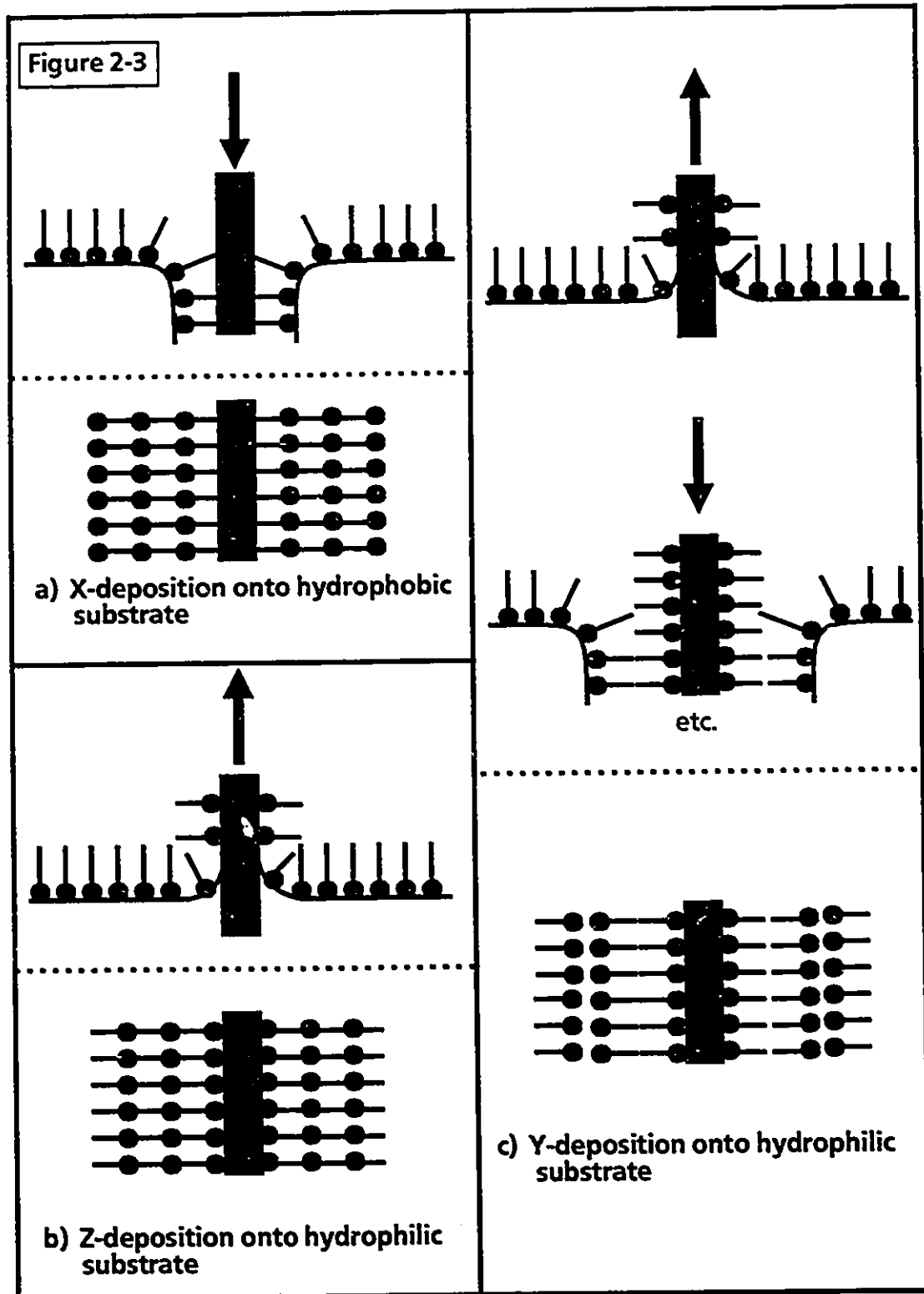
$\frac{\text{Area}}{\text{molecule}} = \frac{\text{Surface area}}{\text{Avogadro's no.} \times \text{concentration} \times \text{volume}}$	equation 2.5
--	-----------------

A line can be extrapolated from the steeply sloping region of the solid part of the isotherm and a value of area/molecule read from the x-axis. The first part of an LB experiment is to collect the surface pressure-area isotherm. Next, deposition onto the substrate must be considered.

Many different substrates can be used for Langmuir-Blodgett films. Glass and quartz are hydrophilic. Atomically flat substrates such as polished silicon wafers and mica can be used as substrates for LB work and later atomic forces microscopy. Glass can be made hydrophobic by using silanizing agents⁷⁻⁹. Langmuir-Blodgett deposition of monolayers onto metal island films is demonstrated in a later chapter for surface-enhanced Raman spectroscopy. Whatever substrate is chosen, it is important that it be clean.

There are a number of deposition techniques which can be used to build up Langmuir-Blodgett films¹⁻³ and a few of these are illustrated in Figure 2-3. X-type deposition is carried out by dipping a hydrophobic substrate into the water subphase. The hydrophobic tail is adjacent to the substrate surface. The subsequent film layers have hydrophilic to hydrophobic contact which may not be particularly stable. Z-type deposition involves withdrawing a hydrophilic substrate through the monolayer. The hydrophilic head group is adjacent to

- Figure 2-3:
- a) X-type LB deposition onto a hydrophobic substrate.
 - b) Z-type LB deposition onto a hydrophilic substrate.
 - c) Y-type LB deposition onto a hydrophilic substrate by withdrawal and dipping.



the hydrophilic substrate. Once again, layers of the film have hydrophilic-hydrophobic contact. Y-type deposition involves successive withdrawal and dipping of the substrate. Adjacent layers have hydrophilic-hydrophilic contact and hydrophobic-hydrophobic contact.

A substrate dipper is used for LB deposition with variable speeds and a smooth action. The transfer of a monolayer to a substrate is carried out in a constant pressure mode. A feedback to the control of the moving barrier is necessary so a compensation takes place as material is removed during transfer to the substrate. One measure of the quality of LB deposition is the transfer ratio, t_R given in equation 2.6.

$t_R = \frac{\text{area removed from trough}}{\text{area transferred to substrate}}$	equation 2.6
--	--------------

A consistent transfer ratio is important. A transfer ratio of one suggests good transfer and that the orientation of the monolayer on the substrate is similar to that on the subphase.

2.2 VACUUM EVAPORATED FILMS

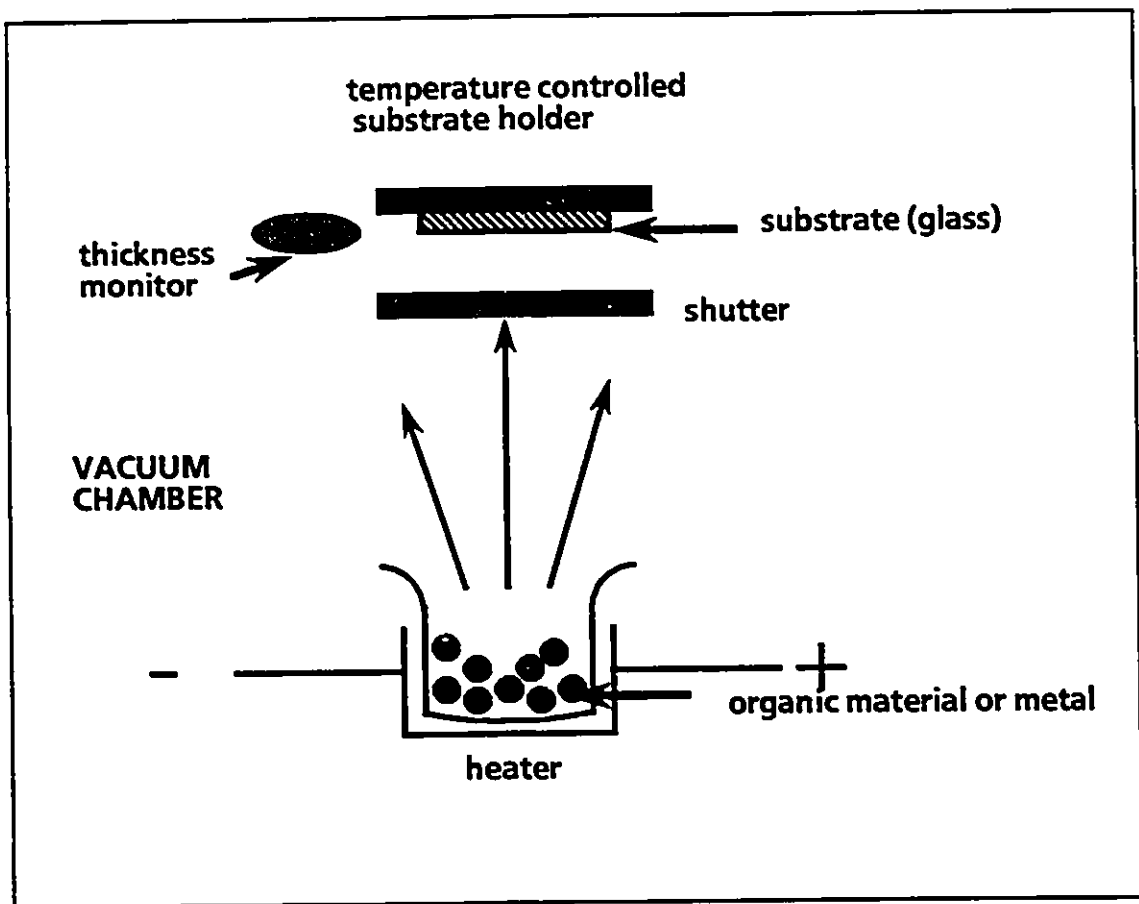
A description of high vacuum systems is available in the literature^{10,11}. A Vacuum Generators DPUHV12 model was actually used in the experimental section. Two types of materials were vacuum evaporated, metals and organic pigments. The metals were of high purity and the boat was selected so that an alloy was not formed on heating. The organic pigments were previously purified by vacuum sublimation and were placed in a quartz boat. Pigments were selected which did not decompose before the temperature for evaporation was reached. Current was passed through either the metal boat or metal surrounding the quartz holder. The high vacuum was achieved by the presence of a roughing pump and a diffusion pump. The substrate was Corning 7059 glass and was clipped to a substrate holder which allowed heating or cooling. There are further details in the experimental section.

The vacuum chamber was evacuated to a predetermined pressure. At this point the shutter was closed and current gradually applied to the boat. A quartz crystal thickness monitor was located close to the substrate position. As material started to evaporate, readings were observed on the thickness monitor. Once the evaporation rate had stabilized to the desired rate, the shutter was opened. The current was shut off and shutter closed once the desired thickness was obtained. Figure 2-4 is a schematic representation of the vacuum evaporation system.

Figure 2-4: Schematic of a typical vacuum evaporation experiment. An organic material or metal is heated in a vacuum chamber and deposited on substrate. The mass thickness is followed with a quartz crystal thickness monitor.

Figure 2-4

VACUUM EVAPORATION



2.3 RAMAN SPECTROSCOPY THEORY

2.3.1. Normal Raman

Raman spectroscopy and infrared spectroscopy provide vibrational information which is complementary in nature. The observed frequencies depend on selection rules unique to each technique. The molecular symmetry and crystal form determines which vibrations are active. The relative intensities of bands may be quite different in the Raman spectrum versus the IR spectrum because the mechanisms are very different. For a mode to be Raman active, there must be a change in the molecular polarizability during that vibration. A change in the molecular dipole moment during vibration is a requisite for IR activity.

There are instrumental differences between an FTIR spectrometer and a Raman spectrometer. The source in an IR instrument is very broad in nature spanning a range of 200–4000 cm^{-1} . In comparison, lasers are intense monochromatic sources for Raman work with lines available in the UV, visible and near-IR regions. Molecules undergo absorption of IR radiation during the measurement of an infrared spectrum. The molecules are excited from the ground vibrational state to a higher vibrational state. Modern infrared spectrometers have interferometers which allow all frequencies to be detected simultaneously. The Michelson interferometer has a fixed and a moving mirror. During one scan, the moving mirror travels a distance defined by the desired resolution. The light from two beam paths interact either constructively or destructively. The measured IR intensity is a function of the distance (or velocity \times time). A mathematical transformation is carried out to convert from the time domain to a frequency domain, thus the term Fourier transform infrared (FTIR). An infrared spectrum is a plot of intensity

(absorbance or transmittance) versus frequency in wavenumbers (units cm^{-1}). An FTIR sample is ratioed against a background to take instrumental factors into account. Two examples of FTIR detectors are the MCT and DTGS detectors.

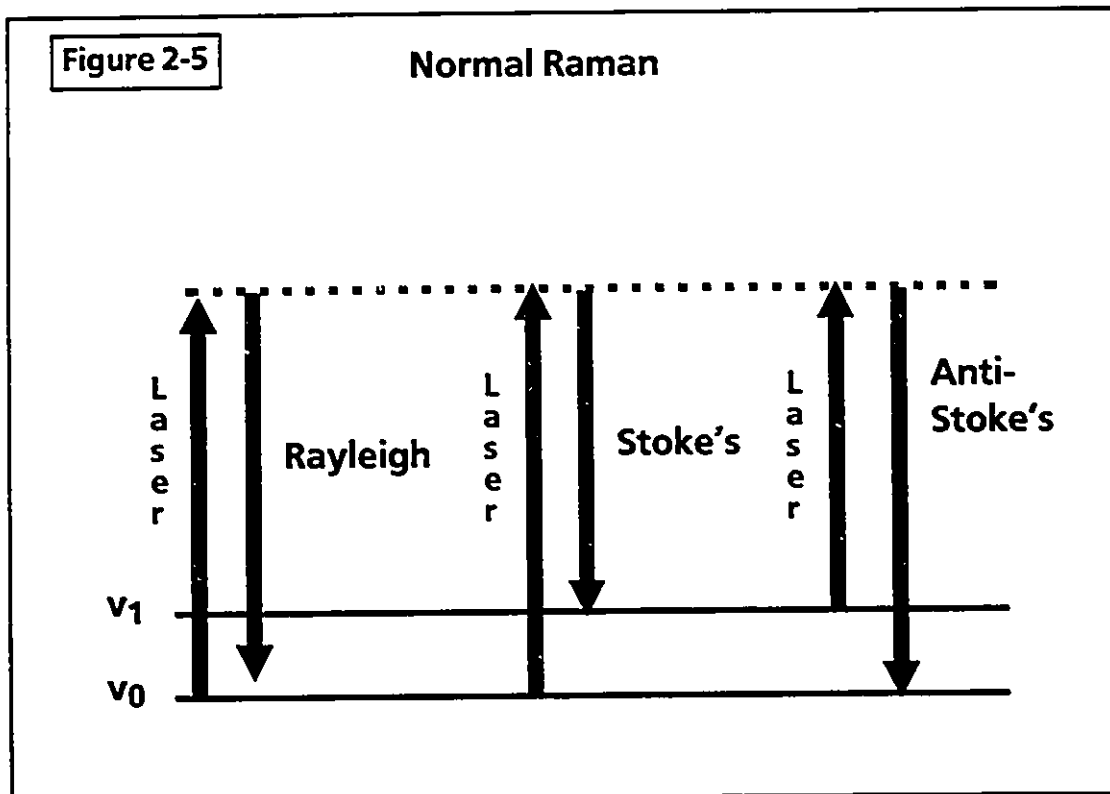
In a Raman experiment, an intense monochromatic source such as a laser strikes a sample and most of the light is scattered elastically producing Rayleigh scattering. However, a very small proportion of photons will be scattered inelastically giving Raman scattering. There are two possibilities for Raman scattering, Stoke's and anti-Stoke's, both causing a shift in the frequency of the light. Figure 2-5 shows the vibrational energy levels. For Stoke's scattering, the frequency of scattered light is less than the frequency of the incident light. Molecules are excited from a ground vibrational state ($v=0$) to a higher energy state. The molecules leave this higher energy state and return to an excited vibrational state (eg. $v=1$). In the anti-Stoke's situation, molecules start in an excited vibrational state (eg. $v=1$), are excited to a higher energy state and then return to the ground vibrational state ($v=0$). The frequency of anti-Stoke's scattering is greater than the frequency of the incident light. Stoke's scattering is usually much more intense than anti-Stoke's because few molecules start out in an excited vibrational energy level.

The laser source used for Raman spectroscopy has an electric field E and frequency ν_0 given by equation 2.7.

$$E = E_0 \cos(2\pi\nu_0 t)$$

equation 2.7

Figure 2-5: Schematic showing vibrational energy levels and photons for elastic Rayleigh scattering, inelastic Stoke's and anti-Stoke's normal Raman scattering.



A dipole moment, μ is induced in the molecule by the electric field of the laser. The molecular polarizability α describes the ease of electron deformation in a molecule.

$$\mu = \alpha E$$

equation 2.8

The molecular polarizability is a tensor which has nine components, another form of equation 2.8 follows:

$$\begin{pmatrix} \mu_x \\ \mu_y \\ \mu_z \end{pmatrix} = \begin{pmatrix} \alpha_{xx} & \alpha_{xy} & \alpha_{xz} \\ \alpha_{yx} & \alpha_{yy} & \alpha_{yz} \\ \alpha_{zx} & \alpha_{zy} & \alpha_{zz} \end{pmatrix} \begin{pmatrix} E_x \\ E_y \\ E_z \end{pmatrix}$$

equation 2.9

For normal Raman scattering, there are six polarizability components modulated by a molecular vibration because the polarizability tensor is symmetric: $\alpha_{xy} = \alpha_{yx}$, $\alpha_{xz} = \alpha_{zx}$ and $\alpha_{yz} = \alpha_{zy}$.

The molecular polarizability in equation 2.10 consists of the polarizability, at the equilibrium nuclear coordinates (α_0) and polarizability which is modulated by the vibrational frequency ν_1 ¹².

$$\alpha = \alpha_0 + \alpha_0 \cos(2\pi\nu_1 t)$$

equation 2.10

The change in polarizability with respect to the normal coordinates, Q can be expressed in the form of equation 2.11¹².

$$\alpha = \alpha_0 + \sum (\partial\alpha/\partial Q_i) Q_i + \dots \quad \text{equation 2.11}$$

It is the second term in equation 2.11, also called the polarizability derivative α' which produces Raman scattering. There must be a change in the molecular polarizability in order for a vibration to be Raman active. From this point on the symbol α will represent the molecular polarizability derivative.

Equation 2.12 is the expression for the intensity of radiation emitted by an oscillating dipole¹². The intensity is affected by the frequency to the fourth power. The electric field of the laser and the molecular polarizability are included through $\mu = \alpha E$.

$$I = \left(\frac{16\pi^4 \nu^4}{3c^3} \right) \mu^2 \quad \text{equation 2.12}$$

In the case of conventional normal Raman spectroscopy, the scattered light is separated into different wavelengths with gratings. Holographic gratings can be used in double or triple monochromators. One type of detector for Raman scattering is the photomultiplier tube. Spectral sensitivity is an important consideration when selecting a detector for scattered light which can be in the UV, visible or near-IR region. In the conventional Raman

system, the gratings are moved so that different wavelengths are passed over the photomultiplier tube. It can be time consuming to collect an entire spectrum. Alternatively, all frequencies could strike a detector array such as a charge-coupled device (CCD) or photodiode array simultaneously. The time to collect a spectrum in this case is short. There are now FT-Raman spectrometers which have a laser source, interferometer and an appropriate detector. Lasers with near-IR lines are used with infrared detectors. A review of dispersive Raman and FT-Raman systems has been recently published¹³. Whatever system is used, there must be a way of removing the intense Rayleigh scattering from the weak Raman scattering.

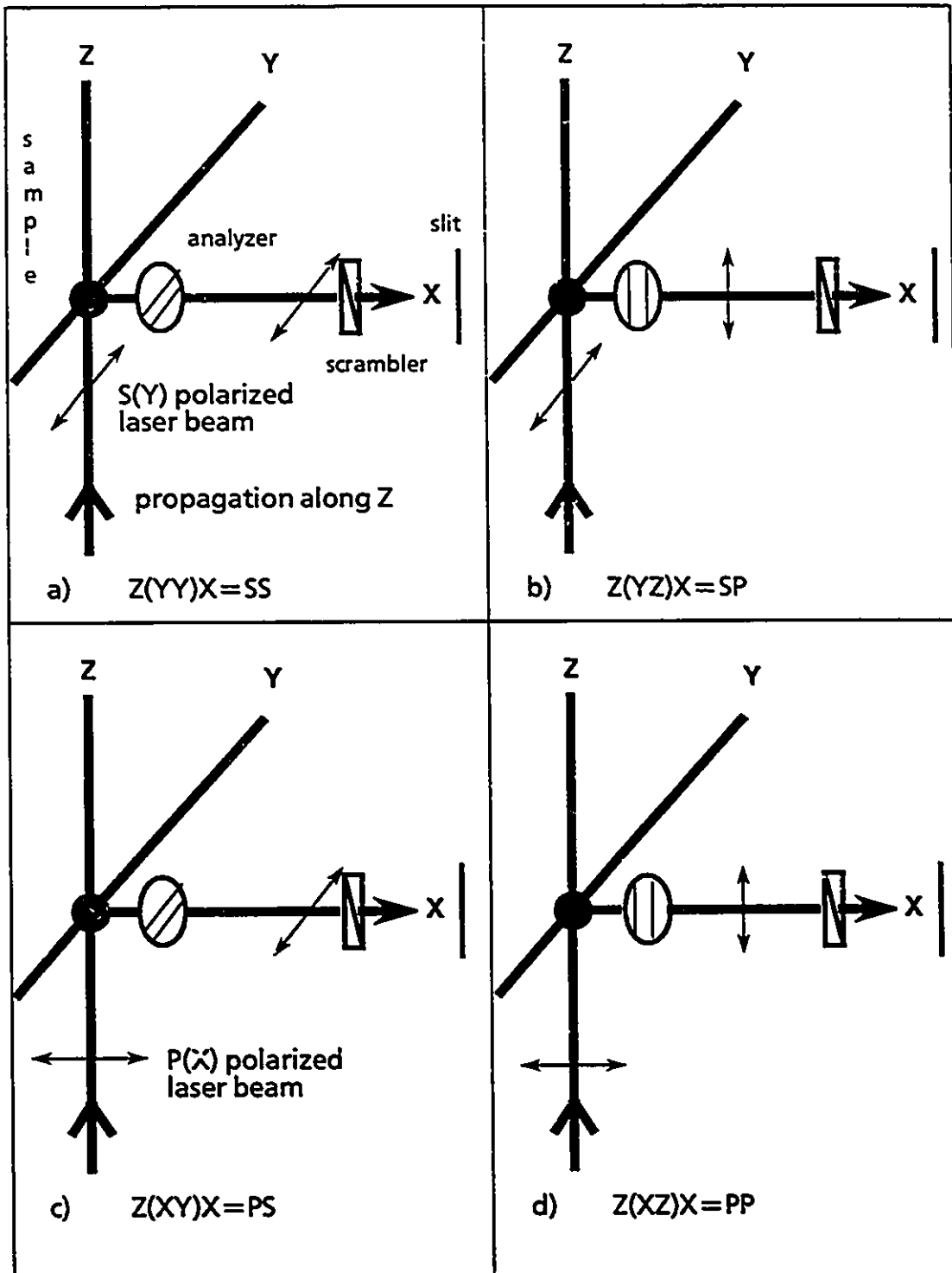
2.3.2 Polarizations of Light

A brief discussion can be made here concerning the notation for different polarizations of laser light that are available for a Raman experiment. The notation being used is that of Porto¹⁴. Figure 2-6 shows the four polarizations SS, SP, PS and PP that can be determined in a Raman experiment with a 90 degree geometry between the direction of propagation of the laser and the collection of scattered light. There are two possible polarizations of the laser, perpendicular to the scattering plane, S and parallel, P. The analyzer after the sample also has two positions S and P.

Depolarization ratios¹⁵ are commonly measured for liquids and have values ranging from 0 to 3/4. In liquid samples, important information is gained about the molecular symmetry of a vibration from the depolarization ratio. A totally symmetric vibration produces a Raman band with a depolarization ratio between 0 and 3/4 while antisymmetric vibrations are depolarized.

Figure 2-6: The four polarizations of light according to Porto¹⁴ for a ninety degree Raman scattering experiment. The propagation of the laser is along the z-axis. Collection of scattered light is along the x-axis. The four polarizations are SS, SP, PS and PP. The terms inside the brackets describe the electric field vector of the laser and the electric field vector of the light analyzed after the sample.

Figure 2-6



The experimental work presented in later chapters is for Langmuir-Blodgett films and vacuum evaporated films which exist in the solid state. Polarization ratios SS, SP, PS and PP can provide information about molecular orientation with respect to the substrate if a number of transformations are performed. There are three sets of coordinate systems that must be considered. Firstly, there is the molecular coordinate system. A transformation is carried out to go from molecular coordinates to the second system, the substrate coordinates. The orientation of the molecule with respect to the substrate is important. Thirdly, the laboratory coordinates are defined by the position of the substrate in relation to the incident laser beam and collection of scattered light.

2.3.3 Resonance Raman

Resonance Raman (RR) scattering occurs when the laser excitation wavelength coincides with a molecular electronic transition. Resonance Raman scattering is more intense than normal Raman scattering due to a change in the molecular polarizability derivative tensor. $(\alpha_{p\sigma})_{GF}$ is the poth component of the Raman scattering tensor and $p\sigma$, = x, y or z. The ground state is represented by G and the final state is F. The elements of the polarizability tensor are given by¹⁶⁻¹⁸:

$$(\alpha_{p\sigma})_{GF} = \frac{1}{\hbar} \sum_I \left(\frac{\langle F|r_p|I \rangle \langle I|r_\sigma|G \rangle}{\nu_{GI} - \nu_L - i\Gamma_I} + \frac{\langle I|r_p|G \rangle \langle F|r_\sigma|I \rangle}{\nu_{IF} - \nu_L - i\Gamma_I} \right)$$

equation 2.13

I = vibronic excited states

r = electron position operator

Γ_I = damping term

From equation 2.13, it can be seen that the first term in the summation becomes very large if ν_L approaches ν_{GI} for an allowed electronic transition and that the damping term related to the bandwidth of the electronic transition prevents the expression from reaching infinity. The polarizability tensor for resonance Raman may become asymmetric, i.e. $\alpha_{xy} \neq \alpha_{yx}$, etc. A new term is introduced into intensity and depolarization expressions.

$(C_{pq})_{GF}$ has been divided into two terms described by Albrecht¹⁶⁻¹⁷. The first term is Albrecht's A term and involves Franck-Condon factors. Only totally symmetric terms are enhanced in the RR spectrum. Albrecht's B term for RR follows a Herzberg-Teller mechanism where electronic states are mixed and non-totally symmetric modes can be observed.

Resonance Raman scattering can be distinguished from normal Raman scattering in a number of ways. The intensity of normal Raman scattering will follow a ν^4 dependence on excitation frequency whereas RR scattering varies greatly with excitation frequency. The RR time dependence is slower than off-resonance or normal Raman scattering. The relative intensity of Stoke's to anti-Stoke's scattering for normal Raman is determined by the Boltzman distribution. However, this is not true for RR and the intensity of anti-Stoke's scattering can actually exceed Stoke's scattering.

Surface-Enhanced Raman Scattering is covered in Chapter 3.

2.3.4 FT-Raman Spectroscopy

A series of reviews and applications have appeared concerning FT-Raman spectroscopy¹⁹⁻⁶⁰. There were a number of reasons why FT-Raman systems were developed. Intrinsic fluorescence or fluorescence due to impurities in samples has been a severe problem for Raman spectroscopy using visible laser excitation. Fluorescence is a much more efficient process than Raman scattering and can completely mask Raman signals. The 1064 nm line or in a special case⁶⁰ the 1339 nm line of a Nd/YAG laser can eliminate or greatly reduce fluorescence. Some materials have an electronic absorption in the visible region and will photodecompose when exposed to visible light. Biomolecules that fall into this category that have been examined by FT-Raman spectroscopy include: cobalamins, bacteriorhodopsin, chlorophylls, cytochrome c and porphyrins⁵⁸. It may be desirable to obtain normal Raman scattering rather than resonance Raman scattering.

A multiplexing system based on a Michelson interferometer has an internal frequency calibration using a He-Ne laser. The precision and accuracy of frequencies is extremely high. This makes it possible to carry out spectral subtractions in an FT-Raman system. An example of where this is important is for biological assemblies where membrane reorganizations are reflected in small frequency shifts²⁵. Dispersive instruments which have holographic gratings have greater errors in the frequencies and are less predictable¹⁹.

Interferometers have a throughput (Jacquinot's) advantage compared to dispersive spectrometers²⁰. If the Raman experiment is detector noise limited rather than shot noise limited, a multiplexing (Felgett's) advantage is achieved using the interferometer. It should be mentioned that there is a disadvantage

in using near-IR excitation rather than visible excitation for Raman spectroscopy. The intensity of Raman scattering is proportional to ν^4 and drops by a factor of sixteen going from 514.5 nm to 1064 nm²⁰. The throughput and multiplexing advantages can compensate for the lower Raman scattering cross-section in the near-IR region.

Another advantage of FT-Raman instrumentation is it is relatively cheap compared to a conventional dispersive Raman system operating in the visible with a photomultiplier tube (PMT) and can be operated with minimal training. There are systems which consist of combined FT-Raman and FTIR modules. The information from Raman and IR experiments are complementary since the selection rules are different and both techniques should be applied to a problem. FT-Raman is non-destructive and sample preparation is very simple. Cuvettes, mp capillary tubes, and nmr tubes can be used to hold the sample. The optimal sample cells have been reported and include a spherical cell with a reflecting layer^{28,38,51}. Water is highly absorbing and interferes with FTIR spectra. The overtone region of water has some absorption in the near-IR region used for FT-Raman spectroscopy and can reduce the scattering intensity of C-H stretching modes²⁵.

Fiber optic probes that were developed for the telecommunications industry have their best performance in the region 1.3 μm to 1.7 μm which is ideal for FT-Raman spectroscopy³⁷. There are two ways to carry out remote Raman process monitoring²². A small instrument could be used in situ and the spectra shipped to a central location for analysis or a fiber optic bundle could carry the laser beam to the process site and take the scattered light away. The fibers should be of a type which has the lowest water content possible²¹.

Results have been reported for indene and a polymerization reaction of styrene with initiator at 70°C followed in situ³⁷. A suggested application of FT-Raman with fiber optics is monitoring cure reactions and rates during vulcanization at different depths within a compound or to follow in-service aging of a tire³⁵. Two arrangements of optical fibers have been described for FT-Raman measurements of SERS active colloids and electrodes⁵³. A near-IR system with fiber optics is being developed to monitor contaminants of groundwater in situ that are in wells 100 to 600 feet below the surface of the earth⁴².

The 1064 nm line of a neodymium-doped yttrium-aluminum garnet (Nd/YAG) solid state laser is the most common excitation source for FT-Raman spectroscopy. Future developments could be based on a neodymium-doped yttrium lithium fluoride (Nd/YLF) diode pumped laser of wavelength 1047 nm which is small and does not require cooling²¹. The present drawbacks are higher power is needed and lower cost. There could be a move to slightly shorter wavelengths in the range 790-900 nm using a narrow line-width laser with photodiode detection²². A compromise would be made which would cause sample fluorescence to increase but background from thermal emission of hot samples would be moved and less noisy detectors are available²². A near-IR Raman system has been described incorporating a tunable Ti-sapphire laser which can operate at wavelengths between 790-850 nm with charge-coupled device (CCD) detection⁵².

FT-Raman instruments are available with various scattering geometries such as 180 degree backscattering. It is extremely important that the relatively intense Rayleigh line be eliminated from the scattered radiation entering the

interferometer and ultimately striking the detector. The first problem is the detector would require an extremely large dynamic range to accommodate Raman and Rayleigh scattering. It is conceivable the Rayleigh component would saturate the detector. Secondly, the interferogram would have a large modulated Rayleigh line on top of a weak Raman spectrum and shot noise would be distributed over the spectrum^{20,22}. Many approaches including filtering have been described in the literature to remove the intense Rayleigh line²¹⁻²³. Advances in Rayleigh rejection are needed to access longitudinal acoustic modes (LAMs) close to the Rayleigh line. The scattered light enters a Michelson interferometer which contains appropriate beamsplitters as well as moving and stationary mirrors.

The detectors suitable for near-IR radiation include InGaAs, Ge and PtSi^{19,21,48,59}. Detector response curves are published for Ge and InGaAs²¹. Both of these materials exhibit lower noise equivalent powers (NEPs) at cryogenic temperatures, however spectral response is reduced. Thus, the Ge detector operated at 77K falls off at frequency shifts greater than 2500 cm^{-1} with a 1064 nm laser line¹⁹. This would sacrifice the C-H and N-H stretching region of the FT-Raman spectrum. The InAs detector is better in terms of responsivity than other materials but the noise is unacceptable²¹. Silicon detectors have a low response above 1 micron and would be useful for anti-Stokes FT-Raman only⁵⁹. Platinum silicide extends into the near-IR but one problem is thermal background and low sensitivity. At present the best choice for the desired near-IR spectral response and lowest noise is an InGaAs detector operating somewhere between 77K and room temperature⁴⁸.

There have been reports of FT-SERS of pyridine on metal electrodes such as copper, silver and gold using 1064 nm laser excitation^{39-40,42-43}. Electrodes are roughened either ex situ with just the electrolyte present or in situ with the species to be studied also present. This is accomplished by oxidation-reduction cycles (ORCs). The metal electrode is the working electrode, a platinum counter electrode is present and a reference electrode such as the saturated calomel electrode (SCE) is part of the cell. The FT-SERS spectrum depends on the electrode material and the potential applied to the working electrode^{39,43}. Often broad backgrounds are observed due to the metal. The calculated enhancement factors for pyridine are in the range 10^5 - 10^6 on copper and gold electrodes⁴². In order for FT-SERS to be useful for chemical sensor applications, the species of interest must be able to be desorbed from the electrode at some potential to allow electrode reconditioning. It has been shown that reconditioning of a copper electrode can take place after pyridine has been adsorbed, but a gold electrode was irreversibly affected by pyridine adsorption⁴². There is a complex dependence between potential and pH for pyridine adsorbed on a silver electrode⁴³. The positions and relative intensities of bands attributed to ring breathing and deformations indicate there were at least two or three types of pyridine species with at least two orientations. The reproducible splitting of bands was indicative of the existence of multiple environments.

FT-SERS of 3-picoline and 3-chloropyridine has been observed on copper electrodes⁴¹. The calculated enhancement factors were 9×10^5 and 5×10^5 respectively. This work was part of an initial study of environmental contaminants using FT-SERS. The adsorption of ferro- and ferricyanide ions onto a gold electrode in lithium chloride and cesium chloride has been

discussed⁴³. The redox species were adsorbed in ion pairs and were present in a variety of environments which could be due to different metal sites. The corrosion inhibitors benzotriazole (BTA) and tolyltriazole (TTA) give SERS in the near-IR on copper electrodes⁵⁵. These inhibitors are circulated in cooling water to reduce corrosion of copper containing parts. The FT-SERS results indicate that both BTA and TTA are adsorbed through the azole ring and it is this film which protects the copper. Commercial antifreezes which contain water, ethylene glycol and organic inhibitors selectively adsorbed the organic inhibitors on the copper electrode⁵⁵.

2.4 ATOMIC FORCE MICROSCOPY

There are many references available concerning atomic force microscopy (AFM) and scanning tunneling microscopy (STM)⁶¹⁻¹⁶¹. This section will give a brief description of AFM. Papers are cited in Chapter 6 for AFM work on phthalocyanines, perylenes, fatty acids and self-assembled monolayers and particular attention is paid to AFM of Langmuir-Blodgett monolayers.

Atomic force microscopy (AFM) has a number of advantages for imaging Langmuir-Blodgett (LB) films and thin solid films compared to other techniques such as electron microscopy and scanning tunneling microscopy (STM). The contact mode of the AFM gives higher resolution in height (z-direction) than electron microscopy. The resolution of the AFM in the x-y plane is also excellent and is affected by the tip geometry and tip composition as well as sample properties. The AFM can image regions on the order of microns to nanometers. LB films for AFM are transferred to atomically flat substrates which include mica, highly oriented pyrolytic graphite (HOPG) and silicon wafers. The AFM can be operated in an aqueous environment in which a non-

conducting sample and tip are submerged and this is of interest for biological studies⁷⁰.

For scanning electron microscopy (SEM), the sample must be conductive, a thin conductive layer applied or replicas prepared. In some instances the sample is not directly imaged. To carry out transmission electron microscopy (TEM), the sample is transferred to a substrate such as a carbon-coated microscope grid. There is insufficient contrast to image a single LB monolayer unless some sort of surface decoration technique is used to increase contrast. Materials can be damaged when subjected to high energy electrons.

Both AFM and STM give local information. Many characterization techniques such as IR, Raman, X-ray or neutron scattering give spatially averaged results over a large number of atoms. AFM and STM are good choices for observing local defects such as pinholes, cracks, grain boundaries or heterogeneous structures such as mixed LB films. In the best case for STM, atomic resolution can be achieved and features observed which are 0.2 nm in diameter¹²⁰. Although STM requires that the sample under investigation be conductive, the AFM can image conductive and non-conductive materials. In STM, electrons tunnel between the tip and the sample. The images reveal aspects of the sample topography and electronic structure. What is observed is the density of electronic states at the Fermi level. Results from AFM can be considered complementary to STM because AFM images are due to energy levels up to the Fermi level.

The contact mode of the AFM senses repulsive forces which are due to an overlap of the electrons in the tip with electrons of the nearby atoms on the

sample surface. One must be careful not to disrupt van der Waals forces between molecules or hydrogen-bonding when imaging LB films. There should be some sort of immobilization of the LB film on the substrate either through covalent bonding or physisorption. Molecular stacking causes strong intermolecular interactions which can help stabilize the position of the LB film. Experimentally, a cantilever with a low spring constant can be used or samples imaged under water. The force applied to an organic surface in a STM experiment is approximately 10^{-7} newtons, orders of magnitude greater than most AFM experiments¹⁶². AFM is the preferred technique for imaging thin organic films because sample damage can be minimized.

An atomic force microscope consists of a tip and cantilever to sense the force. The cantilever deflection is detected either electronically or optically. Some sort of mechanical scanning system is required and usually has a piezoelectric component. The tip is held stationary while the sample is moved in the x and y directions. The data which is acquired is a map of forces over points on the surface of the sample. A feedback system is incorporated to control the vertical distance (z) between the tip and sample allowing two modes of operation, constant force and constant height. It is important to minimize any mechanical vibrations of the AFM. A display system is used to convert the data into an image and data processing is performed.

Initial AFM experiments were carried out using metal foil as the cantilever¹⁶¹. Melmed¹²⁸ has reviewed the literature on making sharp tips for field ion microscopy, field electron emission microscopy and STM with an emphasis on electrolytic methods. In addition AFM force sensors have been constructed from carbon and quartz fibers¹²⁶. The tips are formed by chance

on broken ends. AFM and STM can be performed simultaneously if graphite fibers are used for the probe. Tips for cantilevers have been prepared by attaching diamond fragments by hand to the end of levers^{144,147}. Microfabrication techniques are presently used to provide silicon, silicon dioxide and silicon nitride cantilevers with and without integrated tips^{134,138}.

It is desirable to have a cantilever with a low spring constant in the range 0.1 to 10 N/m with a high resonance frequency¹⁰⁷. Rugar and Hansma¹¹⁸ calculate a value of 10 N/m for an interatomic spring constant (k) based on vibrational frequencies (ω) on the order of 10^{13} Hz or higher and mass of atoms (m) on the order of 10^{-25} kg using the expression:

$$k = \omega^2 m$$

equation 2.14

The cantilever spring constant and force must be kept much lower than 10 N/m so that van der Waals interactions, hydrogen-bonding and bonds are not disrupted or broken.

There are numerous ways to detect cantilever deflection. Early AFM experiments described by Binnig and Quate¹⁶¹ used electron tunneling to measure the deflection of the cantilever. Meyer and Amer⁶⁸ described an optical method to detect cantilever deflection in an AFM by bouncing a laser beam off the back of the cantilever. Deflections were measured with a position sensitive photodiode and the smallest deflection that could be measured was only limited by thermal vibrations. Sarid and Elings¹⁰⁵ have

reviewed scanning force microscopy and discuss the seven methods to detect cantilever deflection. Additional methods include an electronic method which senses small changes in the capacitance and determines motions of a cylindrical cantilever^{141,142}. Other optical methods are homodyne¹⁴³, heterodyne¹⁴⁴, laser diode feedback¹⁴⁵ and polarization¹⁴⁶. Optical methods are preferred over tunneling because the laser spot averages over a larger area on the cantilever backside and is less sensitive to roughness or contamination¹⁰⁷. The detection method should not exert a measurable force on the cantilever.

A mechanical scanning system is an integral part of the AFM which allows data to be collected over the sample surface. Usually the sample is scanned in the x and y directions while the tip is held stationary. A coarse mechanical system brings the tip and the sample into the operating range of a finer system which has piezoelectric components. Piezoelectric materials change dimensions in a known fashion in response to applied voltages.

The imaging resolution of an AFM operating in contact with a LB film has been described in terms of the applied force, tip radius, adhesive force, sample and tip properties⁶⁶. Contact diameters were calculated using the Young's modulus of the LB film from nanoindentation experiments, the applied force and tip radius. At small forces the behavior was elastic but as the force was increased, a transition to inelastic deformation appeared. At this onset point there is irreversible damage to the LB film and line scans are no longer reproducible. Adhesive forces between the tip and the LB film have the effect of increasing the contact diameter and decreasing the resolution. There were suggestions made to improve imaging resolution⁶⁶. If the tip is sharpened, the adhesive force is decreased but there is the risk of sample damage by inelastic

deformation. Secondly, a stiffer tip with higher Young's modulus would be beneficial. Adhesion can be minimized by immersing the tip and sample in water. Another alternative would be to image in a non-contact mode.

2.5 SUMMARY

An introduction to Langmuir-Blodgett films was contained in this chapter. A history of the development of LB films was given. The steps to collect a surface pressure-area isotherm and to deposit a LB film on a substrate were described. One way to prepare metal films and thin organic films is by vacuum evaporation which was considered briefly. The next section contained theory and background on Raman spectroscopy including normal Raman, resonance Raman and FT-Raman spectroscopy. Surface-enhanced Raman scattering is covered in Chapter 3. A comparison was made between infrared spectroscopy and Raman spectroscopy. The four polarizations of light SS, SP, PP, and PS have been defined for a 90 degree Raman experiment. A general review of atomic force microscopy was made with more specific references to phthalocyanines, perylenes, fatty acids and self-assembled monolayers reserved for Chapter 6. Atomic force microscopy was compared to scanning tunneling microscopy and electron microscopy. The components of atomic forces microscope have been described.

Chapter 2: References

1. *Langmuir-Blodgett Films*; Roberts, G., Ed.; Plenum Press, New York, 1990.
2. Ulman, A. in *Introduction to Ultrathin Organic Films From Langmuir-Blodgett to Self-Assembly*; Academic Press Inc., Toronto, 1991.
3. Gaines, G. L. in *Insoluble Monolayers at Liquid-Gas Interfaces*; Prigogine, I. Ed.; Interscience Publishers, New York, 1966.
4. Knobler, C. M. *Adv. Chem. Phys.* **1990**, *77*, 397.
5. *Thin Solid Films* **1994**, *242*, 1-1102.
6. Fromherz, P. *Rev. Sci. Instrum.* **1975**, *46*, 1380.
7. Von Tscharner, V.; McConnell, H. M. *Biophys. J.* **1981**, *36*, 241.
8. Honig, E. P.; Hengest, J. H. T.; den Engelson, D. J. *Colloid Interface Sci.* **1973**, *45*, 92.
9. Highfield, R. R.; Thomas, R. K.; Cummins, P. G.; Gregory, D. P.; Mingis, J.; Hayter, J. B.; Scharpf, O. *Thin Solid Films* **1983**, *99*, 165.
10. Hanlon, J. F. in *A User's Guide to Vacuum Technology*, 2nd ed.; John Wiley & Sons, Toronto, 1989.
11. Hablanian, M. H. in *High-Vacuum Technology*; Marcel Dekker, Inc., New York, 1990.
12. Champion, A. in *Vibrational Spectroscopy of Molecules on Surfaces*; Yates, T.; Madey, T. E. Eds.; Plenum Press, New York, 1987, pp. 348-350.
13. Chase, B. *Appl. Spectrosc.* **1994**, *48*(7), 14A.
14. Damen, T. C.; Porto, S. P. S.; Tell, B. *Phys. Rev.* **1966**, *142*, 570.
15. Lin-Vien, D.; Colthup, N. B.; Fateley, W. G.; Grasselli, J. G.; in *The Handbook of Infrared and Raman Characteristic Frequencies of Organic Molecules*; Academic Press Inc., San Diego, 1991, pp. 1-7.
16. Tang, J.; Albrecht, A. C. in *Raman Spectroscopy Theory and Practice*, Szymanski, H. A. Ed.; Plenum Press, New York, 1970.
17. Albrecht, A. C. *J. Chem. Phys.* **1961**, *34*, 1476.
18. Spiro, T. G. *Biochim. Biophys. Acta* **1975**, *57*(3), 169.
19. Crookell, A.; Hendra, P. J.; Mould, H. M.; Turner, A. J. *J. Raman Spectrosc.* **1990**, *21*, 85.
20. Cutler, D. J. *Spectrochim. Acta* **1990**, *2*, 123.

21. Cutler, D. J. *Spectrochim. Acta* 1990, 46A, 131.
22. Petty, C. J.; Bennett, R. *Spectrochim. Acta* 1990, 46A, 331.
23. Hirschfeld, T.; Chase, B. *Appl. Spectrosc.* 1986, 40(2), 133.
24. Purcell, F. J.; Heinz, R. E. *Canadian Chemical News* 1989, May, 17.
25. Levin, I. W.; Lewis, E.N. *Anal. Chem.* 1990, 62(21), 1101A.
26. Messerschmidt, R. G.; Chase, D. B. *Appl. Spectrosc.* 1989, 43(1), 11.
27. Jawhari, T.; Hendra, P. J.; Willis, H. A.; Judkins, M. *Spectrochim. Acta* 1990, 46A(2), 161.
28. Schrader, B.; Hoffmann, A.; Simon, A.
29. Levin, I. W.; Lewis, E. N. *SPIE Fourier Transform Spectroscopy* 1989, 1145, 99.
30. Wright, N. A., Krishnan, K. *SPIE Fourier Transform Spectroscopy* 1989, 1145, 186.
31. Shurvell, H. F.; Bergin, F. J. *SPIE Fourier Transform Spectroscopy* 1989, 1145, 192.
32. Chase, D. B. *SPIE Fourier Transform Spectroscopy* 1989, 1145, 172.
33. Deeley, C.; Sellors, J.; Spragg, R. *SPIE Fourier Transform Spectroscopy* 1989, 1145, 195.
34. Purcell, F. J. *Spectroscopy* year?, 4(2), 24.
35. Jackson, K. D. O.; Loadman, M. J. R.; Jones, C. H.; Ellis, G. *Spectrochim. Acta* 1990, 46A(2), 217.
36. Agbenyega, J. K.; Ellis, G.; Hendra, P. J.; Maddams, W. F.; Passingham, C.; Willis, H. A.; Chalmers, J. *Spectrochim. Acta* 1990, 46A(2), 197.
37. Williams, K. P. J.; Mason, S. M. *Spectrochim. Acta* 1990, 46A(2), 187.
38. Schrader, B.; Hoffman, A.; Tischler, M.; Podschadlowski, R.; Simon, A. *SPIE Fourier Transform Spectroscopy* 1989, 1145, 190.
39. Crookell, A.; Fleischmann, M.; Hanniet, M.; Hendra, P. J. *Chem. Phys. Lett.* 1988, 149(2), 123.
40. Chase, D. B.; Parkinson, B. A. *Appl. Spectrosc.* 1988, 42(7), 1186.
41. Angel, S. M.; Archibald, D. D. *Appl. Spectrosc.* 1989, 43(6), 1097.
42. Angel, S. M.; Katz, L. F.; Archibald, D. D.; Lin, L. T.; Honigs, D. E. *Appl. Spectrosc.* 1988, 42, 1327.

43. Fleischmann, M.; Sockalingum, D.; Musiani, M. M. *Spectrochim. Acta* **1990**, *46A*, 285.
44. Chase, B. *Proc. ACS Division of Polymeric Materials* **1991**, *64*, 189.
45. Claybourn, M.; Turner, P. *Proc. ACS Division of Polymeric Materials* **1991**, *64*, 193.
46. Claybourn, M.; Hendra, P.; Agbenyega, J. *Proc. ACS Division of Polymeric Materials* **1991**, *64*, 191.
47. Chase, B. *Anal. Chem.* **1987**, *59*(14), 881A.
48. Tripp, C.; Buijs, H. *Mikrochim. Acta* **1988**, *II*, 209.
49. Hendra, P. J. in *Proceedings of the Twelfth International Conference on Raman Spectroscopy*; Durig, J. R.; Sullivan, J. F. Eds.; John Wiley & Sons, Toronto, 1990, pp. 856-857.
50. Hendra, P. J.; Passingham, C.; Royaud, I. A. M. in *Proceedings of the Twelfth International Conference on Raman Spectroscopy*; Durig, J. R.; Sullivan, J. F. Eds.; John Wiley & Sons, Toronto, 1990, pp. 678-679.
51. Schrader, B.; Hoffman, A.; Simon, A.; Sawatzki *Vib. Spectrosc.* **1991**, *1*, 239.
52. Schulte, A. *Appl. Spectrosc.* **1992**, *46*(6), 891.
53. Angel, S. M.; Myrick, M. L. *Pract. Spectrosc.* **1992**, *13*, 225.
54. Petty, C. J. *Vib. Spectrosc.* **1991**, *2*, 263.
55. Sockalingum, D.; Fleischmann, M.; Musiani, M. M. *Spectrochim. Acta* **1991**, *47A*(9-10), 1475.
56. Lee, N. *Bull. Korean Chem. Soc.* **1991**, *12*(6), 601.
57. Guy, H.; Buijs, H. *SPIE Fourier Transform Spectroscopy* **1989**, *1145*, 197.
58. Yu, N.; Nie, S. *SPIE Laser Applications in Life Sciences* **1990**, *1403*, 112.
59. Chase, B. *SPIE Int. Conf. on Scientific Optical Imaging* **1990**, *1439*, 47.
60. Asselin, K. J.; Chase, B. *Appl. Spectrosc.* **1994**, *48*(6), 699.
61. Manivannan, A.; Nagahara, L. A.; Hashimoto, K.; Fujishima, A.; Yanagi, H.; Kouzeki, T.; Ashida, M. *Langmuir* **1993**, *9*, 771.
62. Pester, O.; Mrwa, A.; Heitschold, M. *Phys. Stat. Sol. (A)* **1992**, *131*, 19.
63. Ludwig, C.; Gompf, B.; Glatz, W.; Petersen, J.; Eisenmenger, W.; Mobius, M.; Zimmermann, U.; Karl, N. *Z. Phys. B. - Condensed Matter* **1992**, *86*, 397.

64. Bourdieu, L; Ronsin, O.; Chatenay, D. *Science* **1993**, *259*, 798.
65. Binning, G; Rohrer, H.; Gerber, Ch.; Weibel, E. *Rev. Phys. Lett.* **1982**, *49*(1), 57.
66. Weihs, T. P.; Nawaz, Z.; Jarvis, S. P.; Pethica, J. B. *J. Appl. Phys.* **1991**, *59*(27), 3536.
67. Mizes, H. A.; Loh, K. G.; Miller, R. J. D.; Ahuja, S. K.; Grabowski, E. F. *J. Appl. Phys.* **1991**, *59*(22), 2901.
68. Meyer, G.; Amer, N. M. *J. Appl. Phys.* **1988**, *53*(12), 164.
69. Burnham, N. A.; Dominguez, D. D.; Mowery, R. L.; Colton, R. J. *Phys. Rev. Lett.* **1990**, *64*(16), 1931.
70. Drake, B.; Prater, C. B.; Weisenhorn, A. L.; Gould, S. A. C.; Albrecht, T. R.; Quate, C. F.; Cannel, D.S.; Hansma, H. G.; Hansma, P. K. *Science* **1989**, *243*, 1586.
71. Annis, B. K.; Schwark, D. W.; Reffner, J. R.; Thomas, E. L.; Wunderlich, B. *Makromol. Chem.* **1992**, *193*, 2589.
72. Wang, P.; Shamsuzzoh, M.; Wu, X.; Lee, W.; Metzger, R. M. *J. Phys. Chem.* **1992**, *96*, 9025.
73. Snetivy, D.; Vancso, G. J. *Macromolecules* **1992**, *25*, 3320.
74. Kuroda, R.; Kishi, A; Yamano, A.; Hatanaka, H.; Matsuda, K.; Eguchi, K.; Nakagiri, T. *J. Vac. Sci. Technol. B* **1991**, *9*(2), 1180.
75. Sotobayashi, H; Schilling, T.; Tesche, B. *Langmuir* **1990**, *6*, 1246.
76. Hansma, H. G.; Gould, S. A. C.; Hansma, P. K.; Gaub, H. E.; Longo, M. L.; Zadinski, J. A. N. *Langmuir* **1991**, *7*, 1051.
77. Yeo, Y. H.; McGonigal, G. C.; Yackoboski, K.; Guo, C. X.; Thomson, D. J. *J. Phys. Chem.* **1992**, *96*, 6110.
78. Alves, C. A.; Smith, E. L.; Porter, M. D. *J. Am. Chem. Soc.* **1992**, *114*, 1222.
79. Sano, M.; Sasaki, D. Y.; Isayama, M.; Kunitake, T. *Langmuir* **1992**, *8*, 1893.
80. Schwark, D. W.; Vezie, D. L.; Reffner, J. R.; Thomas, E. L.; Annis, B. K. *J. Mat. Sci. Lett.* **1992**, *11*, 352.
81. Collin, B.; Chatenay, D.; Coulon, G.; Ausserre, D.; Gallot, Y. *Macromolecules* **1992**, *25*, 1621.
82. Luttrull, D. K.; Graham, J.; DeRose, J. A.; Gust, D.; Moore, T. A.; Lindsay, S. M. *Langmuir* **1992**, *8*, 765.
83. Hansma, H.; Motamedi, F.; Smith, P.; Hansma, P.; Wittman, J. C. *Polymer* **1992**, *33*(3), 647.

84. Wang, Y.; Juhue, D.; Winnik, M. A.; Leung, O. M.; Goh, M. C. *Langmuir* 1992, 8, 760.
85. Overney, R. M.; Howald, L.; Frommer, J.; Meyer, E.; Brodbeck, D.; Guntherodt, H. J. *Ultramicroscopy* 1992, 42-44, 983.
86. Fang, J. Y.; Lu, Z. H.; Wang, L.; Wei, Y. *Phys. Lett. A* 1992, 166, 373.
87. Weisenhorn, A. L.; Romer, D. U.; Lorenzi, G. P. *Langmuir* 1992, 8, 3145.
88. Bar, G.; Magonov, S. N.; Cantow, H. J.; Dietrich, M.; Heinze, J. *Synth. Met.* 1991, 41-43, 2335.
89. Overney, R. M.; Meyer, E.; Howald, L.; Frommer, J.; Brodbeck, D.; Luthi, R.; Haefke, H.; Guntherodt, H. J. *L'actualite chimique* 1992, Mars-Avril, 177.
90. Overney, R. M.; Meyer, E.; Frommer, J.; Guntherodt, H. J.; Decher, G.; Reibel, J.; Sohling, U. *Langmuir* 1993, 9, 341.
91. Krantzman, K. D.; Rees, D. C.; Farrelly, D. J. *Phys. Chem.* 1991, 95, 9039.
92. Hentschke, R.; Schurmann, B. L.; Rabe, J. P. *Chem. Phys.* 1992, 96(8), 6213.
93. Sumpter, B. G.; Getino, C.; Noid, D. W. *J. Chem. Phys.* 1992, 96(9), 7072.
94. Matsumoto, M.; Uyeda, N. *Thin Solid Films* 1993, 223, 358.
95. Nakamura, T.; Tachibana, H.; Yamura, M.; Matsumoto, M.; Azumi, R.; Tanaka, M.; Kawabata, Y. *Langmuir* 1992, 8, 4.
96. Fujiwara, I.; Ishimoto, C.; Seto, J. *J. Vac. Sci. Technol. B* 1991, 9(2), 1148.
97. Weisenhorn, A. L.; Egger, M.; Ohnesorge, F.; Gould, S.A.C.; Heyn, S. P.; Hansma, H. G.; Sinsheimer, R. L.; Gaub, H. E.; Hansma, P. K. *Langmuir* 1991, 7, 8.
98. Rabe, J. P.; Sano, M.; Batchelder, D.; Kalatchev, A. A. *Journal of Microscopy* 1988, 152(2), 573.
99. Kamrava, S. J.; Zagorska, M.; Krische, B.; Soderholm, S. *Physica Scripta* 1991, 44, 112.
100. Hayashi, T.; Yamamura, H.; Nishi, T.; Kakimoto, M. *Polymer* 1992, 33(17), 3751.
101. Zhu, R.; Min, G.; Wei, Y.; Schmitt, H. J. *J. Phys. Chem.* 1992, 96, 3210.
102. Bourdieu, L.; Maaloum, M.; Silberzan, P.; Ausserre, D.; Coulon, G.; Chatenay, D. *Ann. Chim. Fr.* 1992, 17, 229.
103. Gould, S. A. C.; Drake, B.; Prater, C. B.; Weisenhorn, A. L.; Manne, S.; Hansma, H. G. *J. Vac. Sci. Technol. A* 1990, 8(1), 369.

104. Rohrer, H. In *Scanning Tunneling Microscopy and Related Methods*; Behm, R. J., Ed., Kluwer Academic Publishers; Netherlands, 1990, pp. 1-25.
105. Sarid, D.; Elings, V. J. *Vac. Sci. Technol. B* 1991, 9(2), 431.
106. Frommer, J.; Meyer, E. Z. *Phys. B - Condensed Matter* 1991, 3, S1-S9.
107. Heinzelmann, H.; Meyer, E.; Rudin, H.; Guntherodt, H. J. In *Scanning Tunneling Microscopy and Related Methods*; Behm, R. J., Ed., Kluwer Academic Publishers; Netherlands, 1990, pp. 443-467.
108. Bar, G.; Magonov, S. N.; Cantow, H. J.; Gmeiner, J.; Schwoerer, M. *Ultramicroscopy* 1992, 42-44, 644.
109. Nawaz, Z.; Cataldi, T. R. I.; Knall, J.; Somekh, R.; Pethica, J. B. *Surf. Sci.* 1992, 265, 139.
110. Lippel, P. H.; Wilson, R. J.; Miller, M. D.; Woll, Ch.; Chiang, S. *Phys. Rev. Lett.* 1989, 62(2), 171.
111. Snyder, S. R.; White, H. S. *Anal. Chem.* 1992, 64, 116R.
112. Chiang, S. In *Scanning Tunneling Microscopy I. Springer Series in Surface Sciences Vol. 20*; Guntherodt, H. J., Weisendanger, R., Eds., Springer-Verlag, Heidelberg, 1992, pp. 181-205.
113. Avouris, P. J. *Phys. Chem.* 1990, 94, 2246.
114. Schwartz, D. K.; Viswanathan, R.; Zasadzinski, J. A. N. *J. Phys. Chem.* 1992, 96, 10444.
115. Viswanathan, R.; Schwartz, D. K.; Garnaes, J.; Zasadzinski, J. A. N. *Langmuir* 1991, 8, 1603.
116. Zasadzinski, J. A. N. *Microbeam Analysis* 1991, 367.
117. Annis, B. K.; Noid, D. W.; Sumpter, B. G.; Reffner, J. R.; Wunderlich, B. *Makromol. Chem. Rapid Commun.* 1992, 13, 169.
118. Rugar, D.; Hansma, P. *Physics Today* 1990, October, 23.
119. Sarid, D. In *Scanning Force Microscopy*; Oxford University Press; New York, 1991, pp. 181-249.
120. Wickramasinghe, H. K. *Scientific American* 1991, October, 98.
121. Frommer, J. *Angew. Chem. Int. Ed. Engl.* 1992, 31, 1298.
122. Fang, J. Y.; Lu, Z. H.; Ming, G. W.; Ai, Z. M.; Wei, Y. *Physical Review A* 1992, 46(8), 4963.
123. Edinger, K.; Golzhauser, A.; Demota, K.; Woll, Ch.; Grunze, M. *Langmuir* 1993, 9, 4.

124. Marti, O.; Ribi, H. O.; Drake, B.; Albrecht, T. R.; Quate, C. F.; Hansma, P. K. *Science* **1988**, *239*, 50.
125. Snetivy, D.; Vancso, G. J.; Rutledge, G. C. *Macromolecules* **1992**, *25*, 7037.
126. Schmidt, H.; Heil, J.; Wesner, J.; Grill, W. J. *Vac. Sci. Technol. A* **1990**, *8*(1), 388.
127. Miller, R. G.; Bryant, P. J. *J. Vac. Sci. Technol. A* **1989**, *7*(4), 2879.
128. Melmed, A. J. *J. Vac. Sci. Technol. B* **1991**, *9*(2), 601.
129. Magonov, S. N.; Bar, G.; Keller, E.; Yagubskii, E. B.; Cantow, H. J. *Synth. Met.* **1991**, *40*, 247.
130. Kimura, M.; Sakurauchi, K.; Okumura, A.; Miyamura, K.; Gohshi, Y. *Analytical Sciences* **1991**, *7*, 389.
131. Hallmark, V. M.; Chiang, L. S.; Swalen, J. D.; Rabolt, J. F. *Polym. Prepr.* **1987**, *28*(2), 22.
132. Wilson, T. E.; Ogletree, D. F.; Salmeron, M. B.; Bednarski, M. D. *Langmuir* **1992**, *8*, 2588.
133. Overney, R. M.; Howald, L.; Frommer, Meyer, E; Guntherodt J. *Chem. Phys.* **1991**, *94*(12), 8441.
134. Albrecht, T. R.; Akamine, S.; Carver, R. E.; Quate, C. F. *J. Vac. Sci. Technol. A* **1990**, *8*(4), 3386.
135. Binning, G.; Smith, D. P. E. *Rev. Sci. Instrum.* **1986**, *57*(8), 1688.
136. Ducker, W. A.; Senden, T. J.; Pashley, R. M. *Nature* **1991**, 239.
137. Lyubchenko, Y. L.; Lindsay, S. M.; DeRose, J. A.; Thundat, T. J. *Vac. Sci. Technol. B* **1991**, *9*(2), 1288.
138. Wolter, O.; Bayer, T.; Greschner, J. J. *Vac. Sci. Technol. B* **1991**, *9*(2), 1353.
139. Porter, T. L.; Oden, P. I.; Caple, G. *Surf. Sci.* **1991**, *259*, 221.
140. Alexander, S.; Hellemans, L.; Marti, O.; Schneir, J.; Elings, V.; Hansma, P. K.; Longmire, M.; Gurley, J. J. *Appl. Phys.* **1988**, *65*(1), 164.
141. Goddenhenrich, T.; Lemke, H.; Hartmann, U.; Heiden, C. J. *Vac. Sci. Technol. A* **1990**, *8*, 383.
142. Neubauer, G.; Cohen, S. R.; McClelland, G. M.; Horn, D. E.; Mate, C. M. *Rev. Sci. Instrum.* **1990**, *61*, 2296.
143. McClelland, G. M.; Erlandsson, E.; Chiang, S. In *Review of Progress in Quantitative Nondestructive Evaluation, Vol. 6B*; Thompson, D. O., Chimeti, D. E., Eds.; Plenum, New York, 1987, p. 307.

144. Martin, Y.; Williams, C. C.; Wickramasinghe, H. K. *J. Appl. Phys.* **1987**, *64*, 4723.
145. Sarid, D.; Iams, D.; Weissenberger, V. *Opt. Lett.* **1988**, *13*, 1057.
146. Schonenberger, C.; Alvarado, S. F. *Rev. Sci. Instrum.* **1989**, *60*, 313.
147. Martin, Y.; Wickramasinghe, H. K. *Appl. Phys. Lett.* **1987**, *50*, 1455.
148. Schwartz, D. K.; Viswanathan, R.; Zasadzinski, J. A. N. *Langmuir* **1993**, *9*, 1384.
149. Magonov, S. N. *Applied Spectroscopy Reviews* **1993**, *28*(1&2), 1.
150. Meyer, E. *Prog. Surf. Sci.* **1993**, *41*, 3.
151. Cohen, S. R. *Ultramicroscopy* **1992**, *42-44*, 66.
152. Bashkin, M. O.; Bepalov, V. A. Emelyanov, A. V.; Inkin, V. N. Portnov, S. M.; Zimin, A. V.; Kharkevich, S. I.; Menshikov, O. D. *Ultramicroscopy* **1992**, *42-44*, 977.
153. Chi, L. F.; Anders, M.; Fuchs, H.; Johnston, R. R.; Ringsdorf, H. *Science* **1993**, *259*, 213.
154. Josefowicz, J. Y.; Maliszewskyj, N. C.; Idziak, S. H.; Heiney, P. A.; McCauley Jr., J. P.; Smith III, A. B. *Science* **1993**, *260*, 323.
155. Manivannan, A.; Nagahara, L. A.; Yanagi, H.; Kouseki, T.; Ashida, M.; Maruyama, Y.; Hashimoto, K.; Fujishima, A. *Thin Solid Films* **1993**, *226*, 6.
156. Schwartz, D. K.; Garnaes, J.; Viswanathan, R.; Chiruvolu, S.; Zasadzinski, J. A. N. *Phys. Rev. E* **1993**, *47*(1), 452.
157. Yamada, H.; Nakayama, K. *Jpn. J. Appl. Phys.* **1993**, *1*(6B), 2958.
158. Snetivy, D.; Vancso, G. J. *Langmuir* **1993**, *9*(9), 2253.
159. Tsukruk, V. V.; Reneker, D. H.; Bengs, H.; Ringsdorf, H. *Langmuir* **1993**, *9*, 2141.
160. Sun, L.; Crooks, M. *Langmuir* **1993**, *9*, 1951.
161. Binning, G.; Quate, C. *Rev. Phys. Rev. Lett.* **1986**, *12*, 1930.
162. Ulman, A. in *An Introduction to Ultrathin Organic Films*; Academic Press, Toronto, 1991.

CHAPTER 3: SURFACE-ENHANCED RAMAN SCATTERING (SERS) AND MODEL CALCULATIONS OF ENHANCEMENT FACTORS

3.1. INTRODUCTION

During normal Raman scattering only a fraction of the incident light is scattered inelastically. As a further complication, thin solid films which have monolayer or submonolayer thicknesses produce weak Raman scattering due to the small number of molecules in the incident beam. Surface-enhanced Raman scattering (SERS) is one way to improve the sensitivity of the Raman technique. Surface-enhanced Raman scattering occurs when molecules are at or near specially prepared metal substrates. The average of the Raman scattering intensity is typically increased on the order of 10^4 by SERS¹. The enhancement factor is the ratio of the scattering intensity in the presence of the SERS active substrate to the intensity that would be observed without the substrate present:

$$EF = \frac{I_{\text{SERS}}}{I_{\text{R}}} \quad (\text{equation 3.1})$$

This chapter discusses the substrates that have been used for SERS. A historical perspective is provided which connects such diverse areas as metal colloids, aerosols, light scattering and absorption, color and SERS. SERS theories which fall into two groups are presented. There are selection rules that influence the relative intensities of SERS bands. Model calculations are

carried out based on electromagnetic theory to guide the experimental selection of metal substrates for SERS in the near-IR.

There have been a number of SERS review articles and books in the literature¹⁻⁸. The first observation of SERS was reported by Fleischmann, Hendra and McQuillan⁹ for pyridine on an electrochemically roughened silver electrode. Many different metals give rise to SERS such as: Ag, Au, Cu, In, Li, Na, K, Ni, Pd, Rh, Ti, Cd, Co, Hg and Al^{3,10-11}. The SERS-active substrates are prepared in various ways and surface roughness is necessary. Metal electrodes are roughened during oxidation-reduction cycles in an electrolyte. Metal island films are produced by vacuum evaporation at elevated substrate temperatures. Cold deposited metal films are prepared with the substrate below 120K¹. Repetitive rough structures such as gratings are produced lithographically. Metal colloids which consist of metal spheres or aggregated structures are SERS-active.

It is possible to have surface-enhanced resonance Raman scattering (SERRS) when the laser excitation is in resonance with both an electronic absorption of the adsorbate and the plasmon frequency of the SERS-active substrate. Many dyes and pigments are colored and absorb light in the visible region. Surface-enhanced resonance Raman scattering was used for trace analysis of the fluorescent dye rhodamine 6G on a silver sol¹². Raman bands were observed even at a dye concentration of 4×10^{-12} M. A thin film of the pigment zinc phthalocyanine (ZnPc) on gold and silver island films produced SERRS with an enhancement on the order of 10^3 which is above that estimated for SERS alone using the 647.1 nm Kr⁺ laser line^{13,14}. In Chapter 5, additional examples will be presented of SERRS of phthalocyanines and perylenes.

Connections have been made between a number of seemingly disparate phenomena by Kerker¹⁵. Michael Faraday carried out many experiments involving colloidal metal sols. Faraday made particular note of the colors of metal sols and how finely divided metal particles aggregated and changed color when salt was added. John Tyndall was Faraday's assistant and successor. Tyndall was interested in aerosols and made a connection between the blue color of the small aerosol particles, the color of the sky and the fact that light is polarized when observed perpendicular to the incident light from the Sun. The next historical figure was Lord Rayleigh who provided the theory behind Tyndall's observations. Rayleigh derived expressions for scattering and absorption of light and realized the blue color of the sky was due to molecules in the air. The type of factors entering Rayleigh's scattering and absorption expressions included the particle diameter, the wavelength of light, and the dielectric constant. Lord Rayleigh and later Sir C. V. Raman studied sulfur sols. Raman is well known for his discovery of the effect in which a small fraction of scattered light has been shifted in frequency. Surface-enhanced Raman scattering was discovered much later in 1974⁹. Rough metal surfaces were initially used for SERS and then metal colloids. The colors of silver and gold colloids present in stained glass, Faraday sols and SERS had a common origin according to Alan Creighton¹⁵. Kerker offers the explanation that the color of sols and SERS are due to resonances¹⁵. The same Irving Langmuir, who worked on Langmuir-Blodgett films discovered that under the right conditions, an electromagnetic wave could cause electrons in metals to vibrate cooperatively leading to strong electrical fields. More will be mentioned about surface plasmons later in the next section. The electron oscillations lead to strong scattering and absorption. Color and SERS are effects which depend on particle size, morphology and dielectric function of the metal.

3.2. ELECTROMAGNETIC THEORY FOR SERS

Theories to explain SERS fall into two categories, electromagnetic (EM) and non-electromagnetic. The electromagnetic theory will be considered first. The electrons in metals such as silver, copper and gold behave like a gas. Metals have collective oscillations of the electrons which can be excited by an incident electric field and localized on the surface of a metal. The collective oscillations are surface plasmons³. In order for surface plasmons to radiate, frequency and parallel momentum must be conserved and this condition is fulfilled by metals which have surface roughness features on the order of 10-100 nm^{1,7}. Electric fields at or near the surface of the metal are greatly enhanced and localized. A molecule at or near the metal surface experiences an effective electric field due to the incident electric field from the laser and the electric field arising from the metal surface. Raman shifted radiation is produced which can also be in resonance with the surface plasmon. If the excitation wavelength and Raman scattering wavelength are not too different a double resonance is possible. There are some experimental factors that can be varied in order to obtain the greatest SERS enhancement factor. It is possible to tune into the plasmon resonance by using the appropriate laser wavelength. The dielectric constant can be changed by selecting a different metal. SERS-active substrates can be prepared with different morphologies.

Simple models for surface roughness can be used to calculate SERS enhancements factors. The simplest case is that of an isolated metal sphere. One assumption in the calculations is that the particle size is significantly smaller than the wavelength of the incident light. Campion reports the following expression for the SERS enhancement factor (EF) for a sphere⁷:

$$EF = \left[\frac{\epsilon_1(\omega_L) - \epsilon_2}{\epsilon_1(\omega_L) - 2\epsilon_2} \right]^2 \left[\frac{\epsilon_1(\omega_S) - \epsilon_2}{\epsilon_1(\omega_S) - 2\epsilon_2} \right]^2 \left(\frac{r}{r+d} \right)^{12}$$

(equation 3.2)

ϵ_1 is the dielectric function of the sphere and ϵ_2 is the dielectric function of the medium.

ω_L and ω_S are the incident and Raman scattered frequencies respectively.

r is the radius of the sphere and d is the distance of the molecule away from the sphere.

The increase in Raman scattering is roughly proportional to the fourth power of the surface-enhanced electromagnetic field. Some general features can be extracted from expression 3.2. The resonance condition is $\text{Re}\epsilon_1 = -2\epsilon_2$ at the incident or scattering frequencies. The enhancement is proportional to $(\text{Im}\epsilon_1)^{-4}$. Metals such as silver, gold and copper are good enhancers in the visible region while transition metals should work well in the ultraviolet region⁵. The distance dependence term is based on the dipole decay law. Electromagnetic theory can be checked quantitatively by measuring the distance-dependence of the SERS enhancement and this will be discussed later. The enhancement as a function of distance falls off rapidly for small particles or surface roughness features with a high radius of curvature. This equation provides an explanation for the fact that SERS intensities fall off with higher frequency shifts⁷. In practice, incident and scattering fields are not simultaneously in resonance with the surface plasmons. If particles become larger and approach the wavelength of the exciting light, the resonances are red shifted, broadened and the enhancement factor decreases⁷.

Gersten and Nitzan¹⁶ considered enhancement factors arising from molecules at or near metal spheroids of different aspect ratios. More will be mentioned about this model in the section in this chapter on model calculations. Prior to carrying out SERS experiments in Chapter 5, enhancement factor calculations were completed according to Gersten and Nitzan¹³ for various metals in the visible and near-IR region. The calculations guided the selection of the most appropriate metal(s) for island films and SERS in the near-IR. Whatever simple model is chosen, the experimentally obtained SERS-active substrates are usually more complex. For instance, aggregation takes place with metal colloids and shifts the plasmon resonance to the red. Most rough surfaces will have a distribution of particle sizes. A quantitative comparison between EM theory and experimental results is most appropriate for SERS-active substrates which have well-defined morphologies. An example would be gratings or lithographically produced structures. Electron microscopy and atomic force microscopy are valuable tools to check the substrate morphology.

Other surface-enhanced phenomena in addition to SERS are predicted by electromagnetic theory for rough metal surfaces. The photochemical decomposition of azo sulfonate compounds adsorbed on silver films has been followed¹⁷. Excimer laser pulses at 308 nm irradiated the films and surface-enhanced Raman scattering using argon ion laser excitation at 488.0 nm and 514.5 nm was used to follow the reaction products. The monitoring of photolysis in solution was hampered by the production of small amounts of fluorescent products. Fortunately the metal island film quenched the fluorescence by radiationless transfer to the metal while increasing the Raman scattering¹⁷. The distance dependence of fluorescence has been reported of a Langmuir-Blodgett monolayer of tetra-*tertiary*-butyl metal-free

phthalocyanine ((t-bu)₄H₂Pc) on silver island films with arachidic acid LB monolayer spacer layers¹⁸. The fluorescence spectrum of an LB monolayer of (t-bu)₄H₂Pc with no spacer layer on the Ag film was 200 times higher in intensity than that of an LB monolayer of (t-bu)₄H₂Pc on glass. The fluorescence enhancement factor with five monolayers of spacer was approximately 400. Two processes compete in this system, radiationless decay to the metal and local field enhancement. There are other processes such as absorption, second harmonic generation and luminescence to name a few which are enhanced by rough metal surfaces^{1,3}.

3.3. NON-ELECTROMAGNETIC THEORIES FOR SERS

An overview of the important non-electromagnetic theories for SERS follows. The theories are usually grouped under the umbrella of "chemical" enhancement mechanisms. There are some experimental observations which are difficult to explain in the context of EM theory. There are certain molecules which display a "first layer" effect. The enhancement factor for molecules in the layer adjacent to the metal surface is much higher than predicted by EM theory. Charge transfer (CT) excitations can occur between a metal and an adsorbate for specific systems and would affect the first layer only. An example would be an Ag-C₂H₄ complex which displays SERS in the visible region². An optical absorption band has been observed for this complex at 550 nm which corresponds to a charge transfer excitation of an Ag 5s state to the lowest unoccupied molecular orbital (LUMO), a π^* b_{2g} state¹⁹. Charge transfer can take place from metal to adsorbate or adsorbate to metal. Molecules such as CH₄ and C₂H₆ do not have affinity levels of the correct energy for SERS in the visible region². One way of thinking of charge transfer excitations is to make an analogy to the resonance Raman effect. The molecular polarizability

derivative tensor is changed and this causes increased Raman scattering. A resonance occurs when the laser excitation coincides with the charge transfer energy.

Molecules such as CO and N₂ have the same Raman scattering cross-section¹. Experimentally, SERS of CO on cold-deposited silver is fifty times more intense than N₂ on the same substrate²⁰. The CO band on Ag is shifted 28 cm⁻¹ from the Raman band of free CO. Nitrogen, however has a minor shift of 2 cm⁻¹ in frequency when it is adsorbed on cold-deposited Ag. The fifty-fold difference in intensity cannot be accounted for by preferred orientation of CO on Ag alone. Adsorbates on SERS-active substrates can be either physisorbed or chemisorbed. Physisorbed molecules have van der Waals type of interactions with the surface. The Raman frequencies and relative intensities are not expected to differ greatly from the adsorbate in the absence of the surface. On the other hand, chemisorbed molecules have a strong interaction with the metal leading to bond formation. The frequencies and relative intensities can be quite different from the molecule alone. The molecular electronic distribution has been changed and the molecular polarizability derivative tensor is that of the surface-adsorbate complex. The electromagnetic mechanism would operate on the surface-adsorbate complex. A second possibility is that there are two SERS mechanisms operating simultaneously. One which causes a fifty-fold increase over the other electromagnetic enhancement.

Excitation profiles are a plot of SERS intensity against excitation wavelength. Usually the intensities are calibrated with an internal standard. There have been some unusual results obtained for adsorbates on roughened

electrodes at different potentials^{21,22}. The intensity maxima occur at different potentials for different excitation wavelengths. One explanation is that the potential affects the gap between the energy levels of the metal and adsorbate². If the charge transfer is from the metal to the adsorbate, a negative potential will push the Fermi level up and lead to a red shift in the CT excitation wavelength⁷. Conversely, for CT from an adsorbate to metal, positive potentials push the Fermi level down and lead to a blue shift in the CT excitation⁷. The Raman molecular polarizability derivative, α can be expressed in terms of the Kramers-Heisenberg equation⁷:

$$\alpha = \frac{\sum_i \langle f | H | i \rangle \langle i | H | g \rangle}{(E_i - E_g) - h\nu + i\Gamma_i} + \frac{\sum_i \langle f | H | i \rangle \langle i | H | g \rangle}{(E_i - E_g) + h\nu}$$

[equation 3.3]

g , i and f are ground, intermediate and final states of the molecule. H is the Hamiltonian operator for molecule-radiation interaction. Γ_i is the natural linewidth of the intermediate state. ν is the frequency of the incident light.

The denominator becomes small and α large in equation 3.3 when $CT = h\nu = E_i - E_g$. A large molecular polarizability derivative causes increased Raman scattering and equation 3.3 is the condition for the resonance Raman effect. There would also be increased scattering due to the presence of the rough metal.

The CT (excited model) has been described in which a resonance Raman effect leads to increased Raman scattering. There are a couple of ground state charge transfer models²³⁻²⁷. In the ground state, there is some amount of charge transfer between the metal and adsorbate which is modulated by molecular vibrations^{4,23,24}. The total polarizability is affected by this electron transfer and vibrations which change the metal-adsorbate distance are influenced the most. The second ground state CT model involves vibrations that push and pull electrons to and from the metal surface and vibrationally modulate the reflectivity of the surface or Mie scattering of metal particles^{5,25-27}.

Three classes of biomolecules were deposited on silver island films in an attempt to determine short-range and classical electromagnetic contributions to SERS²⁸. The first class of adsorbates were biomolecules such as adenine and calf thymus deoxyribonucleic acid (CT-DNA) which have electronic transitions in the UV region only. Secondly, flavine adenine dinucleotide (FAD) and doxorubicin (DOX) were compounds with low coefficient of extinction electronic transitions in the visible region. The third category included β -carotene which has a high coefficient of extinction electronic transition in the visible region. The silver island films had extinction spectra with maxima from 450-660 nm depending on the thickness of the metal. The term "extinction" was used because the spectra were not corrected for scattering and reflectance. Excitation profiles were obtained for different bands of each molecule on the metal and enhancement factors calculated. The first two classes of molecules had chemical interactions with the silver surface and the Raman enhancement was short-ranged. The β -carotene on the other hand, displayed long-range enhancement characteristic of a classical electromagnetic

enhancement. The type of enhancement mechanism which is operative may depend not only on the chemical nature of the adsorbate, but also its electronic absorption²⁸. For the β -carotene, the maximum SERS enhancement occurred in the region of maximum overlap between the molecular electronic absorption and the plasmon absorption of the metal island film²⁸.

Otto et al. have described a search for SERS-active sites². The adatom hypothesis involves strong electron-photon coupling at regions of atomic scale roughness leading to electron tunneling from the metal via the adatoms to the electronic states of the adsorbate^{29,30}. Adatoms are clusters of metal atoms much smaller than the surface roughness features 10-100 nm normally discussed in regards to EM theory. Regions of atomic scale roughness (ASR) are believed to consist of clusters of five or six atoms¹. Otto et al.² also described adsorption sites of lowered affinity called "E-sites" which have extra lines compared to normal lines of the adsorbates. There are frequency shifts at the E-sites and the adsorbate is chemisorbed.

Campion⁷ has taken smooth metal surfaces with very low enhancement factors and created defects of well-known structure. Defects were created on high index faces of single crystals of silver by cutting, thermal evaporation of adatoms or by underpotential deposition. The observations were that on Ag(521), Ag(987) stepped and kinked surfaces, the Raman spectrum of physisorbed pyridine is unenhanced⁷. On Ag(540) the pyridine was chemisorbed but the Raman spectrum was not enhanced. Therefore, chemisorption alone is not sufficient to produce SERS⁷.

Moskovits has addressed challenges to the electromagnetic model¹. For instance, most EM calculations assume a molecule is physisorbed to the metal. There is no reason why one cannot consider chemisorption. The only adjustment that is necessary is to use the polarizability tensor of the metal-adsorbate complex and assume the EM field is acting on this complex. Adatoms are not necessary for SERS for the CT-model, only chemisorption sites. The intensity of adsorbates on cold deposited porous films usually increases with increasing substrate temperature and then decreases. Rather than invoking adatoms, the results can be explained by the idea that the surface structures of the films are being changed and tuned to allow EM enhancement. The weakness or absence of SERS for water on electrodes in aqueous systems can be explained by the fact that water is inherently a weak Raman scatterer and secondly the high vibrational frequency does not allow the simultaneous resonance between the incident and Raman scattered excitation and the surface plasmon¹. The saturation of the SERS effect with coverage can often be explained by the effect metal curvature has on the distance dependence of SERS. Features of low curvature produce the longest-ranged enhancement. The experiments with CO and N₂ on SERS-active surfaces have been mentioned and differences between ethylene and ethane. In the later case, there appears to be another mechanism operating on top of the EM enhancement. SERS spectra do not have to be the enhanced version of the normal Raman spectrum. This will be discussed in the section of this chapter on surface-selection rules which allow for different relative intensities of bands. Under a couple of circumstances, "forbidden" bands are also possible.

3.4 DISTANCE AND COVERAGE DEPENDENCE OF SERS ENHANCEMENT FACTOR.

The distance dependence of the SERS enhancement factor should provide evidence for either an electromagnetic mechanism or chemical mechanism. A chemical mechanism requires immediate contact with the SERS-active substrate. The electromagnetic mechanism can be relatively long-ranged depending on the substrate geometry. Murray et al.³¹⁻³³ carried out the earliest SERS distance dependence studies. The sample geometry was complex consisting of the following layers: CaF_2 underlayer / vacuum evaporated Al - Al_2O_3 / dip coated adsorbate / spin coated spacer / top vacuum evaporated Ag . The adsorbate to silver distance was not well-defined because of the protrusions in the CaF_2 layer influencing subsequent layers and enhancement could have also been due to the Al - Al_2O_3 .

SERS distance dependence results for Langmuir-Blodgett films on metal islands were reported independently by two groups^{34,35}. Cotton et al.³⁵ spaced dyes from silver island films. Kovacs et al.³⁴ used LB spacer layers of arachidic acid of well known thicknesses to separate tetra-*tertiary*-butyl metal-free phthalocyanine ((*t*-bu)₄H₂Pc) from silver and indium island films. Calculation of an absolute enhancement factor was possible by comparison with the intensity of an unenhanced spectrum of one or more LB monolayers of (*t*-bu)₄H₂Pc. Weak enhancement was observed even at 15 nm from the surface. The data in both cases^{34,35} supported the notion of an electromagnetic mechanism.

Silver island films have been prepared in UHV on sapphire substrates³⁶. At low temperatures, cyclohexane molecules were condensed on top of the metal and were used as spacer molecules for subsequent deposition of aromatic molecules such as benzene. The intensity of the Raman band assigned to C-C stretching of benzene reached a maximum at 1.3-1.7

monolayer coverage with an enhancement factor of 10^4 . When a clean silver island surface was exposed to oxygen prior to aromatic molecules, the 10^4 enhancement was lost and the long-range classical electromagnetic enhancement was observed. The explanation provided was that atomic oxygen passivates the surface by adsorbing on regions of atomic scale roughness or defects³⁶.

There have been many studies related to distance-dependence and coverage dependence using pyridine adsorbed on metal surfaces³. If chemisorption sites are present in low concentrations and are necessary, the SERS signal should have a maximum value at a low surface coverage. Adsorption of additional physisorbed species can lower the local field³. The coverage dependence of SERS of cobalt phthalocyanine (CoPc) on roughened films has been measured and the maximum intensity was observed for 0.07 monolayer³⁷. An electromagnetic model could explain the results and damping of the plasmon resonance above 0.1 monolayers. If there are no special adsorption sites then the normal EM enhancement is in effect. If molecules are adsorbed, the effect on the dielectric constant of the medium must be considered³.

3.5 SURFACE-SELECTION RULES

The frequencies and relative intensities of Raman bands of a molecule are influenced by the presence of a surface and are governed by surface selection rules³⁸. The model begins with a molecule above a smooth metal surface. The orthogonal coordinate system consists of the z-axis normal to the surface and the plane of incidence is yz. There are two possible polarizations of incident linearly polarized light, P with the electric field parallel to the plane of

incidence and S with the electric field vector perpendicular to the plane of incidence. The electric field at the surface is due to incident and reflected beams. The angle the incident beam makes with the surface normal is ϕ . The electric field components have been expressed in terms of Fresnel coefficients³:

$$E_x = (1 + r_s)E_s \quad [\text{equation 3.4}]$$

$$E_y = (r_p - 1)\cos\phi E_p \quad [\text{equation 3.5}]$$

$$E_z = (1 + r_p)\sin\phi E_p \quad [\text{equation 3.6}]$$

$$r_s = \frac{\cos\phi - (\epsilon - \sin^2\phi)^{1/2}}{\cos\phi + (\epsilon - \sin^2\phi)^{1/2}} \quad [\text{equation 3.7}]$$

$$r_p = \frac{\epsilon\cos\phi - (\epsilon - \sin^2\phi)^{1/2}}{\epsilon\cos\phi + (\epsilon - \sin^2\phi)^{1/2}} \quad [\text{equation 3.8}]$$

The Fresnel coefficients r_s and r_p are defined by equations 3.7 to 3.8¹. ϵ is the dielectric function of the metal.

The squared amplitude of the electric fields (E_{zp}^2 , E_{yp}^2 , E_{xs}^2) have been calculated for different angles of incidence (0 to 90°) with 514.5 nm excitation of silver and indium surfaces³. The conclusions are that the field parallel to the surface is small for good reflectors, the perpendicular component is strong due to the superposition of incident and reflected fields and best Raman enhancement should occur for P-polarized light at a calculated 60° angle of incidence.

Four combinations of polarizations are possible experimentally based on the polarization of the incident light and analyzed light after a 90° Raman scattering experiment: SS, PS, SP and PP. Expressions similar to 3.4 to 3.8 can be generated for scattered light. The primes ('s) in subsequent expressions indicate scattered radiation. To define this model further, the geometry of the molecule must be considered relative to the surface. The simplest case has the coordinates of the molecule and surface in common. The expressions for the four polarizations according to Moskovits¹ are given in equations 3.9 to 3.12. The molecular polarizability derivative tensor component elements are α_{ij} .

$$SS \propto |\alpha_{xx} (1+r_s) (1+r_s')|^2 \quad (\text{equation 3.9})$$

$$SP \propto |\alpha_{yx} (1+r_s) (1-r_p') \cos\phi' + \alpha_{zx} (1+r_s) (1+r_p') \sin\phi'|^2 \quad (\text{equation 3.10})$$

$$PP \propto | \{ \alpha_{yy} (r_p - 1) \cos \phi + \alpha_{yx} (1 + r_p) \sin \phi \} (1 - r_p') \cos \phi' + \\ \{ \alpha_{zy} (r_p - 1) \cos \phi + \alpha_{zz} (1 + r_p) \sin \phi \} (1 + r_p') \sin \phi' |^2$$

(equation 3.11)

$$PS \propto | \alpha_{xy} (r_p - 1) (1 + r_s') \cos \phi + \alpha_{xz} (1 + r_p) (1 + r_s') \sin \phi |^2$$

(equation 3.12)

Returning to the Fresnel coefficient expressions in 3.7 and 3.8, as $|\epsilon|$ becomes very large, which is true to the red¹, $r_s \rightarrow -1$ and $r_p \rightarrow +1$. The tangential field component of the surface becomes close to zero and the normal component of the incident field is increased. The term in PP which is related to α_{zz} remains. Raman-active modes of the molecule are observed which have a non-zero α_{zz} component. This is an example of how the relative intensities of Raman bands can be quite different for a molecule near a metal surface compared to the free molecule.

The condition necessary for the tangential field component being stronger than the normal component is that $1 / |\epsilon|$ becomes very large¹, making $r_s \rightarrow +1$ and $r_p \rightarrow -1$. Raman modes with non-vanishing α_{xx} , α_{yy} , α_{xy} are expected. Raman bands of molecules on smooth surfaces fall into three classes¹: those with α_{zz} , those with one or all of α_{xx} , α_{yy} , α_{xy} and one or both of α_{xz} and α_{yz} . The excitation profile (intensity versus wavelength) for each class of bands is different.

The next step in the development of surface selection rules is to consider molecules adsorbed on metal spheres³. If the same coordinate system exists for the molecule and the sphere, the α_{zz} components are enhanced when the excitation frequency is to the red of the plasmon frequency, followed by α_{xz} and α_{yz} components. If SERS experiments are carried out just to the blue of the plasmon frequency, all types of modes are equally enhanced appearing to violate the surface selection rule¹ in which modes which are normal to the metal surface are strong.

The surface selection rules affect the relative intensities of "allowed bands" in SERS spectrum. There are two ways to have "forbidden modes" appear in SERS spectra. Firstly, the symmetry of the adsorbate can be lowered by bonding to the surface. Secondly, a steep field gradient near the surface makes it necessary to include additional terms in the induced dipole moment expression.

The orientation of adsorbed molecules on SERS-active substrates can be determined by applying surface selection rules³⁹⁻⁴³. The orientation of low symmetry molecules on metal was calculated based on the relative intensities of $\nu_{\text{sym}}(\text{C-H})$ and $\nu_{\text{asym}}(\text{C-H})$ vibrations of methyl groups⁴³. Two assumptions must be made. The polarizability tensor should not change when a molecule is adsorbed to the surface. Therefore, relative intensities of adsorbate bands should not be due to a resonance Raman effect. The total radiation experienced by the adsorbate must be a vector sum of the normal and tangential electric field components. In general, this approach could be used for two modes of known spatial relation that have discrete frequencies. The polarizability ellipsoid changes along the adjacent carbon to methyl carbon for

the $\nu_{\text{sym}}(\text{C-H})$ mode. The $\nu_{\text{asym}}(\text{C-H})$ mode has polarizability changes in a perpendicular direction.

3.6 MODEL CALCULATIONS OF SERS ENHANCEMENT FACTORS

A computer program⁴⁴ written in FORTRAN for a VAX system was used to calculate the enhancement factor of a molecule above a prolate metal hemispheroid according to Nitzan and Gersten¹⁶. The identity of the metal hemispheroid was varied and also the excitation wavelength. Literature values of dielectric constants of metals at the excitation and scattering wavelengths were collected and input to the program. The surrounding medium was assumed to have $\epsilon_0=1$. The excitation wavelengths used as input were 488.0 nm (Ar⁺ laser), 514.5 nm (Ar⁺ laser), 647.1 nm (Kr⁺ laser) and 1064.1 nm (Nd/YAG laser).

The molecule selected for the calculations was a phthalocyanine derivative, tetra-*tertiary*-butyl metal-free phthalocyanine ((t-bu)₄H₂Pc). In the past, Langmuir-Blodgett monolayers of this material were deposited on vacuum evaporated metal island films⁴⁵⁻⁴⁷. The enhancement factors were calculated for a band which appears at a frequency shift of 686 cm⁻¹ corresponding to a macrocycle breathing mode. For the purpose of these calculations, the geometry of the hemi-spheroid was fixed with a semi-major axis of 38 nm and a semi-minor axis of 33 nm. Different values could also be input based on geometries that are possible experimentally. The enhancement factors were calculated at the top of the spheroid and to a distance 24.50 nm using 0.50 nm increments. The enhancement factor (EF) expression according to Nitzan and Gersten was¹⁶:

$$EF = |A(\omega_L)|^2 |A(\omega_S)|^2 \quad [\text{equation 3.13}]$$

ω_L is the laser excitation wavelength
 ω_S is the wavelength of scattered radiation

$$A(\omega) = 1 + L \frac{\epsilon_0 - \epsilon(\omega)}{\epsilon(\omega) - \epsilon_0 P} \quad [\text{equation 3.14}]$$

ϵ_0 is the dielectric constant of the surrounding medium
 $\epsilon(\omega)$ is the wavelength dependent dielectric constant for the metal
 L and P are geometrical factors

$$L = \frac{\xi_0 Q_1'(\xi_1)}{Q_1(\xi_0)} \quad [\text{equation 3.15}]$$

$$P = \frac{\xi_0 Q_1'(\xi_0)}{Q_1(\xi_0)} \quad [\text{equation 3.16}]$$

Q_1 is a Legendre function of the second kind

The geometry of the prolate hemi-spheroid used for the calculations is shown in Figure 3-1. The focus point f , is related to the semi-major axis b and semi-minor axis a through equation 3.17. The height above the tip of the

spheroid is H . The geometrical terms ξ_0 and ξ_1 are related to a , H and f through equations 3.18 and 3.19.

$$f = (a^2 - b^2)^{1/2} \quad [\text{equation 3.17}]$$

$$\xi_0 = a/f \quad [\text{equation 3.18}]$$

$$\xi_1 = (a + H)/f \quad [\text{equation 3.19}]$$

An example of the prolate enhancement factor output for a gold hemi-spheroid with semi-major axis=38 nm and semi-minor axis=33 nm and a laser excitation wavelength of 1064.1 nm appears in Appendix I. The enhancement factor drops rapidly from 155 for a molecule at the top of the metal to 4.48 at a distance of 24.50 nm from the metal. The first set of enhancement factor calculations were completed for (t-bu)₄H₂Pc on silver, gold and copper metal hemi-spheroids using various laser excitation wavelengths. The input parameters and calculated enhancement factors for a molecule at the top of the Ag, Au and Cu hemi-spheroids appear in Table 3-1. In the case of silver, the enhancement factor decreases with increasing wavelength. The EF was modeled to be 403 using 488.0 nm laser excitation and 151 for 1064.1 nm excitation. Gold and copper display a slightly different behavior from silver with the highest enhancement calculated for 514.5 nm excitation with EF values of 690 and 272 respectively.

Figure 3-1: Prolate hemi-spheroid geometry¹⁶ used for enhancement factor model calculation.

Figure 3-1

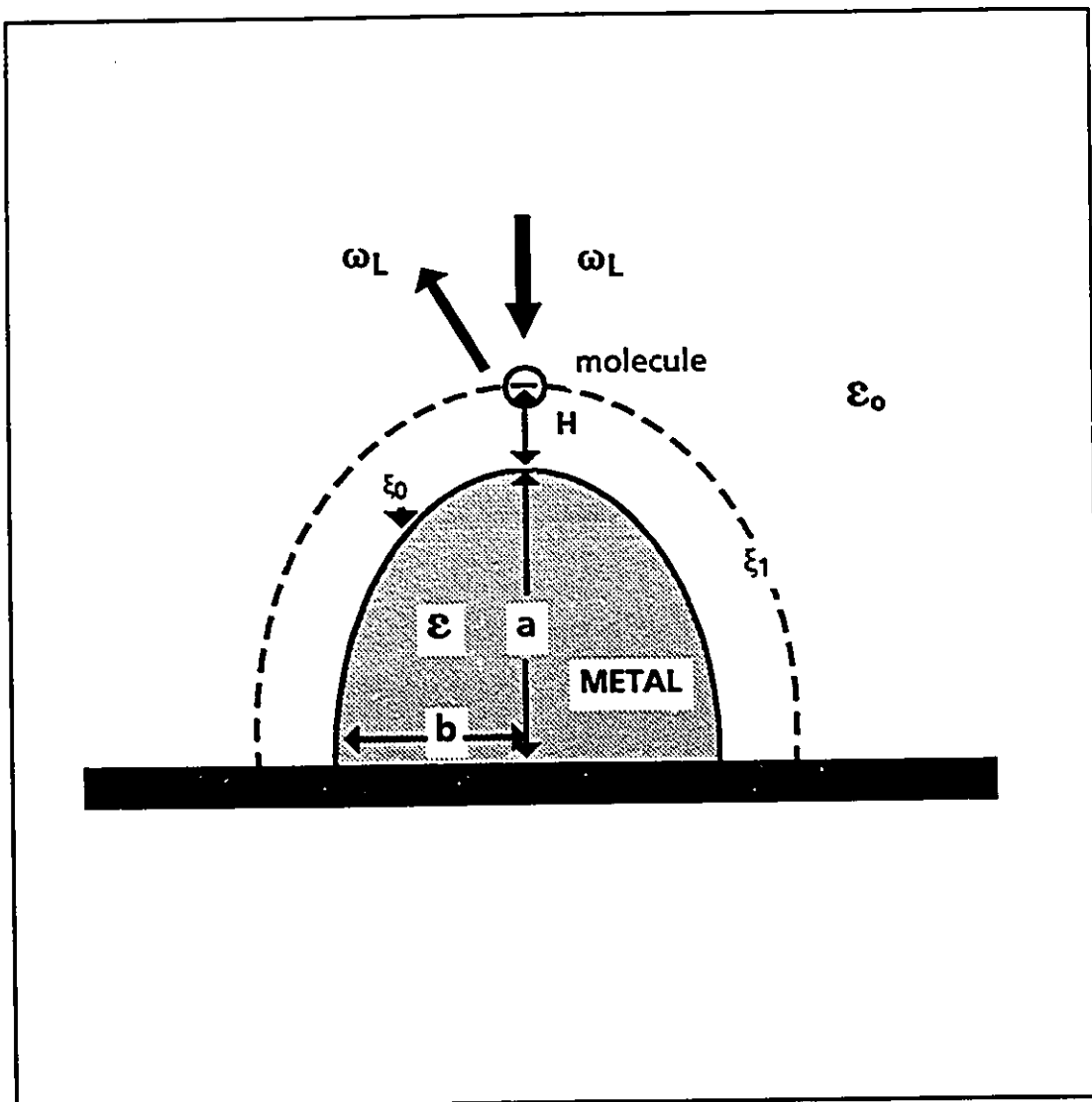


Table 3-1: Calculated Enhancement Factors for Ag, Au, Cu and Ni.

METAL	Reference for ϵ values	EF laser line = 488.0 nm	EF laser line = 514.5 nm	EF laser line = 647.1 nm	EF laser line = 1064.1 nm
Ag	Johnson & Cristy ⁴⁸	403	332	213	151
Au	"	270	690	274	155
Cu	"	253	272	268	154
Ni	Johnson & Cristy ⁴⁹	179	177	169	148

Input parameters: EF for band at shift 687 cm^{-1} ,
semimajor axis = 38 nm, semiminor axis = 33 nm.

Table 3-2: Calculated Enhancement Factors for Various Metals at 1064 nm.

METAL	Reference for ϵ values	ϵ_{Re} (1064 nm)	ϵ_{Im} (1064 nm)	ϵ_{Re} (1148 nm)	ϵ_{Im} (1148 nm)	ENHANCE- MENT FACTOR (top of spheroid)
Al	Johnson & Cristy ⁵⁰	-107	25.5	-129	27.6	140
Cr	Johnson & Cristy ⁴⁹	-0.235	25.4	0.254	26.0	127
Co	"	-25.2	33.7	-27.8	37.3	147
Cu	Johnson & Cristy ⁴⁸	-49.7	4.97	-59.9	6.56	154
Au	"	-48.8	3.64	-58.6	4.78	155
Ir	Kirillova et al. ^{51,52}	-34.2	39.2	-38.7	42.5	145
Fe	Johnson & Cristy ⁴⁹	-7.28	23.7	-8.88	25.4	143
Mn	Johnson & Cristy ⁴⁹	-9.56	29.3	-9.99	31.4	140
Mo	Moritani et al. ⁵³	-14.3	20.7	-20.6	21.1	160
Ni	Johnson & Cristy ⁴⁹	-18.7	30.1	-20.8	32.5	148
Os	Lynch et al. ⁵⁴	-6.56	14.5	-11.0	16.9	163
Pd	Johnson & Cristy ⁴⁹	-32.8	31.0	-37.1	34.3	150
Pt	Weaver ⁵⁵	-23.0	44.2	-24.5	-49.7	140
Rh	Weaver et al. ⁵⁶	-52.0	57.5	-55.8	61.5	140
Ag	Johnson & Cristy ⁴⁸	-58.3	0.610	-69.3	1.11	151
Ti	Johnson & Cristy ⁴⁹	-4.04	27.8	-4.01	29.1	134
W	Weaver et al. ⁵⁷	-5.15	22.7	-7.37	25.2	140
V	Johnson & Cristy ⁴⁹	-5.54	21.5	-8.76	22.5	144

Input parameters: laser 1064.1 nm, EF for band at shift 687 cm⁻¹ (1148 nm), semimajor axis = 38 nm, semiminor axis = 33 nm.

High SERS enhancement factors are expected for prolate hemi-spheroids with large aspect ratios, a/b . This can be accomplished for instance by depositing an underlayer of rough calcium fluoride followed by metal. There has been a report on the fabrication of tailored needle substrates for SERS⁵⁸. A base layer of latex microspheres was deposited on a glass slide and a metal was evaporated at a grazing angle to produce needles 50-75 nm in diameter with aspect ratios 5:1 or greater. It was possible to obtain good SERS spectra from ca. 100 pg of benzoic acid illuminated on the needles⁵⁸.

Table 3-2 displays the calculated enhancement factors for a series of metals excited at 1064.1 nm. The modeling indicated that a wide range of metals should give FT-SERS enhancement on the order of 10^2 . One objective of the later experimental work is to prepare vacuum evaporated metal island films as SERS-active substrates in the near-IR. The SERS-active substrates would allow signals to be obtained from thin solid organic materials which could be vacuum evaporated or deposited as Langmuir-Blodgett monolayers on the metal island film. There have been previous reports in the literature of FT-SERS on metal electrodes and colloids⁵⁹⁻⁶⁸. However, there had not been any reports of FT-SERS using metal island films. Gold and copper were selected for the preparation of metal island substrates for two reasons. Firstly, FT-SERS on Au and Cu had been demonstrated on electrodes and colloids⁶⁰⁻⁶⁹. Secondly, these materials were readily obtainable in a pure form and could be vacuum evaporated. These two metals would demonstrate the feasibility of FT-SERS on vacuum evaporated metal island films knowing that it was likely that the technique could be extended to other metals.

3.7 SUMMARY

Surface-enhanced Raman scattering (SERS) has been observed for many specially prepared rough metal surfaces. Electromagnetic theory requires collective oscillations of electrons in metals which are surface plasmons. Roughness is required to have radiative plasmons. The electric fields at or near rough metal surfaces are greatly enhanced and localized. An adsorbate experiences an effective electric field due to the incident light, Raman scattered radiation and the surface plasmons. There are chemical models which require immediate contact between the adsorbate and metal. The SERS enhancement factor has a distance and coverage dependence. Surface-selection rules have been described which affect the relative intensities of the observed SERS bands. The presence of forbidden frequencies is explained by either a lowering of adsorbate symmetry on the surface or extremely high electric field gradients. Model calculations of SERS enhancement factors were completed for various metals at visible and near-IR frequencies to guide the later experimental work.

Chapter 3: References

1. Moskovits, M. *Rev. Mod. Physics* **1985**, *57*(3), 783.
2. Otto, A.; Mzrozek, I.; Grabhorn, H.; Akeman, W. *J. Phys. Condens. Matter* **1992**, *4*, 1143.
3. Aroca, R.; Kovacs, G. J. *Vibrational Spectra and Structure* **1991**, *19*, 55.
4. Kneipp, K. *Exp. Tech. Phys.* **1990**, *38*(1), 3.
5. Creighton, J. A. in *Spectroscopy of Surfaces*; Clark, R. J. H.; Hester, R. E.; Eds.; John Wiley & Sons, Toronto, 1988, pp. 37-89.
6. Mal'shukov, A. *Stud. Phys. Theor. Chem.* **1988**, *38*, 433.
7. Campion, A.; in *Vibrational Spectroscopy of Molecules on Surfaces*; Yates, Jr., J. T.; Madey, T. E., Eds.; Plenum Press, New York, 1987, pp. 345-415.
8. Metiu, H.; in *Surface Enhanced Raman Scattering*; Chang, R. K.; Furtak, T. E., Eds.; Plenum Press, New York, 1982, pp. 1-34.
9. Fleischmann, M.; Hendra, P. J.; McQuillan, A. J. *Chem. Phys. Lett.* **1974**, *26*, 163.
10. Seki, H. *J. Electron Spectrosc.* **1986**, *39*, 289.
11. Lopez-Rios, T.; Pettenkofer, C.; Pockrand, I.; Otto, A. *Surf. Sci.* **1982**, *121*, 541.
12. Kneipp, K. *Exp. Tech. Phys.* **1988**, *36*, 161.
13. Jennings, C. A.; Aroca, R.; Hor, A. M.; Loutfy, R. O. *Anal. Chem.* **1984**, *56*, 2033.
14. Jennings, C. A.; Aroca, R.; Hor, A. M.; Loutfy, R. O. *J. Raman Spectrosc.* **1984**, *15*, 35.
15. Kerker, M. *Proc. Royal Inst. of G.B.* **1989**, *61*, 229.
16. Gersten, J.; Nitzan, A. *J. Chem. Phys.* **1980**, *73*(1), 3023.
17. Franzke, D.; Wolkaun, A. *J. Phys. Chem.* **1992**, *96*, 6377.
18. Aroca, R.; Kovacs, G. J.; Jennings, C. A.; Loutfy, R. O.; Vincett, P. S. *Langmuir* **1988**, *4*, 518.
19. McIntosh, D. F.; Ozin, G. A.; Messmer, R. P. *Inorg. Chem.* **1980**, *19*, 3321.
20. Moskovits, M.; DiLella, D. P. in *Surface Enhanced Raman Scattering*; Chang, R. K.; Furtak, T. E., Eds.; Plenum Press, New York, 1982, p. 243.

21. Billman, J.; Otto, A. *Sol. State Commun.* 1982, 44, 105.
22. McMahon, J. J.; Doherty, T. P.; Riley, J.; Babcock, G. T.; Carter, R. L. *Surf. Sci.* 1985, 158, 381.
23. Lippitsch, M. E.; Assenegg, F. R. in *Surface Studies with Lasers*; Assenegg, F. R.; Leitner, A.; Lippitsch, M. E., Eds.; Springer-Verlag, New York, 1983; p. 41.
24. Lippitsch, M. E.; Assenegg, F. R. *Phys. Rev. B.* 1984, 29, 3101.
25. Otto, A. *Surf. Sci.* 1978, 75, 392.
26. Maniv, T.; Metiu, H. *Chem. Phys. Lett.* 1981, 79, 79.
27. Abe, H.; Manzel, K.; Schulze, W.; Moskovits, M.; DiLella, D. P. *J. Chem. Phys.* 1981, 74, 792.
28. Sokolov, K.; Khodorchenko, P.; Petukhov, A.; Nabiev, I.; Chumanov, G.; Cotton, T. M. *Appl. Spectrosc.* 1993, 4, 515.
29. Billmann, J.; Kovacs, G. J.; Otto, A. *Surf. Sci.* 1980, 92, 153.
30. Otto, A. *Appl. Surf. Sci.* 1980, 6, 309.
31. Murray, C. A.; Allara, D. L.; Rhinewine, M. *Phys. Rev. Lett.* 1981, 46, 57.
32. Murray, C. A.; Allara, D. L. *J. Chem. Phys.* 1982, 76, 1290.
33. Murray, C. A.; Allara, D. L.; Hebard, A. F.; Padden, F. J., Jr. *Surf. Sci.* 1982, 119, 449.
34. Kovacs, G. J.; Loutfy, R. O.; Vincett, P. S.; Jennings, C. A.; Aroca, R. *Langmuir* 1986, 2, 689.
35. Cotton, T. M.; Uphaus, R. A.; Mobius, D. *J. Phys. Chem.* 1986, 90, 6071.
36. Mrozek, I. and Otto, A. *J. Electron Spectrosc. Relat. Phenom.* 1990, 54/55, 895.
37. Zeeman, E. J.; Carron, K. T.; Schatz, G. C.; Van Duyne, R. P. *J. Chem. Phys.* 1987, 87, 4189.
38. Moskovits, M. *J. Chem. Phys.* 1982, 77, 4408.
39. Moskovits, M.; Suh, J. S. *J. Phys. Chem.* 1984, 88, 5526.
40. Moskovits, M.; Suh, J. S. *J. phys. Chem.* 1984, 88, 1293.
41. Moskovits, M.; DiLella, D. P.; Maynard, K. J. *Langmuir* 1988, 4, 67.
42. Gao, X.; Davies, J. P.; Weaver, M. J. *J. Phys. Chem.* 1990, 94, 6858.

43. Pemberton, J. E.; Bryant, M. A.; Sobocinski, R. L.; Joa, S. L. *J. Phys. Chem.* **1992**, *96*, 3776.
44. FORTRAN program written by G. J. Kovacs, Xerox Research Centre of Canada and modified by C. A. Jennings.
45. Kovacs, G. J.; Vincett, P. S.; Sharp, J. H. *Can J. Phys.* **1985**, *63*, 346.
46. Aroca, R.; Jennings, C. A.; Kovacs, G. J.; Loutfy, R. O.; Vincett, P. S. *J. Phys. Chem.* **1985**, *89*(19), 4051.
47. Kovacs, G. J.; Loutfy, R.O.; Vincett, P. S.; Jennings, C. A.; Aroca, R. *Langmuir* **1986**, *2*, 689.
48. Johnson, P. B.; Cristy, R. W. *Phys. Rev. B.* **1972**, *6*(12), 4370.
49. Johnson, P. B.; Cristy, R. W. *Phys. Rev. B.* **1974**, *9*(12), 5056.
50. Shiles, E.; Sasaki, T.; Inokuti, M.; Smith, D. Y. *Phys. Rev. B.* **1980**, *22*, 1612.
51. Kirillova, M. M.; Bolotin, G. A.; Mayervskiy, M. V. *Fiz. Met. Metalloved* **1967**, *24*, 95.
52. Kirillova, M. M.; Bolotin, G. A.; Mayervskiy, M. V. *Phys. Met. Metallog.* **1967**, *24*(1), 91.
53. Moritani, S.; Kondo, K.; Wakai, J. *Jpn. J. Appl. Phys.* **1976**, *15*, 1549.
54. Lynch, D. W.; Olson, C. G.; Weaver, J. H., in *Physics Data*; Weaver, J. H.; Krafka, C.; Lynch, D. W.; Koch, E. E., Eds.; Fach-information s-zentrum, Karlsruhe, 1981, part 1, p. 253.
55. Weaver, J. H. *Phys. Rev. B.* **1975**, *11*, 1416.
56. Weaver, J. H.; Olson, C. G.; Lynch, D. W. *Phys. Rev. B.* **1977**, *15*, 4115.
57. Weaver, J. H.; Olson, C. G.; Lynch, D. W. *Phys. Rev. B.* **1975**, *12*, 1293.
58. Wachter, E. A.; Moore, A. K.; Haas, J. W. *Vib. Spectrosc.* **1992**, *3*, 73.
59. Sanchez-Cortes, S.; Garcia-Ramos, J. V. *J. Raman Spectrosc.* **1990**, *21*, 679.
60. Loo, B. H.; Leahey, J.; Lee, Y. G. *Chem. Phys. Lett.* **1990**, *172*(1), 33.
61. Crookell, A.; Fleischmann, M.; Hanniet, M.; Hendra, P. J. *Chemical Physics Letters* **1988**, *149*(2), 123.
62. Angel, S. M.; Myrick, M. L.; Milanovich, F. P. *Applied Spectroscopy* **1990**, *44*(2), 335.
63. Chase, D. B.; Parkinson, B. A. *Applied Spectroscopy* **1988**, *42*(7), 1186.

64. Angel, S. M.; Archibald, D. D. *Applied Spectroscopy* **1989**, *43*(6), 1097.
65. Angel, S. M.; Katz, L. F.; Archibald, D. D.; Lin, L. T.; Honigs, D. E. *Applied Spectroscopy* **1988**, *42*(8), 1327.
66. Kneipp, K.; Roth, E.; Engert, C.; Keifer, W. *Chemical Physics Letters* **1993**, *207*(4-6), 450.
67. Sockalingum, D.; Fleischmann, M.; Musiani, M. M. *Spectrochimica Acta* **1991**, *47A*(9-10), 1475.
68. Wentrup-Byrne, E.; Sarinas, S.; Fredericks, P. M. *Applied Spectroscopy* **1993**, *47*(8), 1192.

CHAPTER 4: FT-RAMAN SPECTROSCOPY OF THIN FILMS OF TITANYL PHTHALOCYANINE AND VANADYL PHTHALOCYANINE

4.1. INTRODUCTION

The FT-Raman spectra of titanyl phthalocyanine (TiOPc) and vanadyl phthalocyanine (VOPc) polymorphs are presented. The characterization of polymorphs was corroborated by X-ray data. Both materials were vacuum evaporated onto a substrate whose temperature was varied during vacuum evaporation. The FT-Raman spectra of the films formed at different temperatures are discussed. It is shown that FT-Raman is an appropriate analytical technique to distinguish between polymorphic forms.

Phthalocyanines (Pcs) have a wide range of applications. Some Pcs exhibit near-IR photosensitivity and could be used in conjunction with laser diodes in high-speed printers. A typical photoreceptor structure consisting of a conductive substrate, a charge generator layer and a charge transport layer has been given in Chapter 1. Optional layers in the photoreceptor include an adhesive layer, blocking layer and an overcoat. The phthalocyanine is part of the charge generator layer and is normally in the form of a dispersion in a polymeric binder. The types of phthalocyanines considered for this application are: X-metal-free phthalocyanine ($X-H_2Pc$)¹⁻³; trivalent metal-Pcs such as chloroaluminum phthalocyanine ($AlPcCl$)⁴, chloroindium phthalocyanine ($InPcCl$)^{5,6}; and tetravalent metal-Pcs such as vanadyl phthalocyanine (VOPc)⁷ and titanyl phthalocyanine (TiOPc)⁸. Third-order non-linear optical susceptibilities have been measured for three polymorphs of TiOPc⁹.

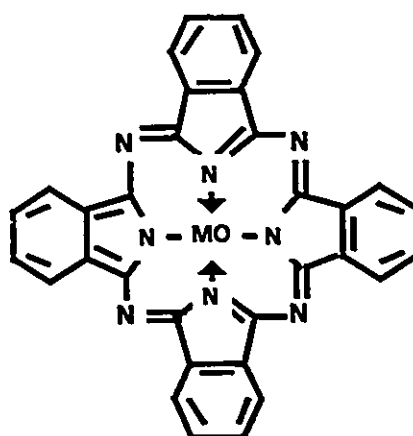
Candidates for non-linear optical waveguides include VOPc, substituted tetra-*tertiary*-butylphthalocyanines and TiOPc¹⁰. Properties such as photosensitivity and non-linear optical effects are influenced by molecular packing and orientation.

Figure 4-1 gives the molecular structure of a tetravalent metal-phthalocyanine such as TiOPc and VOPc. Both TiOPc and VOPc belong to the C_{4v} symmetry point group.

Several crystalline polymorphic forms of titanyl phthalocyanine exist and the nomenclature will be introduced here. Polymorphs can be identified on the basis of their X-ray powder diffraction patterns shown in Figure 4-2 for type I, type II, type III and type IV TiOPc. Single crystal structures of type I and type II TiOPc have been reported by Hiller and others¹¹. Type I is monoclinic with four molecules per unit cell and space group $P2_1/c$ while type II is triclinic with two molecules per unit cell and space group $P-1$. Single crystals of type III and type IV have not been obtained, therefore no single crystal structure has been reported. Rietveld refinement was used to solve crystal structures of TiOPc from X-ray powder diffraction data¹². The results for type I and type II TiOPc were obtained by comparing the data with known crystal structures¹¹. The most probable crystal structure for type IV TiOPc has been proposed¹². The best fit structure by Rietveld refinement for type IV TiOPc was a triclinic unit cell with two molecules per unit cell and space group $P-1$ [12]. Enokida has described the preparation and properties of five polymorphs of TiOPc; α , β , γ , δ and an amorphous form⁸.

Figure 4-1: Molecular structure of TiOPc and VOPc.

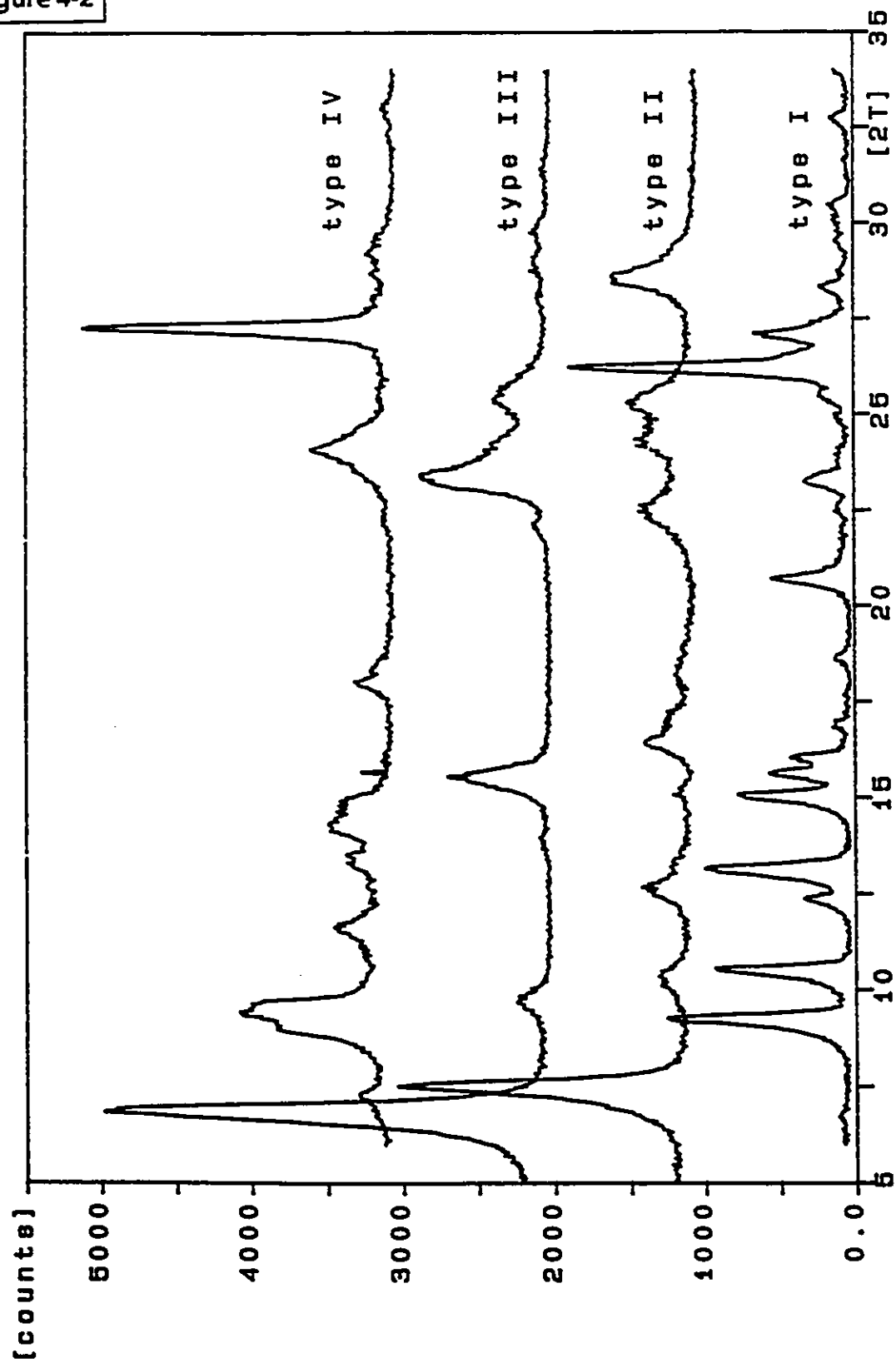
Figure 4-1



M = Ti or V

Figure 4-2: X-ray powder diffraction patterns of TiOPc polymorphs (types I, II, III, & IV).

Figure 4-2



Three polymorphic forms (I, II and III) have been observed for vanadyl phthalocyanine¹³. Type I occurs if VOPc is vacuum deposited onto fused quartz at room temperature. Type II is prepared by crystal growth from solvents such as quinoline or 1-chloronaphthalene, crystal growth from vapor or by heating phase I to 200°C and above. Phase III occurs if a melt at 610°C is quenched. Type II VOPc is triclinic with $P\bar{1}$ symmetry and two molecules per unit cell. A single crystal X-ray structure is not available for type I VOPc.

In the following sections of Chapter 4, the Raman results for a series of thin solid films of TiOPc and VOPc deposited onto a substrate whose temperature was varied during vacuum evaporation are discussed. The technique selected for the study was Fourier-transform Raman spectroscopy (FT-Raman) that provides spontaneous Raman spectra for pigments strongly absorbing in the visible spectral region. The objective of the work was to provide an analytical method to distinguish the different polymorphic forms of these important materials.

4.2. EXPERIMENTAL

4.2.1. Preparation of TiOPc, VOPc and Vacuum Evaporation of Films.

Titanyl phthalocyanine was synthesized by refluxing 1,3-diiminoisoindoline and titanium butoxide in chloronaphthalene followed by washing with boiling *N, N*-dimethylformamide and methanol¹⁴. The pigment was further purified by a train sublimation process¹⁵. An amorphous TiOPc reference film was prepared by vacuum evaporation with the substrate at room temperature. A type II reference film was prepared by vacuum

evaporation with the substrate held at 95°C and subsequent exposure to cyclohexanone vapor for two minutes outside the vacuum chamber. The polymorphic conversion to obtain type IV TiOPc has been described in the patent literature¹⁶. The procedure for preparing VOPc from vanadium pentoxide and phthalonitrile has also been described in a patent¹⁷.

Corning 7059, 1" X 3" glass slides were coated on one-side with vacuum grease (Dow Corning, # 4 Compound) and placed against the substrate holder. The vacuum evaporations were carried out in a Vacuum Generators (VG) UHV system from a quartz boat containing either the TiOPc or VOPc powder. The background pressure was typically 9×10^{-5} to 1×10^{-4} Pa. The sample holder was temperature controlled using either liquid nitrogen for cooling or electrical heating to achieve substrate temperatures from -30°C to 240°C. The film deposition rate was 0.8 to 1.0 nm / second. The film thickness was monitored with a Kronos, Inc., Model QM311 thickness monitor during the deposition. The final thickness was 100 nm for films in the TiOPc and VOPc temperature series and 600 nm for the TiOPc reference films.

4.2.2. X-Ray Powder Diffraction.

Thin film X-ray powder diffraction patterns (XRPD) were collected by a Philips 1710 X-ray powder diffraction system modified with parallel beam optics on the diffraction side. The system used CuK α radiation ($\lambda=0.1542$ nm) and contained a pulse light analyzer and graphite monochromator. The data were collected at an incidence beam angle of 1.0 degree using a step size of 0.1 degrees and count time of 10 seconds at each step.

4.2.3. FT-Raman Spectroscopy.

A Bomem Ramspec 150 spectrophotometer with a Nd/YAG laser emitting at 1064.1 nm and an InGaAs detector were used to acquire FT-Raman spectra. The system had a Michelson interferometer and was interfaced to a NEC Powermate computer. Bomem Easy Software was used to collect the data and files were imported to Spectra Calc (Galactic Industries Corp.). All Raman files were ratioed against an instrument response curve. A back-scattering geometry was used with resolution set at 4 cm^{-1} . Typically 525 scans were averaged requiring 50 minutes to collect the data. The laser power at the sample was 0.75 watt for the 600 nm amorphous TiOPc reference film, 0.025 watt for the type I TiOPc solid sample, 0.10 watt for the 600 nm type II TiOPc reference film, and 0.025 watt for the type IV TiOPc solid sample. The laser power for 100 nm vacuum evaporated films of both TiOPc and VOPc was 1.82 watts.

4.3. RESULTS AND DISCUSSION

The FT-Raman spectra of a 600 nm film of amorphous TiOPc on glass (evaporated at room temperature), type I TiOPc solid in a melting point capillary tube, a 600 nm film of type II TiOPc on glass (evaporated at 95°C and subsequently exposed to cyclohexanone vapor for 2 minutes), and type IV TiOPc solid in a melting point capillary tube appear in Figure 4-3 and can be considered reference materials. Table 4-1 lists the frequencies and intensities of these polymorphs of TiOPc and band assignments are given. The Raman bands have been assigned using model compounds such as benzene¹⁸, pyrrole¹⁹, indole²⁰ and porphyrin²¹. Titanyl phthalocyanine belongs to the point group C_{4v} and since there are 58 atoms, 168 vibrations are expected. The total irreducible representation consists of the following species: $\Gamma = 23a_1 +$

19a₂ + 21b₁ + 21b₂ + 42e (doubly degenerate). Based on C_{4v} symmetry, the a₁ and e species are both Raman and IR active, while b₁ and b₂ species are Raman active only. The a₂ species are neither Raman nor IR active.

Raman depolarization ratios in thin solid films can be used to interpret the symmetry type of observed bands. The theory has been developed in a previous paper²² for thin solid films. Three sets of cartesian coordinates are required, one each for the laboratory, substrate and molecule. The laboratory coordinates describe the laser and collection of Raman scattered light. The substrate position is defined by an angle β between the incident laser beam and substrate normal. Finally the molecular orientation with respect to the substrate is defined by three Euler angles, ϕ , Θ , and Ψ . Transformations are carried out to go from molecular to substrate coordinates and then from substrate to laboratory coordinates. Four polarizations of light SS, SP, PS and PP are available experimentally by adjusting a polarizer at the output of the laser and an analyzer after the sample. A computer program can be used to generate theoretical curves for the value of the depolarization ratio SS/SP as a function of the experimental angle β and molecular stacking angle Θ for a particular symmetry type, a₁, b₁, b₂ or e. The experimentally measured depolarization ratio is then compared with theoretical curves to assist in the assignment of the symmetry type. The SS/SP depolarization ratio has been experimentally measured for TiOPc thin solid films on glass using the 647.1 nm Kr⁺ laser line and was compared with theoretical values²³. The symmetry types listed in Table 4-1 were based on the values of the SS/SP depolarization ratios and on the activity of the vibrations in the Raman and IR spectra.

Figure 4-3: FT-Raman spectra of various polymorphs of TiOPc.
a) 600 nm amorphous film
b) solid type I
c) 600 nm type II film
d) solid type IV

Figure 4-3

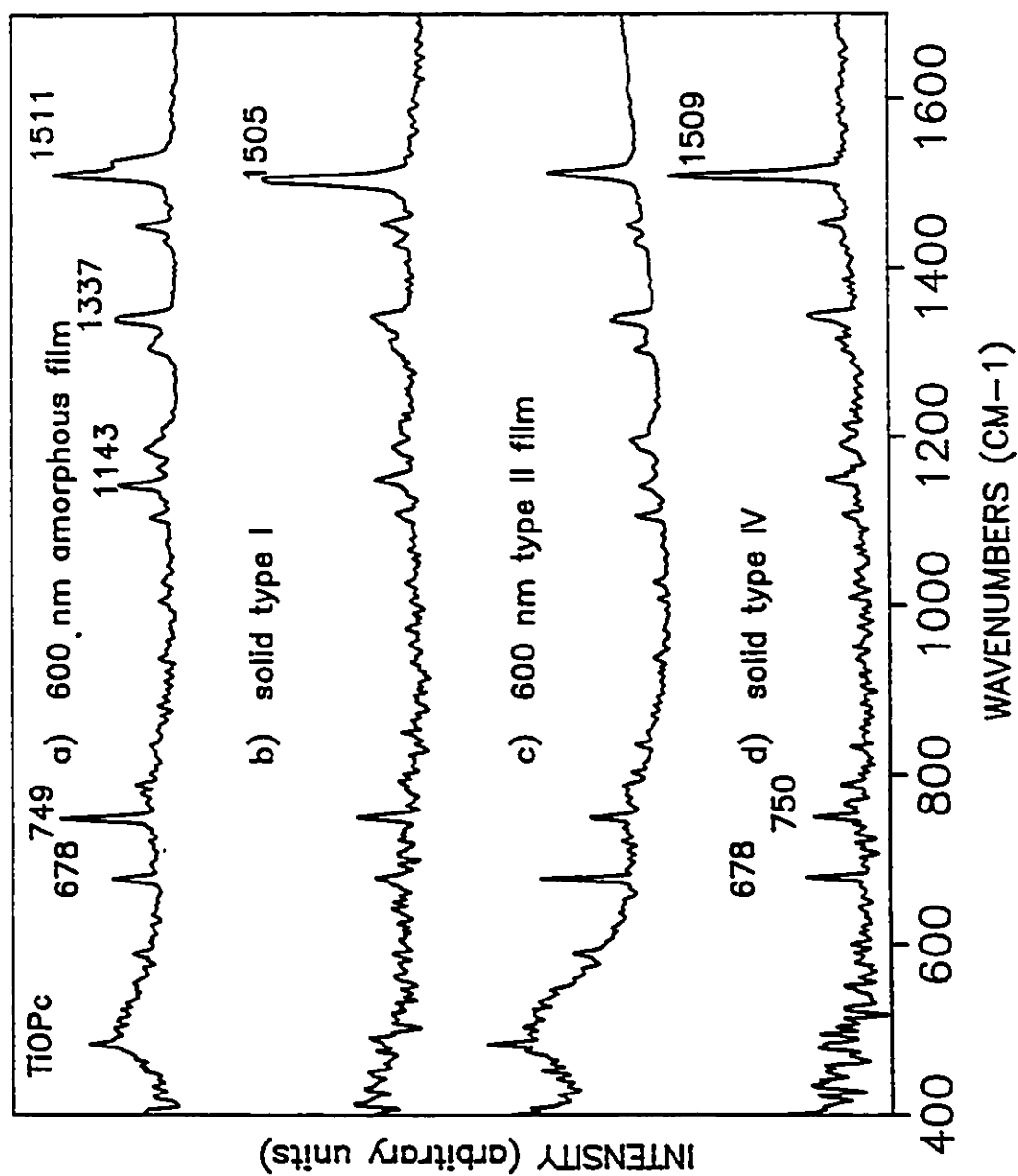


Table 4-1: FT-Raman Frequencies of Selected TiOPc Polymorphs

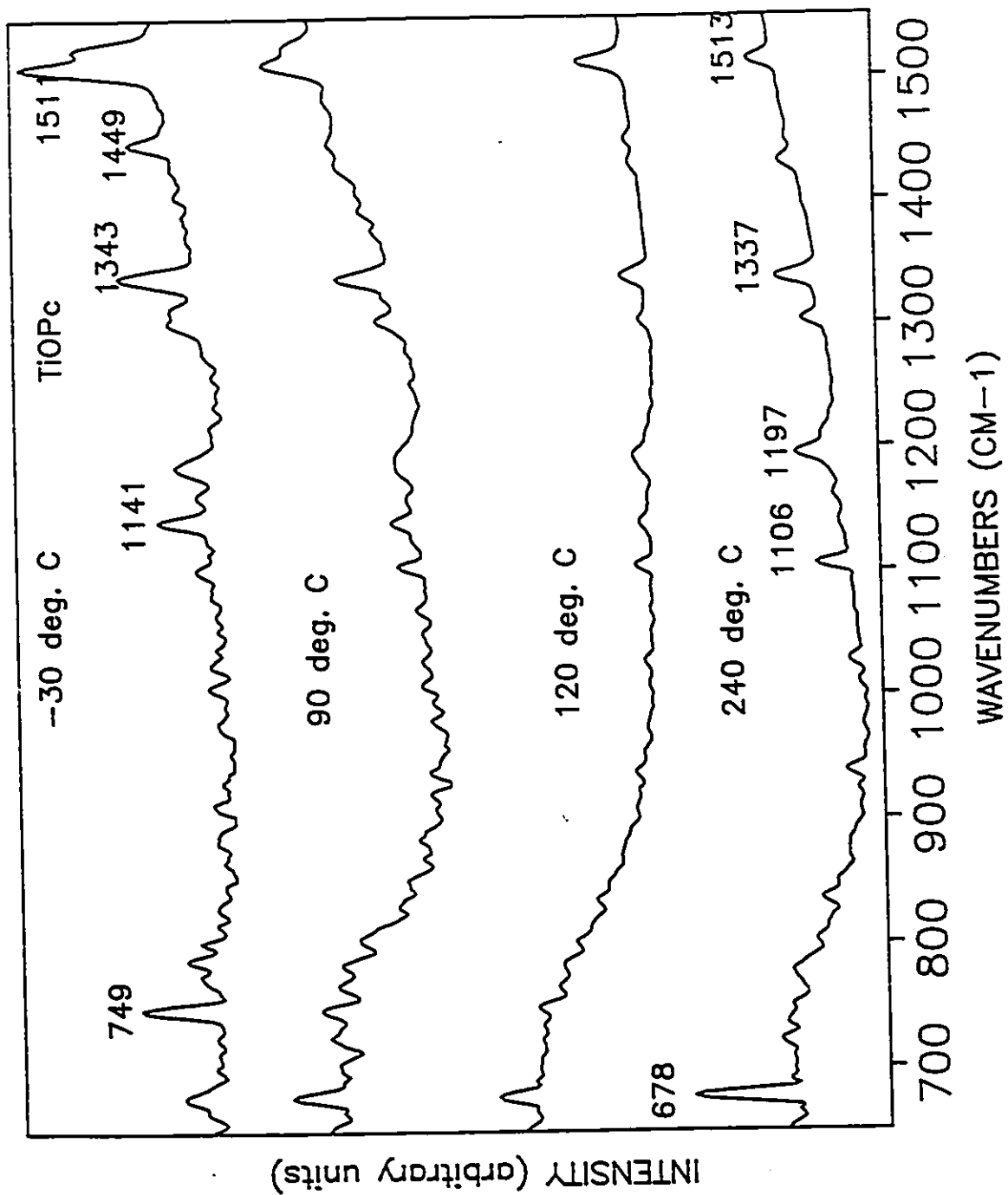
600 nm RT amorphous film (cm ⁻¹)	Type I solid in capillary tube (cm ⁻¹)	600 nm film type II (cm ⁻¹)	Type IV solid in capillary tube (cm ⁻¹)	Assignments
1524	-----	-----	-----	C-N pyrrole stretch, a ₁
1511	1505	1513	1509	benzene (ν_{19a}), a ₁
1449	1453	1450	1453	-----
1432	1428	1429	-----	isoindole stretch, a ₁
1337	1343	1340	-----	pyrrole stretch, a ₁
1305	1312	1303	1316	C-H bend
1206	1213	-----	-----	C-H bend
1185	1187	1192	1191	C-H bend
1164	-----	-----	-----	C-H bend
1143	1147	1141	1148	pyrrole ring breathing
1104	1108	1105	1108	C-H bend
1027	-----	-----	-----	C-H bend
1006	-----	-----	-----	C-H bend, a ₁
938	-----	-----	-----	
-----	-----	836	834	macrocycle stretch, a ₁
789	-----	-----	788	macrocycle stretch
-----	-----	-----	767	
749	751	750	750	benzene (ν_1), e
678	680	678	678	macrocycle breathing, a ₁
589	-----	590	-----	benzene radical
483	-----	483	-----	isoindole ring def.

Titanyl phthalocyanine polymorphs display subtle differences in the FT-Raman spectra in the region around 1500 cm^{-1} . The amorphous film has a very strong band at 1511 cm^{-1} and a shoulder at 1524 cm^{-1} . Types I, II and IV have a single strong band in the range 1505 cm^{-1} to 1513 cm^{-1} . The CN stretching vibration in pyrrole¹⁹ occurs at 1530 cm^{-1} . Vibrations normally associated with carbon-carbon stretching in benzene rings from 1565 cm^{-1} to 1620 cm^{-1} were extremely weak or absent. Carbon-hydrogen stretching bands normally not seen in the Raman spectrum also were not observed in the FT-Raman spectra because they do not cause significant changes in the polarizability of the large TiOPc molecule. The macrocycle refers to the inner core of the phthalocyanine which consists of sixteen alternating carbon and nitrogen atoms which are conjugated. Titanyl phthalocyanine polymorphs have slightly different infrared spectra⁸. The most sensitive regions to polymorphic form⁸ were 700-800 cm^{-1} and 1600-2000 cm^{-1} .

FT-Raman spectra of 100 nm TiOPc films covering a substrate temperature range of -30°C to 240°C during vacuum evaporation appear in Figure 4-4. The Raman scattering of these films was quite weak. In the region of 470 cm^{-1} , a large background was present due to the Corning glass slide. Substrate temperatures of -30°C to room temperature produced the same polymorphic form with a visible absorption band at 720 nm and X-ray diffraction results indicating amorphous TiOPc. As the temperature was increased, the stable type II TiOPc was formed with a typical X-ray peak at $2\theta=7.5^\circ$. Pure type II TiOPc at 102°C has a characteristic Raman band at 1513 cm^{-1} which is not split as observed for the amorphous form.

Figure 4-4: FT-Raman spectra of 100 nm TiOPc films deposited with various substrate temperatures.

Figure 4-4



Vanadyl phthalocyanine also belongs to the C_{4v} point group and 168 vibrations are expected. Again the a_1 , e , b_1 and b_2 species are Raman active. FT-Raman spectra of 100 nm vacuum evaporated VOPc films on glass at room temperature, 90°C, 210°C and 240°C are shown in Figure 4-5. Assignments of observed FT-Raman bands are shown in Table 4-2. Vanadyl phthalocyanine films have a pyrrole C-N stretch at 1522 cm^{-1} to 1525 cm^{-1} while type I, II and IV TiOPc polymorphs exhibit the pyrrole C-N stretch at 1505 cm^{-1} to 1513 cm^{-1} . However, amorphous TiOPc films have a band at 1511 cm^{-1} with a shoulder at 1524 cm^{-1} .

At room temperature, the VOPc film was amorphous and above 200°C the type II polymorphic form was present. The relative intensities of FT-Raman bands for the room temperature VOPc film and the 240°C VOPc film were quite different. At room temperature, the 1522 cm^{-1} peak (C-N pyrrole stretch) was more intense than the 680 cm^{-1} one (macrocycle breathing). At 240°C, the intensities were reversed. The intensity of the 753 cm^{-1} band (benzene breathing) decreased with increasing temperature. The peak at 785 cm^{-1} (room temperature) gave way to a peak at 778 cm^{-1} (240°C). Minor changes with temperature occurred in the C-H bands in the 1200 cm^{-1} region.

Figure 4-5: FT-Raman spectra of 100 nm VOPc films deposited with various substrate temperatures.

Figure 4-5

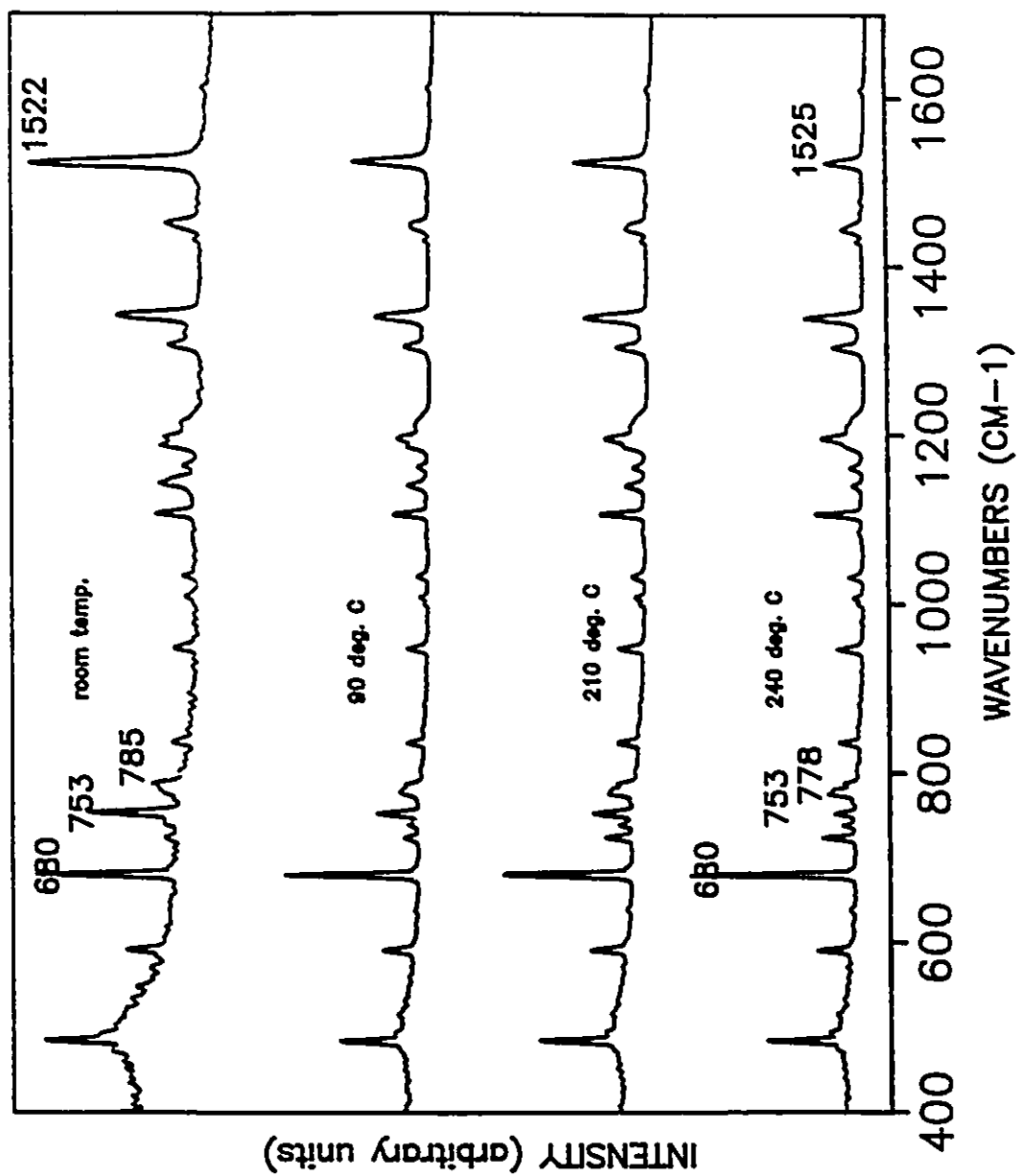


Table 4-2: FT-Raman Frequencies and Relative Intensities of VOPc films.

VOPc film room temperature		Assignment	VOPc film deposited on 240°C substrate	
Frequency (cm ⁻¹)	Relative Intensity		Frequency (cm ⁻¹)	Relative Intensity
		C=C stretch benzene	1611	(2)
1522	(100)	C-N pyrrole stretch	1525	(22)
1451	(19)	isoindole stretch	1445	(11)
1432	(2)	isoindole stretch	1432	(24)
1341	(48)	pyrrole ring stretch	1339	(34)
1307	(19)	C-H	1305	(33)
1210	(6)	C-H	1210	shoulder
1197	(7)	C-H	1197	(24)
1187	(13)	C-H		
1162	(5)	C-H	1162	(7)
1143	(21)	pyrrole ring breathing	1141	(5)
1106	(23)	C-H	1108	(5)
1033	(8)	C-H	1033	(8)
1008	(7)		1008	(5)
948	(13)		948	(15)
836	(11)	macrocycle stretching	836	(12)
785	(16)	macrocycle stretching	778	(18)
753	(53)	benzene (ν_1)	753	(11)
740	(7)		740	(6)
724	(7)	C-H wagg	724	(19)
680	(81)	macrocycle breathing	680	(100)
591	(21)	benzene radial	591	(20)
485	(41)	isoindole ring deformation	485	(46)

4.4 CONCLUSIONS

FT-Raman spectra have been obtained for 100 nm vacuum evaporated films of TiOPc and VOPc with substrate temperatures ranging from -30°C to 240°C. The observed frequencies have been assigned to specific vibrations for both of these phthalocyanines. Titanyl phthalocyanine forms in an amorphous form when evaporated onto substrates held at -30°C to room temperature. Pure type II TiOPc forms with substrate temperatures from 102°C to 240°C. Titanyl phthalocyanine type I, II and IV polymorphs can be distinguished on the basis of slight changes in the FT-Raman spectrum, most notably in the C-N pyrrole stretching region. Vanadyl phthalocyanine forms in an amorphous form on room temperature substrates and as type II on substrates above 200°C. There were changes in band frequencies and relative intensities between the VOPc FT-Raman spectra obtained from room temperature films and from films produced at 240°C. TiOPc or VOPc can be identified on the basis of the FT-Raman spectrum. The FT-Raman scattering intensity was weak in general for these thin solid vacuum evaporated films. To improve the signal intensity a thin film could be deposited on a substrate which gives surface-enhanced Raman scattering in the near-IR^{24,25}.

Chapter 4: References

1. Cheng, Y. C.; Loutfy, R. O. *J. Chem. Phys.* **1980**, 73(6), 2902.
2. Hor, A. M.; Loutfy, R. O.; Hsaio, C. *Appl. Phys. Lett.* **1983**, 42(2), 165.
3. Loutfy, R. O.; McIntyre, L.F. *Can. J. Chem.* **1983**, 61, 72.
4. Rieke, P. C.; Armstrong, N. R. *J. Am. Chem. Soc.* **1984**, 106(1), 47.
5. Loutfy, R. O.; Hor, A. M.; Rucklidge, A. *J. Imag. Sci.* **1987**, 31(1), 31.
6. Loutfy, R. O.; Hsaio, C. K.; Hor, A. M.; DiPaola-Baranyi, G. *J. Imag. Sci.* **1985**, 29(4), 148.
7. Grammatica, S.; Mort, J. *Appl. Phys. Lett.* **1981**, 38(6), 445.
8. Enokida, T.; Hirohashi, R.; Nakamura, T. *J. Imag. Sci.* **1990**, 34(6), 234.
9. Nalwa, H. S.; Hari, S.; Saito, T.; Kakuta, A.; Atsushi, I. T. *J. Phys. Chem.* **1993**, 97(41), 10515.
- 10a. Hosoda, M.; Wada, T.; Yamada, A.; Garito, A. F.; Sasabe, H. *Jpn. J. Appl. Phys., Part I* **1990**, 30(8), 1715.
- 10b. Hosoda, M.; Wada, T.; Yamada, A.; Garito, A. F.; Sasabe, H. *Jpn. J. Appl. Phys., Part II* **1991**, 30(8B), L1486-L1488.
11. Hiller, W.; Straehle, J.; Kobel, W.; Hanack, M. Z. *Krist.* **1982**, 159, 173.
12. Bluhm, T. L.; Mayo, J. D.; Hamer, G. K.; Martin, T. I. *Proc. SPIE-Int. Soc. Opt. Eng.* **1992**, 1670 (Color Hard Copy Graphic Arts), 160.
13. Griffiths, C. H.; Walker, M. S.; Goldstein, P. *Mol. Cryst. Liq. Cryst.* **1976**, 33, 149.
14. U.S. Patent 5,189,155; Mayo, J. D.; Bluhm, T. L.; Hsaio, C. K.; Martin, T. I.; Hor, A., Xerox Corporation, 1993.
15. Wagner, H.; Loutfy, R. O.; Hsaio, C. K. *J. Mater. Sci.* **1982**, 17, 278.
16. U.S. Patent 5,166,339; Duff, J. M.; Mayo, J. D.; Hsaio, C.; Hor, A.; Bluhm, T. L.; Hamer, G. K.; Kazmaier, P. M., Xerox Corporation, 1992.
17. U.S. Patent 4,771,133; Liebermann, G.; Hor, A.; Toth, A., Xerox Corporation, 1987.
18. Shimanouchi, T.; Matsura, H.; Ogawa, Y.; Harada, I. *J. Phys. Chem. Ref. Data* **1981**, 9(4), 1149.
19. Lautie, A.; Novak, A. *J. Chim. Phys. Physiochim. Biol.* **1972**, 69(9), 1332.

20. Lautie, A.; Lautie, M. F.; Gruger, A.; Fakhri, S. A. *Spectrochim. Acta* **1980**, *36A*, 85.
21. Kitagawa, T.; Abe, M.; Kyogoku, Y.; Ogoshi, H.; Watanabe, E. and Yoshida, Z. *J. Phys. Chem.* **1976**, *80*, 1181.
22. Aroca, R.; Jennings, C. A.; Loutfy, R. O.; Hor, A. *J. Phys. Chem.* **1986**, *90*, 5255.
23. Elahresh, M.; *Fourth Year Research Project*, University of Windsor, **1991**.
24. Jennings, C. A.; Kovacs, G. J.; Aroca, R. *J. Phys. Chem.* **1992**, *96*, 1340.
25. Jennings, C. A.; Kovacs, G. J.; Aroca, R. *Langmuir* **1993**, *9*(8), 2151.

CHAPTER 5: FOURIER TRANSFORM SURFACE-ENHANCED RAMAN SCATTERING OF EVAPORATED FILMS AND MONOLAYERS

5.1. INTRODUCTION

Surface-enhanced Raman scattering (SERS) of molecular species on metal island films of Au, and Au films roughened with underlayers of CaF_2 , was obtained using the near-infrared excitation line of the Nd:YAG laser at 1064.1 nm. The molecular species were vanadyl phthalocyanine (VOPc) and 3,4:9,10-perylenetetracarboxylic dianhydride (PTCDA), which were coated onto the Au surfaces as thin vacuum evaporated layers. An enhancement factor of about 100 was obtained for the electromagnetic enhancement. Demonstration of the infrared SERS effect for the two macrocycle molecules is presented and comparisons are made with previous SERS results obtained with visible light excitation. This is the first reported observation of SERS from metal island films with excitation in the infrared region.

Fourier transform surface-enhanced Raman scattering for a single Langmuir-Blodgett (LB) monolayer on a gold island film and on a copper island film using near-IR excitation at 1064.1 nm is reported here for the first time. FT-SERS was also observed for a thin vacuum evaporated film of vanadyl phthalocyanine on a copper substrate. Similar attempts to obtain FT-SERS from vacuum evaporated VOPc on GaAs and $\text{Ga}_{0.7}\text{Al}_{0.3}\text{As}$ semiconductor substrates were not successful. The types of LB monolayers used were copper tetra-*tertiary*-butyl-phthalocyanine (CuTTPc), a mixed monolayer of arachidic acid / asymmetrically substituted diphtalocyanine (PcLuPct), and *N*-pentyl-*N'*-

ethyl-3,4:9,10-perylenetetracarboxylic diimide (PPTCDE). For comparison, surface-enhanced resonance Raman scattering (SERRS) spectra were obtained using visible laser excitation in resonance with both an electronic absorption of the LB material and the surface plasmons of either the copper or gold metal island films. In all cases, the LB material was physisorbed on the metal with the electromagnetic mechanism leading to FT-SERS. The results illustrate the FT-Raman application to submicron thin solid films.

Fourier transform (FT) Raman spectroscopy is a recent addition to the long list of Raman spectroscopic techniques^{1,2}. The FT-Raman system consisted of a Michelson interferometer and an appropriate detector for inelastic light scattered from a sample excited with a Nd:YAG laser operating at 1064.1 nm. A major advantage of the technique for practical applications is the fact it is "fluorescence-free". The intensity of non-resonant scattered light is very weak for thin solid vacuum evaporated films or Langmuir-Blodgett (LB) monolayers due to the small amount of material present. Very few compounds have absorption in the near-infrared which rules out the use of the resonance Raman (RR) effect to increase the intensity of scattering in this region. One approach to increase the scattering is to deposit thin films on a metal island substrate to obtain Fourier transform surface-enhanced Raman scattering (FT-SERS).

Chapter 5 discusses vacuum evaporated vanadyl phthalocyanine (VOPc) and 3,4:9,10-perylenetetracarboxylic dianhydride (PTCDA) films on gold island substrates³. The recently published results for VOPc on a copper island film as well as FT-SERS of single Langmuir-Blodgett monolayers of phthalocyanine and perylene derivatives on copper and gold island films appear here also⁴. S E R S 5

was the first of a number of new techniques, encompassed under the general name of surface-enhanced spectroscopy. In the visible region of the spectrum, SERS is now a common analytical technique routinely used, for instance, in biochemistry⁶ and electrochemistry⁷. Experiments are generally carried out on rough surfaces with the appropriate dielectric constant and shape, as required by the electromagnetic enhancement⁸; Ag, Au and Cu are the surfaces largely used. Infrared FT-SERS of pyridine on Cu and Au electrodes⁹ and 3-picoline and 3-chloropyridine on a copper electrode¹⁰ were demonstrated. Very large enhancement factors of 10^5 - 10^6 and 9×10^6 , respectively, were estimated. These are two of the very few reports on FT-SERS, and there were no previous reports of FT-SERS on metal island films. Other reports on FT-SERS include investigations of pyridine, ferricyanide and ferrocyanide ions on Cu, Ag and Au surfaces and electrodes^{11,12}, of pyridine on Ag and Au electrodes¹³, of dyes and pyridyls on Au and Cu colloids¹⁴, and of pyridine and ruthenium complexes on Cu and Au colloids¹⁵. The electromagnetic model used as a predictive theory for planning infrared SERS experiments, indicated that metal and semiconductor surfaces could be used for Raman enhancement.

There have been cases in the literature of SERS experiments on non-metallic surfaces using visible laser excitation. Roughness-induced SERS appeared for surface carbon on PbTe and was thought to involve interband transitions of the PbTe¹⁶. SERS has been observed for copper phthalocyanine (CuPc) vacuum evaporated onto GaP particles¹⁷. Lines due to CuPc and GaP were enhanced, and the enhancement factor depended on the particle size¹⁷. SERS occurred at a semiconductor-electrolyte interface for I₂ adsorbed on a TiO₂ electrode¹⁸. Ueba presented a theory for Raman scattering from an adsorbed molecule on a semiconductor¹⁹. Excitonic or interband excitations of

the semiconductor can be coupled to the electronic excited states of an adsorbed molecule¹⁹. A measurement of the excitation profile of the Raman scattering intensity can be used to determine which mechanism is operating¹⁹. In this chapter, a thin layer of VOPc was vacuum evaporated on GaAs and Ga_{0.7}Al_{0.3}As surfaces in order to explore possible enhancement of the Raman signal with the near-IR excitation frequency.

The three general classes of LB monolayers transferred to FT-SERS substrates included a substituted metal phthalocyanine, a substituted lanthanide diphthalocyanine, and a perylene derivative. The substituted metal phthalocyanine was copper tetra-*tert*-butylphthalocyanine (CuTTPc). The preparation of a lightly substituted metal-free phthalocyanine has been discussed by Kovacs et al²⁰. Similarly, electrical and structural properties of an LB film of CuTTPc have been reported by Hann et al²¹. A mixed monolayer of CuTTPc reversibly adsorbs NO₂/N₂O₄ and is a candidate for a phthalocyanine-based sensor²².

Lanthanide diphthalocyanines have interesting semiconductive and electrochromic properties²³⁻²⁵. The second type of LB monolayer used for FT-SERS is an asymmetrically substituted lutetium diphthalocyanine. Four *tert*-butyl groups are present at the 4, 4', 4'', 4''' positions of one of the Pc rings (PcLuPct). The vibrational characterization of lutetium, ytterbium, dysprosium and holmium diphthalocyanines (LuPc₂, YbPc₂, DyPc₂, HoPc₂) was reported previously for vacuum evaporated films and LB monolayers^{26,27}. The interaction of diphthalocyanine LB films with NO₂/N₂O₄ gas mixtures has also been documented²⁷⁻²⁹.

Langmuir-Blodgett monolayers of *N*-pentyl-*N'*-ethyl-3,4:9,10-perylenetetracarboxylic diimide (PPTCDE) and other perylene derivatives were candidates for FT-SERS on metal islands. Akers has reported vibrational spectra of vacuum evaporated perylenetetracarboxylic dianhydride (PTCDA) and perylenetetracarboxylic diimide (PTCDI)^{30,31}. SERS and SERRS results for PTCDA and a diimide were presented in a separate report³². SERS results were also published for LB films of *N*-octyl-*N'*-isobutyl-3,4:9,10-perylenetetracarboxylic diimide³³. Electronic and vibrational spectra of LB monolayers of *N*-octyl-3,4-perylenedicarboximide (PDCI) appear in the literature³⁴. LB monolayers of *N*-hexyl-3,4:9,10-perylenetetracarboxylic monoimide (HPTCO) and *N*-hexyl-*N'*-ethyl-3,4:9,10-perylenetetracarboxylic diimide (HPTCDE) display surface-enhanced fluorescence on silver islands³⁵. Energy transfer has been shown to take place between LB multilayers consisting of perylene derivatives as donors and LuPc₂ as the acceptor³⁶.

5.2 EXPERIMENTAL

5.2.1. Vacuum Evaporation of Metal Island Films and Thin Organic Films.

Evaporated thin films were prepared in a Vacuum Generators DPUHV12 vacuum system. Film thicknesses were monitored using a Kronos Inc. Model QM-311 quartz crystal oscillator. Gold was obtained as fine casting grains of 99.99% purity from Johnson Matthey and Co. Ltd., and the copper was Balzers of 99.9% purity with a grain size of 0.2-0.7 mm. The copper and gold films were evaporated at 0.1 nm/s under a pressure of 1.8×10^{-4} Pa from a tungsten boat to a thickness of 20 nm onto Corning 7059 glass slides held at 200°C. Dow Corning No. 4 compound, a high-vacuum silicone grease, was applied to the back of the slide to ensure good thermal contact with the substrate heater.

After evaporation of the copper or gold, the vacuum grease was carefully removed from the back of the slide with a swab soaked in methanol.

A sample of a 20 nm gold film evaporated onto Corning 7059 glass held at 200°C was examined without further treatment using a Hitachi Model S-4000 field emission scanning electron microscope (FESEM). An accelerating voltage of 3 kV was used with the specimen at 0° angle of tilt.

A 3 nm film of vanadyl phthalocyanine was vacuum evaporated onto a 20 nm gold film at 0.1 nm/s under a pressure of 3.2×10^{-4} Pa from a quartz crucible. The synthesis of the VOPc has already been described in Chapter 4. A 3 nm vacuum evaporated film of VOPc on a 20 nm copper island film was prepared in a similar manner. A 3 nm film of 3,4:9,10-perylenetetracarboxylic dianhydride (PTCDA) was vacuum evaporated onto a 20 nm gold film at 0.1 nm/s under a pressure of 3.7×10^{-4} Pa from a quartz crucible. A sample of PTCDA was provided by Professor Nagao and the synthesis has been reported³⁷.

A substrate with surface roughness was prepared by first depositing calcium fluoride, 20 nm Au and then finally 3 nm VOPc. Optical grade calcium fluoride (Alfa Products) was vacuum evaporated to a 250 nm thickness at 0.3 nm/s at 1.4×10^{-4} Pa initial pressure onto Corning 7059 glass slides held at room temperature. A layer of 20 nm Au was vacuum evaporated onto the CaF₂ at a rate of 0.1 nm/s under a pressure 3.0×10^{-4} Pa with the substrate at room temperature. Finally a top layer of 3 nm of VOPc was vacuum evaporated under a pressure of 2.4×10^{-4} Pa again with the substrate at room temperature.

5.2.2. Preparation of Nonmetallic Substrates.

Non-metallic surfaces were prepared for FT-SERS. A gallium arsenide (GaAs) substrate of {100} orientation from Sumitomo Electric Industries Ltd. was used with a surface finish consisting of both sides lapped followed by one side polished, the other etched. A 3 nm film of VOPc was vacuum evaporated at a rate of 0.1 nm / s under a pressure of 2×10^{-4} Pa from a quartz crucible onto each side of the GaAs separately. A second FT-SERS non-metallic surface consisted of a similar GaAs substrate as above with metallorganic chemical vapor deposited (MOCVD) epitaxial layers on top. The subsequent layers were a 1.7 μm thick GaAs buffer layer followed by a 4.65 μm thick $\text{Ga}_{0.7}\text{Al}_{0.3}\text{As}$ layer. A 3 nm film of VOPc was vacuum evaporated on the top $\text{Ga}_{0.7}\text{Al}_{0.3}\text{As}$ layer with conditions as stated previously.

5.2.3. Preparation of Langmuir-Blodgett Films.

The copper tetra-*tertiary*-butylphthalocyanine (CuTTPc) was kindly provided by Dr. Tomilova from the Organic Intermediates and Dyes Institute of the Academy of Sciences of the USSR in Moscow. A solution of 4.40×10^{-4} M CuTTPc in toluene (Eastman Kodak ACS Spectro grade) was prepared and 100 μL spread onto the subphase of a Fromherz circular type Langmuir-Blodgett trough³⁸. For the subphase Milli-Q water with one additional distillation was used at ambient temperature ($\sim 23^\circ\text{C}$) and without further treatment ($\text{pH} \sim 6.3$). A Fromherz trough and dipper, housed in a glove box on a terrazzo vibration-free table were used for film compression and transfer to substrates. The monolayer was compressed at 4×10^{-3} $\text{nm}^2/\text{molecule/s}$ and the film was transferred at 6 mm/min onto the gold film on Corning 7059 glass by Z-type deposition at a constant pressure of 10 mN/m.

The synthesis of an asymmetrically substituted bisphthalocyanine PcLuPct has been reported³⁹. The LB film solution consisted of a 1:10 molar ratio (PcLuPct:arachidic acid) in chloroform. It was necessary to add arachidic acid to obtain good transfer to the substrate. The subphase was maintained at 15°C and transfer was carried out at 3 mm/min with a constant pressure of 15 mN/m to the 20 nm thick gold and copper island films on Corning 7059 glass by Z type deposition. These LB films were prepared in a Lauda Langmuir film balance equipped with the Lauda Film lift FL-1 electronically controlled dipping device.

The *N*-pentyl-*N'*-ethyl-3,4:9,10-perylenetetracarboxylic diimide (PPTCDE) was synthesized and purified by Professor Nagao³⁷. The PPTCDE solution was 3.6×10^{-5} M in chloroform and 4 mL were spread on the Fromherz trough. The PPTCDE was compressed at a rate of 1×10^{-3} nm²/molecule/second and transferred to metal island substrates at 35 mN/m constant pressure. The slide was removed from the trough at 3.6 mm/min and gave Z type deposition.

5.2.4 Raman Systems and UV-visible Spectrophotometer.

A Bomem Ramspec 150 spectrophotometer with a Nd/YAG laser emitting at 1064.1 nm and an InGaAs detector were used to acquire the FT-Raman spectra. The system had a Michelson interferometer and was interfaced to a NEC Powermate 286 Plus computer. Bomem Easy (version 1.45) software was used to collect the data and files were imported to Spectra Calc™ (Galactic Industries Corp.). All Raman files were ratioed against an instrument response curve. A backscattering geometry was used with resolution set at 4 cm⁻¹.

The incident power of the Nd/YAG laser onto the samples were (a) 1.82 W onto the 200 nm VOPc film, (b) 3.5 W onto the 200 nm PTCDA film, (c) 0.61 W

onto the 3 nm PTCDA on 20 nm Au (200°C) film, 0.290 W onto the 3 nm VOPc on 20 nm Au (200°C), 0.290 W onto the 3 nm VOPc on glass film, (f) 0.117 W onto the 3 nm VOPc on 20 nm Au on 250 nm CaF₂ film, (g) 0.070 W onto the 3 nm VOPc on 20 nm Cu (200°C), (h) 0.440 W onto the single LB monolayer of CuTTPc on 20 nm Au (200°C), (i) 0.017 W onto the mixed LB monolayer of 1:10 PcLuPct / arachidic acid on 20 nm Au (200°C), and (j) 0.343 W onto the single LB monolayer of PPTCDE on 20 nm Au (200°C). Typically 525 scans were averaged, requiring 50 minutes to collect the data.

Samples were compared where possible by putting single and multiple layers all on the same slide. For example, on one slide there was a region with VOPc on Au and another region of VOPc on glass only. The slide was aligned with the laser beam focussed onto the VOPc on Au region, and a spectrum was collected. Next, the slide was translated horizontally so the laser beam focussed on the VOPc on glass only region, and scans were collected. It was necessary to collect 2500 scans from a 3 nm VOPc film on glass to acquire the signal needed to calculate the SERS enhancement factor. To calculate the enhancement factors, the signal-to-noise ratios (S/N) were calculated as the square roots of the number of scans both for the VOPc film on glass and for the VOPc film on the roughened Au substrate. The enhancement factor is then given as the ratio of the band heights corrected for the S/N ratios and for the incident laser powers.

A Spectra Physics model 2020 Kr⁺ laser provided the 647.1 nm laser line with 50 mW of s-polarized light at the sample. A rotating sample cell was used to prevent laser damage to LB films. The typical spectral band pass was 4 cm⁻¹ and Raman shifts were measured with a Spex-1403 double monochromator.

The 514.5 nm line of a Spectra Physics Ar⁺ laser was used for the PPTCDE compound on gold.

Electronic spectra were measured in the region 200-1100 nm using a Shimidzu UV-160 spectrophotometer with a glass slide as a reference.

5.3 RESULTS AND DISCUSSION

5.3.1. SERS-active Surfaces for the Near-IR.

It is widely accepted that an electromagnetic enhancement of the Raman signal may be achieved on rough surfaces of certain metals and semiconductors¹⁰. The role of the surface roughness is to couple the incident field of the exciting radiation to the surface plasmons, enhancing the local optical field and efficiency of light scattering, absorption, and fluorescence. Experiments have shown that signal enhancement of 3 and 4 orders of magnitude could be obtained from this effect in the visible region⁴⁰. Calculations of enhancement factors also give an optimum value of $\sim 10^4$ for the average enhancement on Ag⁴¹. Metal island films used for experiments with visible light excitation were approximated as spheroidal particles, and those with dimensions in the range 10-100 nm produced the strongest enhancement⁴².

In the quasi-static limit, $r/\lambda \ll 1$, where r is the radius of a metal sphere, only the dipole surface modes are excited by the plane-wave field, and the enhancement of the field is due to the accumulation of electromagnetic energy in the local plasma oscillations. For most metals used in SERS the maximum enhancement lies in the visible region. Using the same metals (Ag, Au and Cu), the design of a SERS active metal surface for the infrared region

requires an increase in the particle size in order to tune the film plasmon frequency to the exciting laser line. The question arises as to the effect of particle size and particle interactions on the enhancing properties of the film. In general, increasing the particle size and packing of metal particles would also increase the damping of local plasma oscillations, inhibiting the enhancing ability of the film⁴³. The latter discussion implies that only a very modest enhancement should be expected from metal island films of Ag, Cu, and Au evaporated onto glass substrates (held at an elevated temperature of $\sim 200^{\circ}\text{C}$) with a mass thickness sufficient to provide a measurable value of light absorption in the near-infrared region.

Gold has a dielectric constant value that gives plasmon absorption in the red region of the visible spectrum for a mass thickness of only 4 nm. Therefore, metal island films of Au of 15-25 nm mass thickness give considerable absorption in the 1000 nm region as shown in Figure 5-1. Au films deposited onto glass substrates held at 200°C produced an enhanced Raman signal. An electron micrograph of the 20 nm Au film is shown in Figure 5-2. The rough Au surface contains metal islands that are on average larger than 100 nm, with a high packing density.

SERS spectra were obtained with several Au island films, but the 20 nm film produced the largest enhancement factor. Copper films were also deposited onto glass substrates held at 200°C and the best enhancement was observed with 20 nm mass thickness films. In an attempt to increase the enhancement factor observed for FT-SERS from Au, 20 nm of Au was evaporated onto CaF_2 underlayers. This surface improved the enhancement by a factor of 2 over that of the evaporated Au island film.

Figure 5-1: Absorption spectrum of a 20 nm Au island film on glass.

Figure 5-1

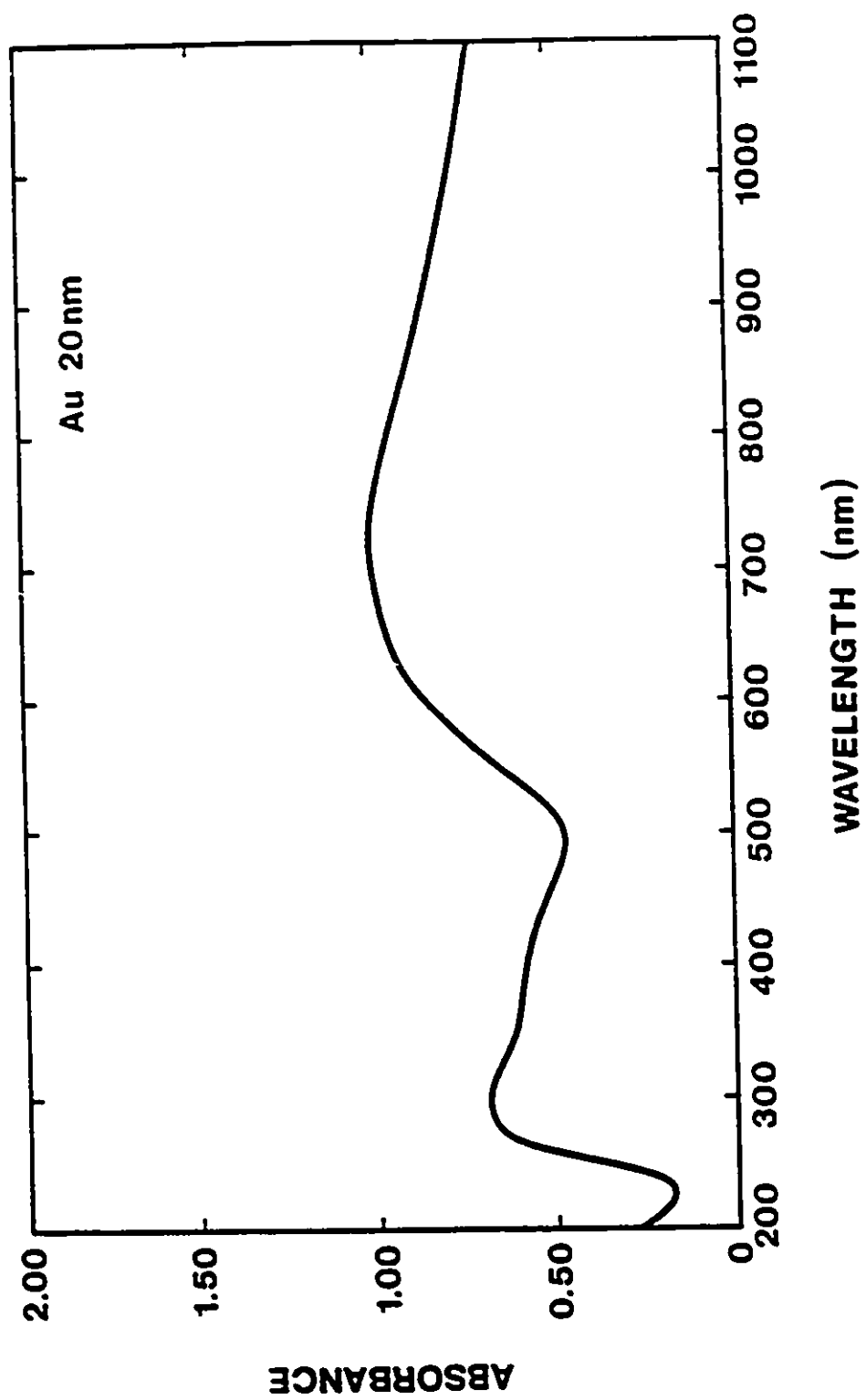
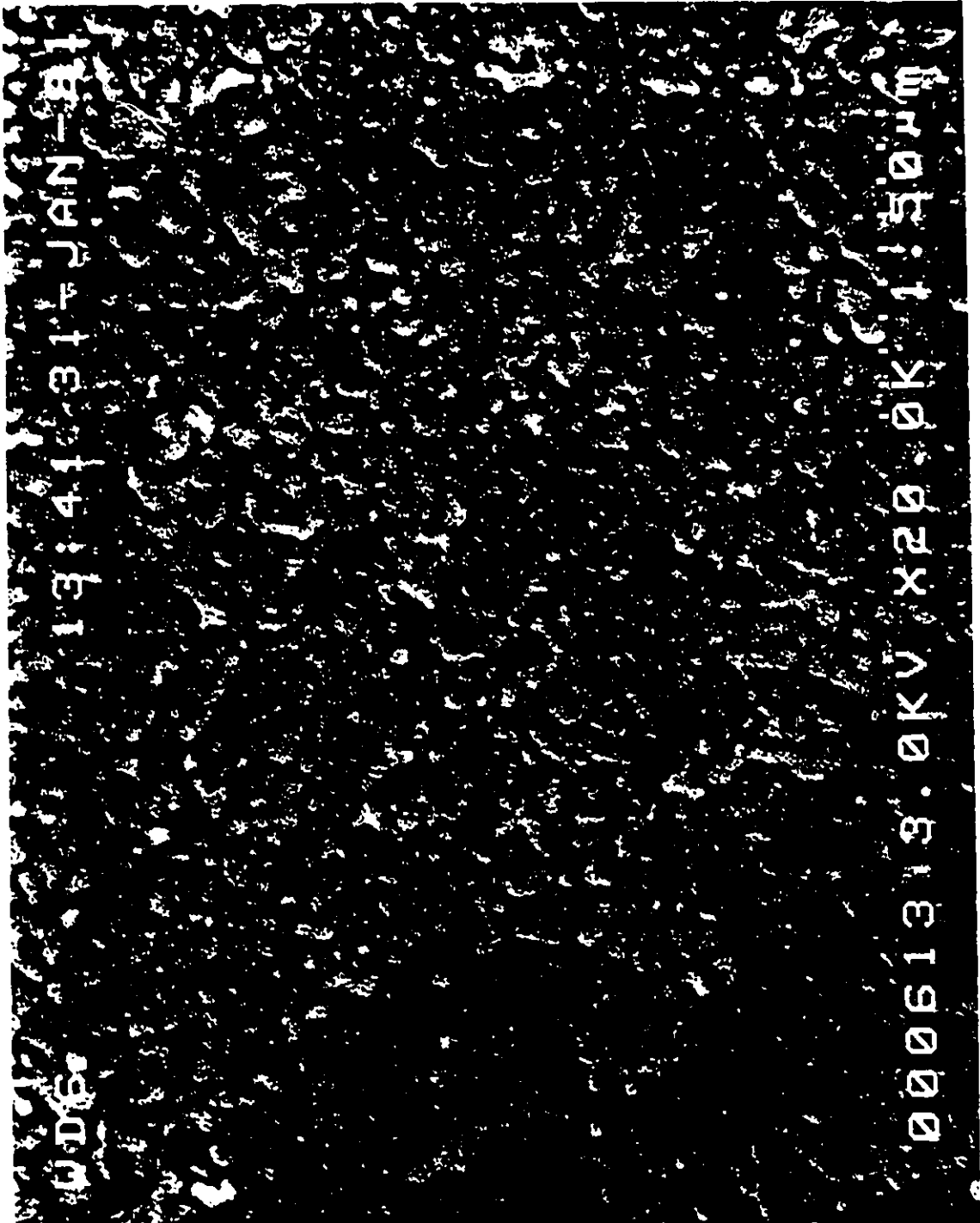


Figure 5-2: Field emission scanning electron micrograph of a 20 nm Au island film on glass.

Figure S-2



The island films of Au consist largely of oblate islands. However, it is known from previous experimental results⁴⁴ that CaF₂ underlayers are very jagged structures which provide a more prolate character to the bumps (roughness) of the covering metal film. Murray and Allara⁴⁴ used two different sample configurations consisting of Si/CaF₂/Al+oxide/Raman scatterer molecule/optional polymer spacer/Ag and Si/Al+oxide/Raman scatterer molecule/optional polymer spacer/Ag, for visible SERS experiments. Our sample configuration consisted of Corning 7059 glass/CaF₂/Au/organic film. FT-SERS was obtained using near-IR laser excitation at 1064.1 nm.

5.3.2 UV-Vis absorption spectra of VOPc and PTCDA. FT-SERS on gold island films.

The molecular structure of VOPc appeared in Figure 4-1. The structure of 3,4:9,10-perylenetetracarboxylic dianhydride (PTCDA) is given in Figure 5-3. Absorption spectra of thin solid films of the molecular pigments used in the SERS experiments are given in Figures 5-4 and 5-5. It can be seen that there was no molecular electronic absorption beyond 850 nm; therefore, the FT-Raman results correspond to spontaneous Raman spectra. Both VOPc and PTCDA have been characterized spectroscopically, and for which SERS and (SERRS) visible spectra were previously reported^{32,45}. The FT-SERS spectrum of a 3 nm VOPc film on a 20 nm Au island film is given in Figure 5-6, where for comparison the FT-Raman spectrum of a 200 nm solid film of VOPc is included. An enhancement factor (EF) of ~50 was estimated by comparison of the FT-SERS signal with the signal obtained from the reference film. The EF found for the 20 nm Au film on CaF₂ was ~100. The FT-SERS spectrum is the enhanced version of the FT-Raman spectrum of the film, and there are no frequency shifts or noticeable intensity changes.

Figure 5-3: Molecular structure of 3,4:9,10-perylenetetracarboxylic dianhydride (PTCDA).

Figure 5-3

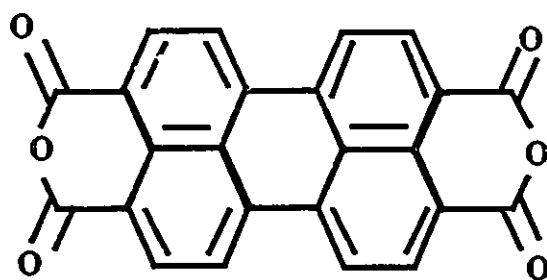


Figure 5-4: Electronic absorption spectrum of a 100 nm evaporated film of VOPc on glass.

Figure 5-4

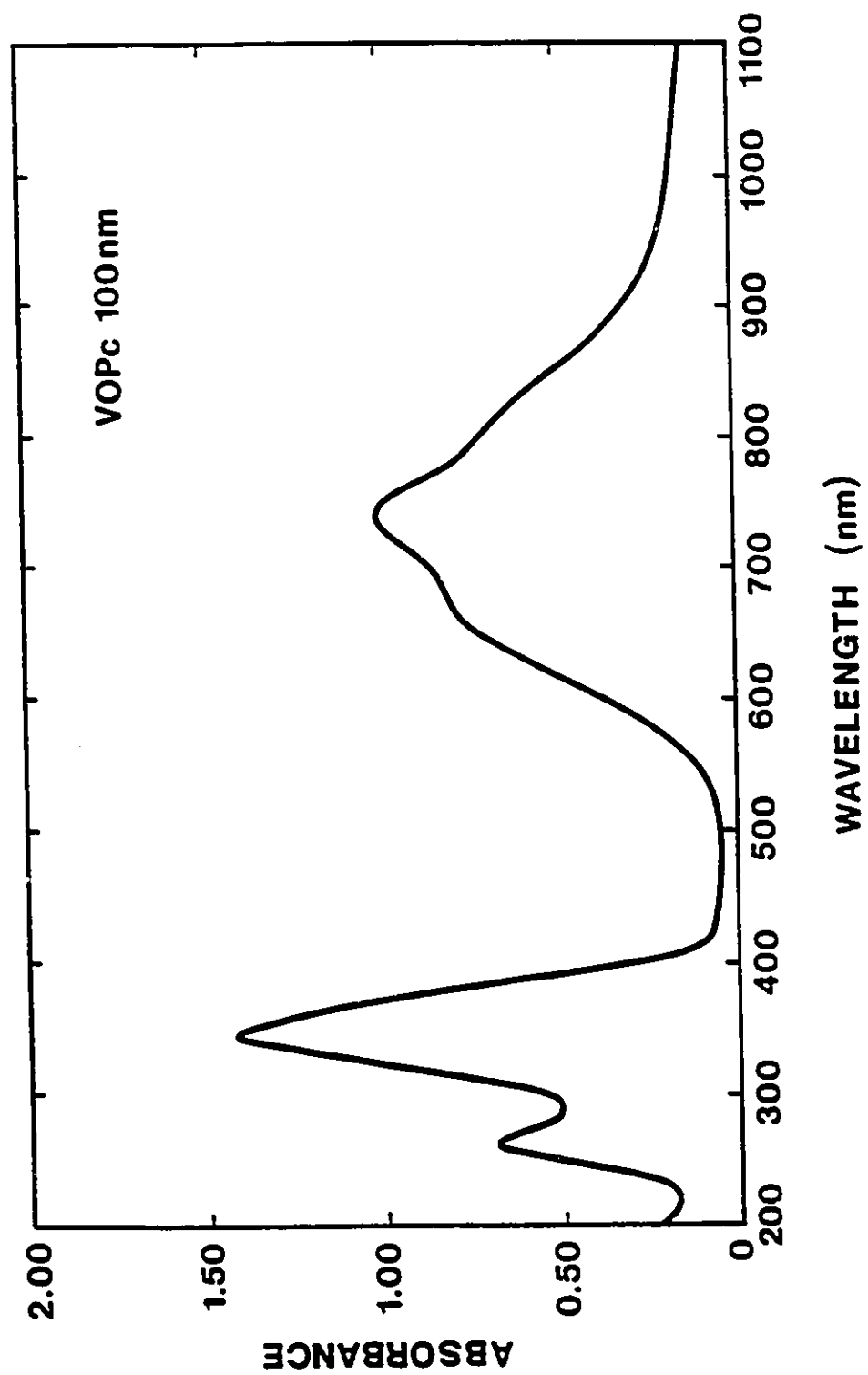
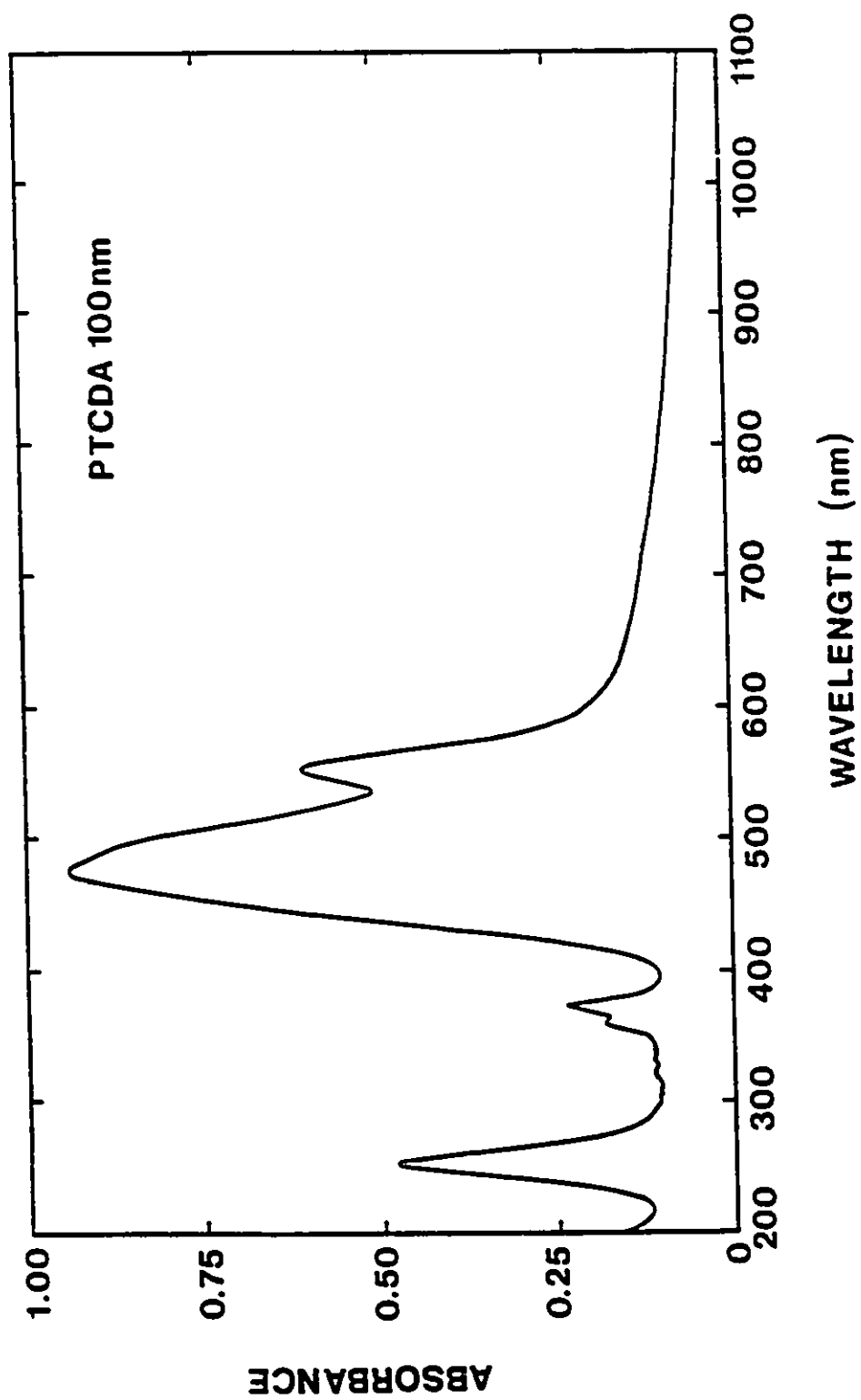


Figure 5-5: Electronic absorption spectrum of a 100 nm evaporated film of PTCDA on glass.

Figure 5-5



The FT-Raman and FT-SERS spectra for PTCDA followed closely the relative intensity patterns and frequency changes observed for SERRS and SERS in the visible region³². The FT-Raman spectrum of a 200 nm thin solid film of PTCDA is shown in Figure 5-7 along with an FT-SERS spectrum of a 3 nm film of PTCDA on a 20 nm Au island film. The frequencies observed in the FT-Raman spectrum of PTCDA include 1052 cm⁻¹, 1307 cm⁻¹, 1384 cm⁻¹, 1574 cm⁻¹ and 1592 cm⁻¹. In the same region, the frequencies observed in the FT-SERS are 1293 cm⁻¹, 1376 cm⁻¹, 1569 cm⁻¹ and 1578 cm⁻¹.

5.3.3 Comparison of Near-Infrared FT-SERS and Visible SERS for VOPc and PTCDA on gold films.

Vanadyl phthalocyanine has strong absorptions in the visible region as can be seen in Figure 5-4. However, there is a transparent window between 400 and 550 nm, and excitation with the 514.5 nm laser line was considered to give SERS, while excitation with the 647.1 nm line gave surface-enhanced resonant Raman scattering (SERRS). Comparing the SERS spectra obtained on Ag-coated Sn spheres⁴⁵ with the FT-SERS results may help to understand the influence of metal-molecule interaction and/or molecular orientation on the observed frequencies and relative intensity patterns. The symmetries of the fundamental isoindole stretching vibrations of VOPc have been studied using polarized Raman spectroscopy of submicron thin films on smooth gold surfaces⁴⁴. In general, there is good agreement between the two spectra, and the most intense Raman frequencies observed in SERS at 1521, 1338, 1001, 836, 678, 590 and 484 cm⁻¹ are also intense in the FT-SERS spectrum shown in Figure 5-6. It can be concluded that both spectra correspond to molecular species physisorbed onto the Ag and Au surfaces, respectively. The FT-Raman and visible RS are similar in one other important behavior. The thick films (bulk) of

Figure 5-6: (a) FT-Raman spectrum of 200 nm film of VOPc and (b) FT-SERS of a 3 nm film of VOPc on 20 nm Au island film.

Figure 5-6

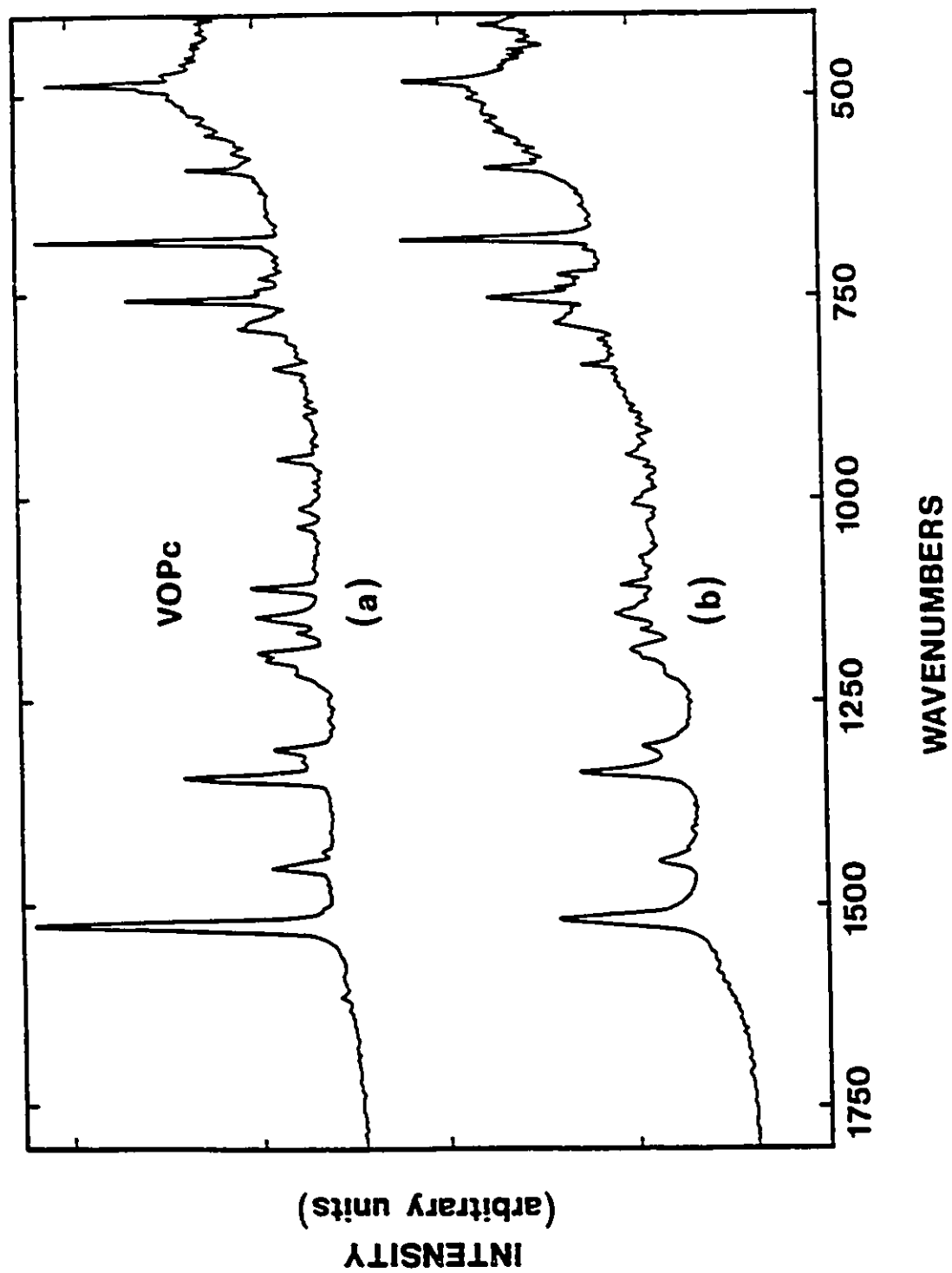
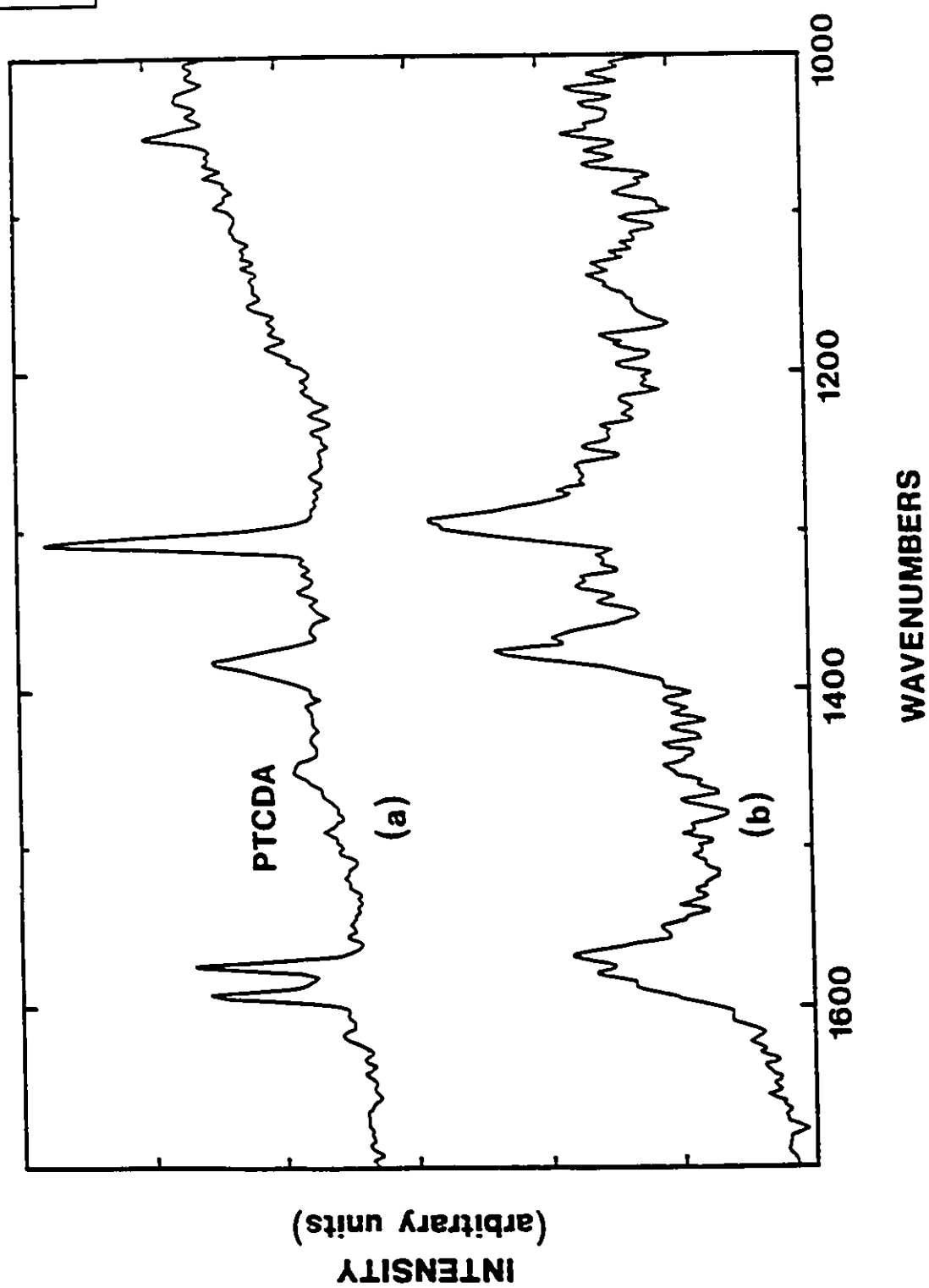


Figure 5-7: (a) FT-Raman spectrum of 200 nm PTCDA and (b) FT-SERS of 3 nm film of PTCDA on a 20 nm Au island film.

Figure 5-7



VOPc show a strong band at 1343 cm^{-1} in both the FT-Raman and visible Raman scattering (RS). However, the SS spectrum⁴⁶ (s-polarized light incident and s-polarized light collected) of the visible RS of a VOPc film showed a very intense band at 1337 cm^{-1} , which was the only one observed in SERS in this wavenumber region. It was assumed⁴⁴ that the doublet ($1343\text{-}1337\text{ cm}^{-1}$) was due to correlation field splitting. Identical results are obtained in the FT-Raman experiments: a band at 1343 cm^{-1} is observed in bulk with a side band at 1338 cm^{-1} , but the FT-SERS shows only one band at 1338 cm^{-1} .

The SERS of PTCDA in the visible region was shown to be different from the Raman spectrum of a solid sample, which was similar to both the corresponding resonant Raman spectrum (RRS) and SERRS³². For example, a doublet was observed in the RRS of the thin solid film at 1574 and 1592 cm^{-1} , which was also seen in the RS and SERRS, and was seen as well in the FT-Raman spectrum. Indeed, the RRS and SERRS (488 nm excitation) and the spontaneous RS obtained with the 1064.1 nm line are similar not only in frequency values but also in relative intensities. In the PTCDA SERS report³², it was shown that the 1574 cm^{-1} line was preferentially enhanced in the SERS spectrum excited with the 647.1 nm laser line on Ag-coated Sn spheres, while both frequencies were seen in the SERRS spectrum (488 nm excitation on Ag-coated Sn spheres). The FT-SERS results are consistent with previous findings, and of the doublet (1574 and 1592 cm^{-1}) observed in the FT-Raman spectrum shown in Figure 5-7, only the 1574 cm^{-1} band is preferentially enhanced in the FT-SERS. The preferentially enhanced band at 1574 cm^{-1} is, in turn, split into a doublet at 1569 and 1578 cm^{-1} . Also in agreement with the visible RS and SERS is the shift of the band centered at 1307 cm^{-1} in the FT-Raman spectrum of the thin solid film to 1293 cm^{-1} in the FT-SERS. In summary, FT-SERS spectra observed on gold

for both molecular systems are consistent with the previous observations of SERS in the visible spectral region, and unique intensity patterns found in the SERS spectra are also observed in the FT-SERS.

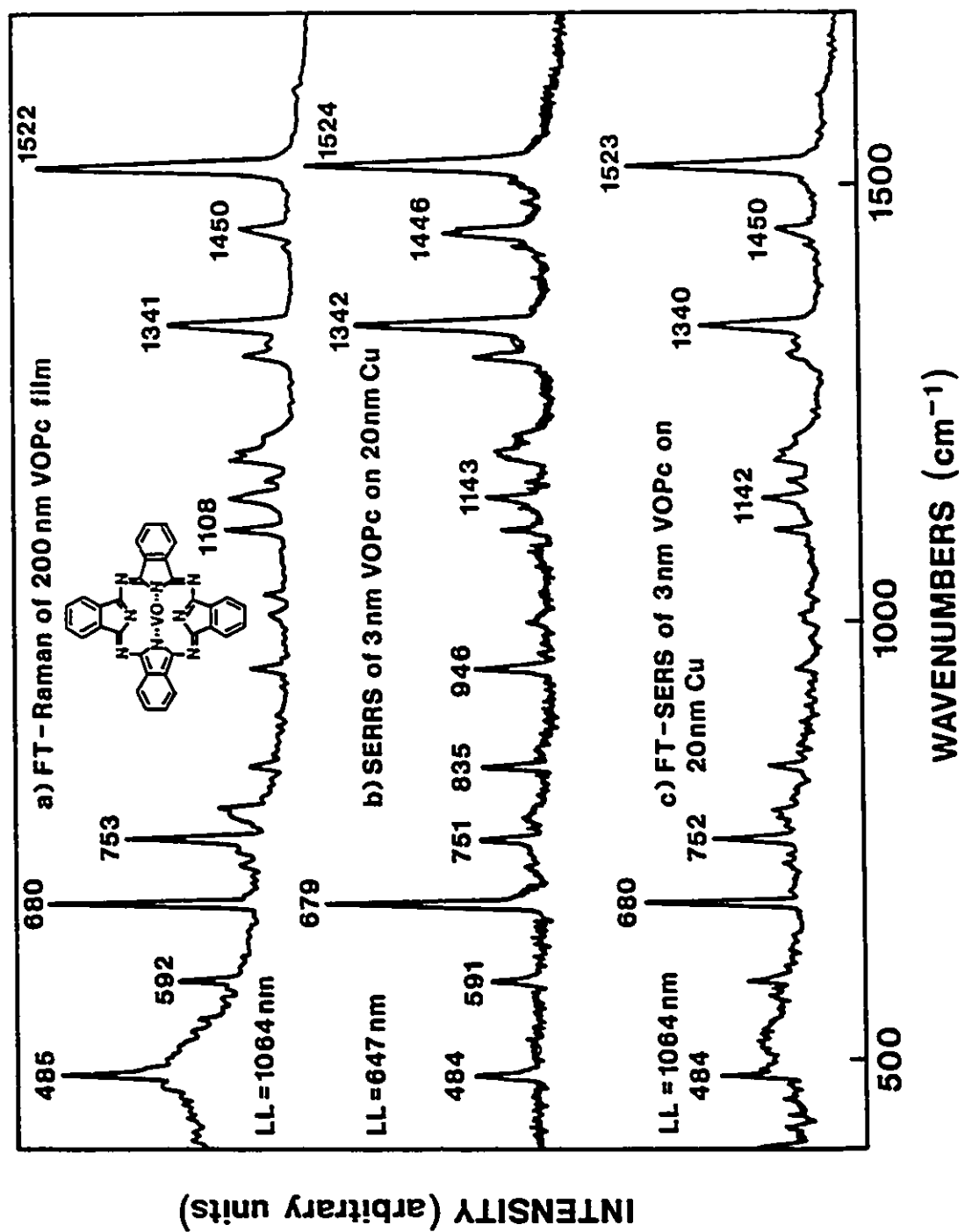
5.3.4 FT-SERS of Thin Vacuum Evaporated VOPc Films on Cu Islands and Semiconductors

FT-SERS was obtained for a 3 nm vacuum evaporated film of vanadyl phthalocyanine on a 20 nm copper island film, the Raman spectra are shown in Figure 5-8. Vanadyl phthalocyanine does not absorb significantly at the 1064.1 nm Nd/YAG laser line but does absorb strongly at the 647.1 nm line of the Kr⁺ laser. The 20 nm copper island film prepared at 200°C displayed a broad absorption spectrum with some absorption at both 647.1 and 1064.1 nm. The spontaneous Raman scattering of a 200 nm thick VOPc film evaporated at room temperature onto glass is included in Figure 5-8 (a) as a reference. Figure 5-8 (b) shows surface-enhanced resonance Raman scattering of a VOPc film on a 20 nm copper island film. Electromagnetic SERS is combined with the resonance Raman effect. Figure 8-5 (c) displays the FT-SERS spectrum of a 3 nm VOPc film on copper islands. The frequency values are practically the same for the FT-Raman of thick VOPc (top) and the FT-SERS (bottom). This indicates that the VOPc is physisorbed rather than chemisorbed onto the metal surface.

Table 5-1 gives the assignments for the spontaneous Raman scattering of VOPc, SERRS of VOPc on Cu, and FT-SERS of VOPc on Cu. The isoindole and benzene radial deformations occur at 484 cm⁻¹ and 591 cm⁻¹ respectively. A macrocycle can be defined by the sixteen inner alternating carbon and nitrogen atoms. Macrocycle breathing and stretching modes are observed in the 650 cm⁻¹ to 1000 cm⁻¹ region while carbon-hydrogen bending modes are

Figure 5-8: (a) FT-Raman spectrum of 200 nm VOPc on glass. Laser line 1064.1 nm. (b) SERRS spectrum of 3 nm VOPc on 20 nm Cu. Laser line 647.1 nm. (c) FT-SERS spectrum of 3 nm VOPc on 20 nm Cu. Laser line 1064.1 nm.

Figure 5-8



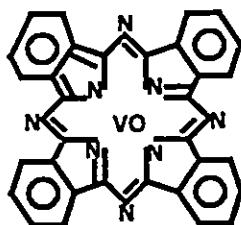
seen from 1000 cm^{-1} to 1300 cm^{-1} . The resonance Raman scattering of phthalocyanine has contributions mainly from the Herzberg-Teller term. Excitation at 647.1 nm enhances both totally and non-totally symmetric vibrations of VOPc. The SERRS spectrum in Figure 5-8 (b) has contributions from both the resonance Raman effect and surface-enhanced scattering.

SERRS and FT-SERS for 3 nm VOPc on copper islands are remarkably similar in relative intensities as can be seen in Figure 5-8 (b) & (c). The observation is simply a consequence of comparable relative intensities found in the correlation of the resonant Raman spectrum (laser frequency in resonance with the Q-band of the VOPc) with the spontaneous FT-Raman spectrum. The SERS spectrum of this particular molecule seems to be reduced to the original spectrum (RRS or FT-Raman) times the enhancement factor, a textbook case of physisorption. FT-SERS was not observed for a 3 nm thick film of VOPc on either GaAs or $\text{Ga}_{0.7}\text{Al}_{0.3}\text{As}$ semiconductor substrates.

5.3.5 FT-SERS of Single LB Monolayers on Copper and Gold Island Films.

FT-SERS is reported here for the first time for a single Langmuir-Blodgett monolayer on vacuum evaporated metal island films. Figure 5-9 shows the FT-SERS spectrum and SERRS spectrum of a single LB monolayer of copper tertiary-butyl-phthalocyanine (CuTTPc) on a 20 nm gold film. Molecular modeling by Hahn et al. suggested that the bulky tertiary-butyl groups of CuTTPc are interleaved with neighboring molecules on water and transmission electron micrographs of CuTTPc on supported grids indicated the molecules form columns in the plane of the film with 1.9 nm between columns and an in-

Table 5-1: Raman Frequencies and Intensities for vacuum evaporated VOPc and VOPc on Cu



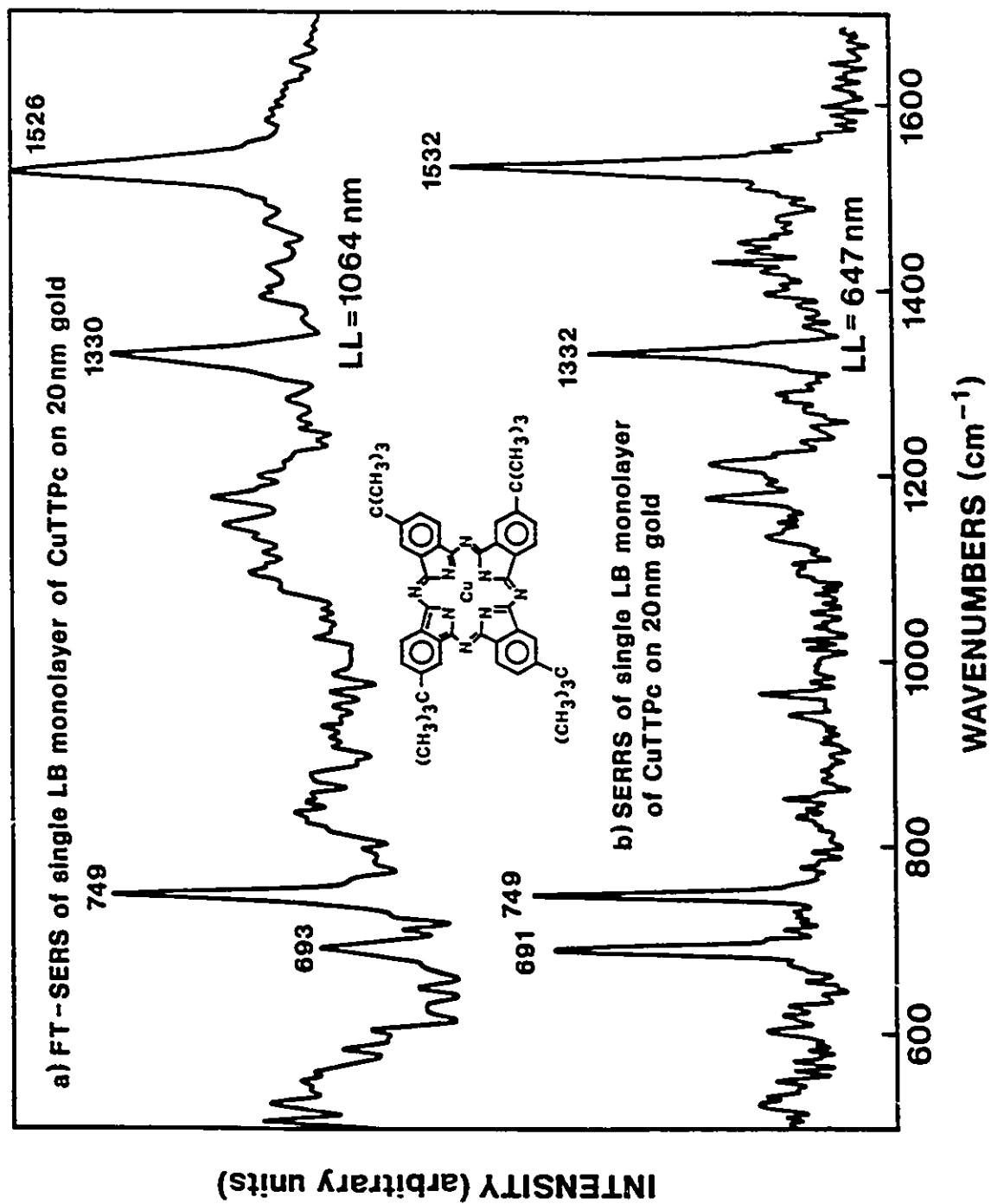
200 nm VOPc LL=1064 nm (RS) Wavenumbers (relative intensity)	3 nm VOPc on 20 nm Cu (200°C) LL=647nm (SERRS) Wavenumbers (relative intensity)	3 nm VOPc on 20 nm Cu (200°C) LL=1064 nm (FT-SERS) Wavenumbers (relative intensity)	Assignments
485 cm ⁻¹ (44)	484 cm ⁻¹ (26)	484 cm ⁻¹ (36)	isoindole ring def.
592 cm ⁻¹ (24)	591 cm ⁻¹ (19)	591 cm ⁻¹ (18)	benzene radial
680 cm ⁻¹ (79)	679 cm ⁻¹ (91)	680 cm ⁻¹ (68)	macrocycle breathing
753 cm ⁻¹ (50)	751 cm ⁻¹ (22)	752 cm ⁻¹ (38)	benzene (ν ₁)
787 cm ⁻¹ (18)	-----	787 cm ⁻¹ (13)	macrocycle stretching
836 cm ⁻¹ (10)	835 cm ⁻¹ (29)	836 cm ⁻¹ (18)	macrocycle stretching
947 cm ⁻¹ (15)	946 cm ⁻¹ (29)	947 cm ⁻¹ (11)	macrocycle stretching
1008 cm ⁻¹ (7)	1007 cm ⁻¹ (18)	1010 cm ⁻¹ (9)	C-H bend
1032 cm ⁻¹ (7)	-----	-----	C-H bend
1107 cm ⁻¹ (22)	1107 cm ⁻¹ (18)	1106 cm ⁻¹ (16)	C-H bend
1143 cm ⁻¹ (19)	1143 cm ⁻¹ (26)	1142 cm ⁻¹ (21)	pyrrole ring breathing
1162 cm ⁻¹ (6)	-----	1162 cm ⁻¹ (9)	C-H bend
1187 cm ⁻¹ (22) ----- -----	----- 1196 cm ⁻¹ (20) -----	1186 cm ⁻¹ (18) 1194 cm ⁻¹ sh. 1210 cm ⁻¹ sh.	C-H bend
1306 cm ⁻¹ (15) -----	1304 cm ⁻¹ (27) -----	1306 cm ⁻¹ sh. 1321 cm ⁻¹ sh.	C-H bend
1341 cm ⁻¹ (44)	1342 cm ⁻¹ (75)	1340 cm ⁻¹ (59)	pyrrole ring stretch
1450 cm ⁻¹ (18)	1446 cm ⁻¹ (41)	1450 cm ⁻¹ (20)	isoindole ring stretch
1522 cm ⁻¹ (100)	1524 cm ⁻¹ (100)	1523 cm ⁻¹ (100)	C-N pyrrole stretch

stack distance of 0.33 nm²¹. Excitation at 647.1 nm is in resonance with an electronic absorption of the CuTTPc molecule and gives surface-enhanced resonance Raman scattering on the gold island surface. The 1064.1 nm Nd/YAG laser line is in resonance with the plasmons in the gold film only and gives rise to FT-SERS. Relative intensities in the region of the macrocycle breathing vibration (691 cm⁻¹) are different due to the specific intensity enhancement of the chromophore vibrations by the resonance Raman effect. The band at 1332 cm⁻¹ in SERRS is centered at 1330 cm⁻¹ in FT-SERS and similarly the 1532 cm⁻¹ band in SERRS is measured at 1526 cm⁻¹ in FT-SERS. The latter differences could be due to the contribution of two fundamentals to the envelope of the observed Raman bands in the FT-SERS. One of the components could be selectively enhanced by the resonance Raman effect. The band near 1330 cm⁻¹ is a pyrrole ring stretch while C-N pyrrole stretching and C β -C β pyrrole stretching account for the bands at 1526 cm⁻¹ and 1532 cm⁻¹.

The FT-SERS spectrum of a mixed monolayer (1:10) of the asymmetrically substituted dipthalocyanine P α LuP α t and arachidic acid on a 20 nm film are presented in Figure 5-10 (a). Surface-enhanced resonance Raman results for the mixed monolayer on copper and gold island films appear in Figures 5-10 (b) and 5-10 (c). The purpose of the arachidic acid was to act as a lubricant on the water and improve the transfer to the substrate. A 20 nm gold island film absorbs light more strongly at the 647.1 nm laser line than the 20 nm copper island film. The observed frequencies for the mixed LB monolayer on gold and copper are similar. The FT-SERS signals were very weak since the P α LuP α t is diluted in arachidic acid. Considering the FT-SERS results first, the 560 cm⁻¹, 760 cm⁻¹ and 913 cm⁻¹ peaks can be assigned respectively to an isoindole deformation, and two macrocycle stretching modes. It was interesting to note

Figure 5-9: (a) FT-Raman spectrum of a single LB monolayer of CuTTPc on 20 nm Au. Laser line 1064.1 nm. (b) SERRS spectrum of a single LB monolayer of CuTTPc on 20 nm Au. Laser line 647.1 nm.

Figure S-9



that there were no Raman bands from the arachidic acid. The most intense band in the SERRS spectra at 681 cm^{-1} arises from macrocycle breathing and macrocycle stretches appear at 744 cm^{-1} and 819 cm^{-1} . In the low frequency region, an isoindole deformation was observed at 479 cm^{-1} with the benzene radial deformation at 577 cm^{-1} . The PCLuPct is physisorbed because known frequencies of diphthalocyanines were observed and not shifted as expected for chemisorption. There is a specific intensity enhancement of chromophore vibrations by the resonant Raman effect in Figures 5-10 (b) and 5-10 (c) which explains the changes in relative intensities between FT-SERS and SERRS.

The FT-SERS and SERRS spectra of a single LB monolayer of *N*-pentyl-*N'*-ethyl-3,4:9,10-perylenetetracarboxylic diimide (PPTCDE) on a 20 nm gold island film are shown in Figure 5-11. The PPTCDE does not have any absorbance in the near-IR at 1064.1 nm while the gold island film absorbs in this region allowing surface-enhanced Raman scattering. The 514.5 nm laser line is in resonance with an electronic absorption in the perylene and the 20 nm gold island film also absorbs at this wavelength producing SERRS. An upper limit of (ca. 10^3) for the enhancement of a resonance Raman signal has been suggested⁴⁷. Earlier work⁴⁸ on the perylene chromophore reported a SERRS enhancement factor of at least 10^4 . The resonance Raman in tetracarboxylic derivatives is due mainly to Franck-Condon scattering and overtones have been observed⁴⁸.

The a_{1g} modes for perylene have been reported⁴⁹ at 550, 1104, 1298, 1369, 1380, 1574 and 1581 cm^{-1} . The FT-SERS frequencies of PPTCDE on gold were 541, 1073, 1292, 1375, 1450 and 1576 cm^{-1} . The 541 cm^{-1} and 1073 cm^{-1} bands correspond to a benzene ring deformation and benzene breathing

Figure 5-10: A mixed monolayer of 1:10 PCLuPct / arachidic acid. (a) FT-Raman spectrum on 20 nm Au. Laser line 1064.1 nm. (b) SERRS spectrum on 20 nm Au. Laser line 647.1 nm. (c) SERRS spectrum on 20 nm Cu. Laser line 647.1 nm.

Figure 5-10

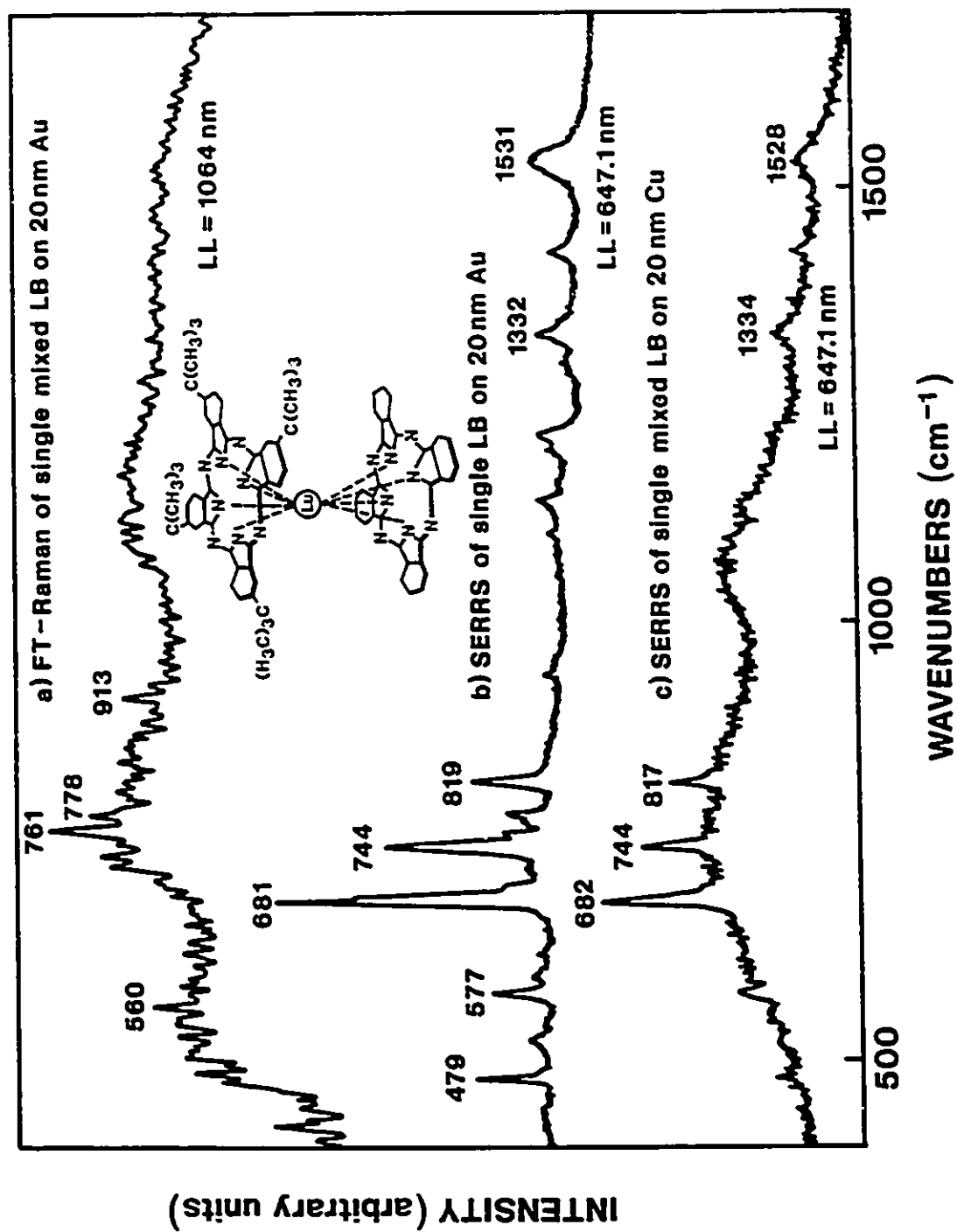
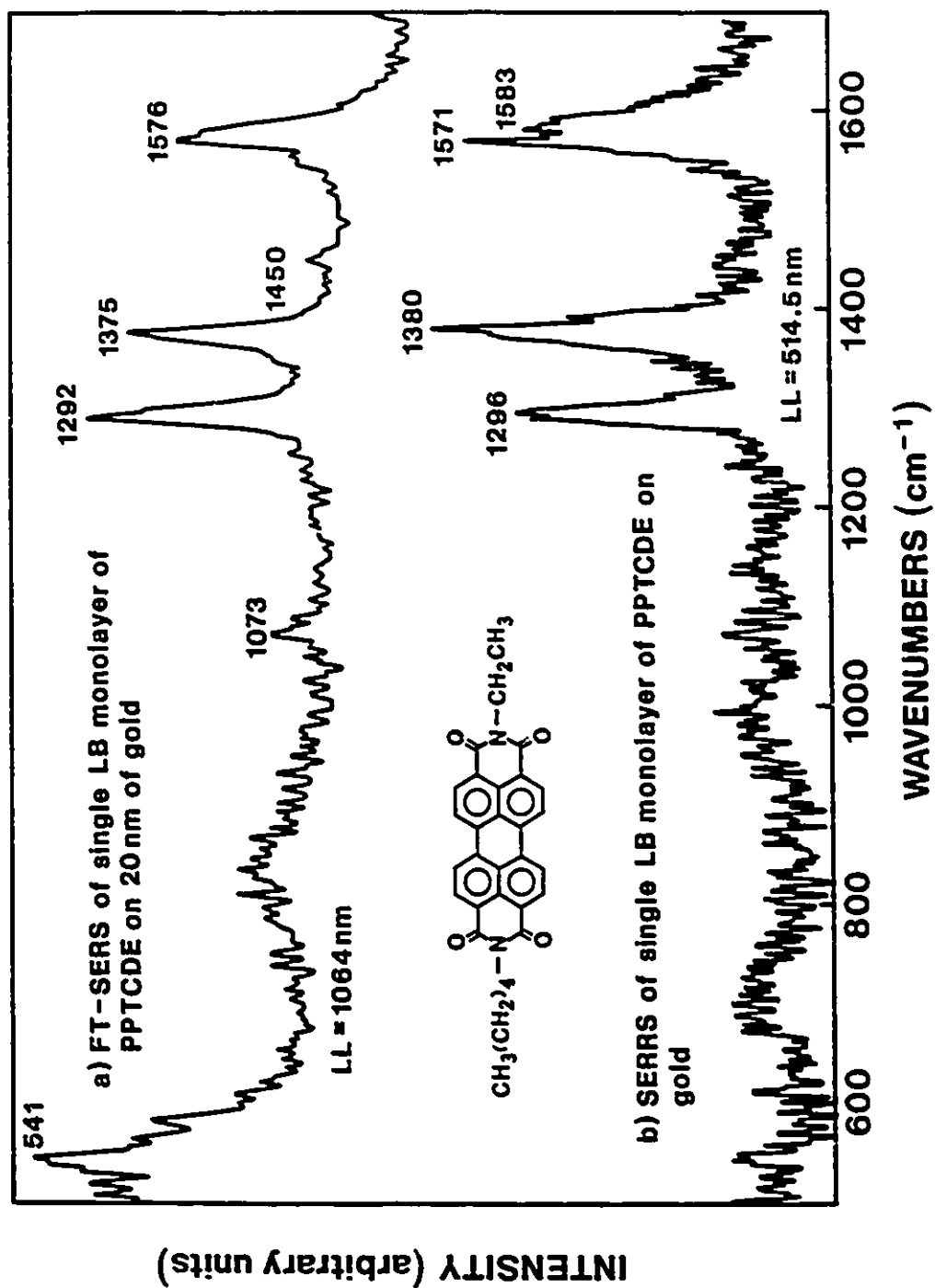


Figure 5-11: (a) FT-SERS spectrum of a single LB monolayer of PPTCDE on 20 nm Au. Laser line 1064.1 nm. (b) SERRS spectrum of a single LB monolayer of PPTCDE on 20 nm Au. Laser line 514.5 nm.



modes respectively. Characteristic group frequencies for the perylene moiety include 1375 cm^{-1} and 1576 cm^{-1} vibrations which involve stretches of the naphthalene group⁴⁹. There are two different naphthalene groups in PPTCDE due to asymmetric alkyl substitution and shoulders appear on the sides of these naphthalene bands. The peak at 1292 cm^{-1} is also a vibration of the parent perylene moiety⁵⁰. The PPTCDE LB monolayer is physisorbed on the gold island film since frequency shifts remain unchanged from PPTCDE alone. In general, a weak continuum inelastic scattering background appeared towards higher wavenumbers for all films which showed FT-SERS which is due to the metal film. The resonance Raman contribution to the SERRS scattering for PPTCDE selectively enhances vibrations of different symmetry type than those seen in the FT-SERS, differences seen in Figure 5-11.

5.4 CONCLUSIONS

FT-SERS on copper and gold island films is reported for the first time. Observed enhancement factors are below 10^3 , an upper limit that would be predicted from the electromagnetic model for metal films with a high density of large metal islands on a glass surface. Recorded FT-SERS spectral frequencies and relative intensities for both VOPc and PTCDA are in agreement with previous SERS findings and support a model of physisorbed molecules on the Au surface. FT-SERS was also observed for a 3 nm vacuum evaporated film of VOPc on a 20 nm copper island film.

FT-SERS is reported for the first time for single LB monolayers on metal island films. The CuTTPc, PCLuPct, and PPTCDE LB monolayers were physisorbed to the metals and the electromagnetic mechanism caused the surface-enhanced Raman scattering. The resonance Raman effect has been shown to selectively enhance chromophore vibrations in SERRS spectra. Gold island films absorb more in the red than copper island films. This results in a greater efficiency of surface plasmon generation which in turn results in greater SERRS enhancement. FT-SERS is a viable technique for obtaining more intense signals for the study Langmuir-Blodgett films or thin vacuum evaporated films in the near-IR.

Chapter 5 References

1. Chase, D. B. *ICORS 1990 (International Conference on Raman Spectroscopy)*; Durig, J. R., Sullivan, J. F., Eds.; John Wiley & Sons: Chichester, 1990, p 11.
2. *Spectrochimica Acta* 1990, 46A. Special edition on FT-Raman spectroscopy, P. J. Hendra, Ed.
3. Jennings, C. A.; Kovacs, G. J.; Aroca, R. *J. Phys. Chem.* 1992, 96, 1340.
4. Jennings, C. A.; Kovacs, G. J.; Aroca, R. *Langmuir* 1993, 9(8), 2151.
5. *Surface Enhanced Raman Scattering*; Furtak, T. E., Chang, R. K., Eds.; Plenum: New York, 1982.
6. Cotton, T. M. In *Spectroscopy of Surfaces*; Clark, R. J. H., Hester, R. E., Eds.; J. Wiley & Sons, Chichester, 1988; vol. 16, p. 91.
7. Chang, R. K.; Laube, B. L. *CRC Crit. Rev. Solid State Mater. Sci.* 1984, 12.
8. Moskovits, M. *Rev. Mod. Phys.* 1985, 57, 783.
9. Angel, S. M.; Katz, L. F.; Archibald, D. D.; Lin, L. T.; Honigs, D. E. *Appl. Spectrosc.* 1988, 42, 1327.
10. Angel, S. M.; Archibald, D. D. *Appl. Spectrosc.* 1989, 43(6), 1097.
11. Fleischmann, M.; Sockalingum, D.; Musiani, M. *Spectrochim. Acta* 1990, 46A, 285.
12. Crookell, A.; Fleischmann, M.; Hanniet, M.; Hendra, P. *J. Chem. Phys. Lett.* 1988, 149, 123.
13. Chase, D. B.; Parkinson, B. A. *Appl. Spectrosc.* 1988, 42, 1186.
14. Lipscomb, L. A.; Nie, S.; Feng, S.; Yu, N. *Chem. Phys. Lett.* 1990, 170(5,6), 457.
15. Angel, S. M.; Katz, L. F.; Archibald, D. D.; Honigs, E. E. *Appl. Spectrosc.* 1989, 43(3), 367.
16. Potts, J. E.; Merlin, R.; Partin, D. L. *Phys. Rev. B.* 1983, 27(6), 3095.
17. Hayashi, S.; Koh, R.; Ichiyama, Y.; Yamamoto, K. *Phys. Rev. Lett.* 1988, 60(11), 1085.
18. Loo, B. H. J. *Electroanal Chem.* 1982, 136, 209.
19. Ueba, H. *Surf. Sci.* 1983, 133, L432.
20. Kovacs, G. J.; Vincett, P. S.; Sharp, J. H. *Can. J. Phys.* 1985, 63, 346.

21. Hann, R. A.; Gupta, S. K.; Fryer, J. R.; Eyres, B. L. *Thin Solid Films* 1985, 134, 35.
22. Battisti, D.; Aroca, R. *J. Am. Chem. Soc.* 1992, 114, 1203.
23. Riou, M. T.; Auregan, M.; Clarisse, C. *J. Electroanal. Chem.* 1985, 187, 349.
24. Moskalev, P. N.; Kirin, I. S. *Russ. J. Phys. Chem.* 1972, 46(7), 1019.
25. M'Sadak, M.; Roncali, J.; Garnier, F. *J. Electroanal. Chem.* 1985, 189, 99.
26. Aroca, R.; Clavijo, R. E.; Jennings, C. A.; Kovacs, G. J.; Duff, J. M.; Loutfy, R. O. *Spectrochim. Acta* 1989, 45A(9), 1957.
27. Souto, J.; Aroca, R.; DeSaja, J. A. *J. Raman Spectrosc.* 1991, 22, 349.
28. Clavijo, R. E.; Battisti, D.; Aroca, R.; Kovacs, G. J.; Jennings, C. A. *Langmuir* 1992, 8, 113.
29. Souto, J.; Aroca, R.; DeSaja, J. A. *J. Raman Spectrosc.* 1991, 22, 787.
30. Akers, K.; Aroca, R.; Hor, A.; Loutfy, R. O. *J. Phys. Chem.* 1987, 91(11), 2955.
31. Akers, K.; Aroca, R.; Hor, A. M.; Loutfy, R. O. *Spectrochim. Acta* 1988, 44A, 1129.
32. Guhathakurta-Ghosh, U.; Aroca, R. *J. Phys. Chem.* 1989, 93, 6125.
33. Aroca, R.; Guhathakurta-Ghosh, U.; Loutfy, R. O.; Nagao, Y. *Spectrochim. Acta* 1990, 46A, 717.
34. Johnson, E.; Aroca, R.; Nagao, Y. *J. Phys. Chem.* 1991, 95, 8840.
35. Aroca, R.; Johnson, E. *Raman and Luminescence Spectroscopies in Technology II*; SPIE: Bellingham, WA, 1990; Vol. 1336, p 291.
36. Johnson, E.; Aroca, R. *Can. J. Chem.* 1991, 69, 1728.
37. Nagao, Y.; Misono, T. *Dyes Pigm.* 1984, 5, 171.
38. Fromherz, P. *Rev. Sci. Instrum.* 1975, 46, 1380.
39. Tomilova, L. G.; Chernykh, E. V.; Gavrilov, V. I.; Shelepin, I. V.; Derkacheva, V. M.; Luk'yanets, E. A. *Zh. Obshch. Khim.* 1982, 52, 2606.
40. Mrozek, I.; Borneman, T.; Otto, A. *Surf. Sci.* 1988, 204, 358.
41. Zeman, E. J.; Shatz, G. C. *J. Phys. Chem.* 1987, 91, 634.
42. Aroca, R.; Martin, F. *J. Raman Spectrosc.* 1985, 16, 156.
43. Wolkaun, A. *Mol. Phys.* 1985, 56, 1.

44. Murray, C. A.; Allara, D. L. *J. Chem. Phys.* **1982**, *76*, 1290.
45. Battisti, D.; Aroca, R.; Loutfy, R. O. *Chem. Mater.* **1989**, *1*, 124.
46. Aroca, R.; Battisti, D.; Kovacs, G. J.; Loutfy, R. O. *J. Electrochem. Soc.* **1989**, *136*, 2902.
47. Weitz, D. A.; Garnoff, S.; Gersten, J. I.; Nitzen, A. *J. Electron Spectrosc. Relat. Phenom.* **1983**, *29*, 1963.
48. Aroca, R.; Clavijo, R. E. *Spectrochim. Acta* **1991**, *47A* (2), 271.
49. Kovner, M. A.; Terkhov, A. A.; Babkov, L. M. *Opt. Spectrosc.* **1972**, *33*, 38.
50. Hochstrasser, R. M.; Nyi, C. A. *J. Chem. Phys.* **1980**, *72*, 2591.

CHAPTER 6: SPECTROSCOPY AND ATOMIC FORCE MICROSCOPY OF LANGMUIR-BLODGETT MONOLAYERS

6.1. INTRODUCTION

Thin solid films of perylenes and phthalocyanines have been prepared using the Langmuir-Blodgett (LB) technique. The orientation of LB monolayers of a series of perylenes on metal surfaces has been determined using reflection-absorption infrared spectroscopy. The atomic force microscopy (AFM) instrument was used to study LB monolayers on atomically flat substrates such as mica and silicon wafers. The observed thickness of a monolayer of *N*-hexyl-*N'*-ethyl-3,4:9,10-perylenetetracarboxylic diimide (HPTCDE) was 1.83 nm by AFM which agrees with the orientation calculated from the reflection-absorption IR measurements. The importance of AFM as an analytical method for characterization of LB film structures and defects is demonstrated. In addition to HPTCDE, AFM results are also included for LB monolayers of *N*-hexyl-3,4:9,10-perylenetetracarboxylic monoimide (HPTCO); 1,4,8,11,15,18,22,25-octabutoxy-29H,31H-phthalocyanine ((BuO)₈H₂Pc) and tetra-*tertiary*-butyl metal-free phthalocyanine, (t-bu)₄H₂Pc.

Thin solid films which differ from bulk material, can be prepared by the Langmuir-Blodgett technique^{1,2}. A single LB monolayer has two interfaces which affect its structure, the first being the substrate/monolayer interface and the second is the monolayer/air interface. The orientation of the monolayer on the substrate is influenced by whether the substrate is hydrophobic or hydrophilic and the manner in which transfer to the substrate is completed. The monolayer is either physisorbed or chemisorbed to the substrate and

intermolecular forces between the molecules in the monolayer play an important role in determining structure. The most thermodynamically stable form of a monolayer may not even be a uniform film.

Mixed monolayers consist of at least two components within a given layer. Segregation or formation of domains could be observed rather than a homogeneous mixing of materials. It is possible to build up a number of successive LB monolayers giving highly organized structures in three dimensions. Strong intermolecular forces between adjacent monolayers is a stabilizing feature and leads to rearrangement after transfer in stearic acid LB films^{3,4}. Two techniques to experimentally explore LB film structure are infrared spectroscopy and atomic force microscopy (AFM).

Reflection-absorption infrared spectroscopy (RAIRS) using different polarizations of light provides information on the orientation of molecules in an LB monolayer. In fact, molecular orientation in Langmuir-Blodgett multilayers can be determined from the combined infrared spectral data obtained in a transmission geometry and in a reflection-absorption geometry. The approach has been illustrated by Umemura *et al.*^{5a} using LB monolayers of cadmium stearate. The quantity of interest that can be evaluated with this method is the tilt angle formed between the direction of a dynamic dipole moment and the normal to the surface of the film. The information so obtained corresponds to an average molecular orientation of molecules on the surface.

If molecular resolution was possible with local probe methods such as AFM, specific molecular information in LB films, rather than data which is

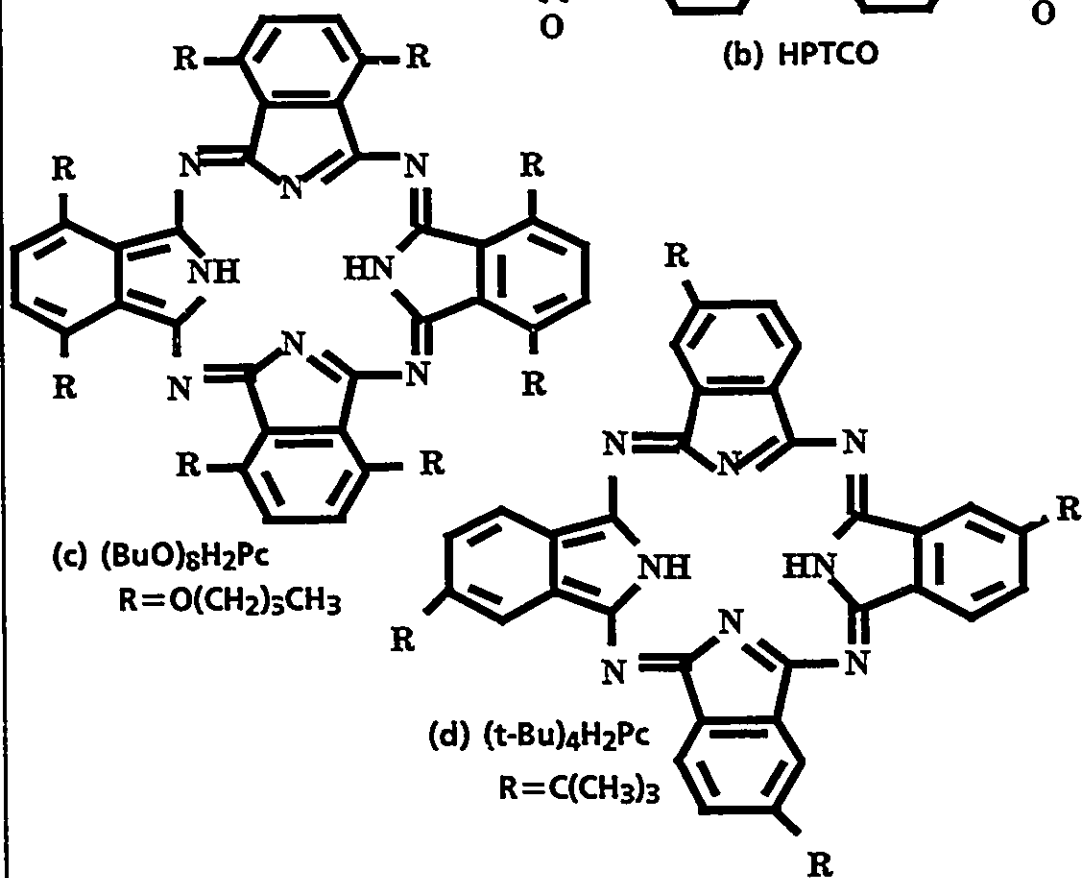
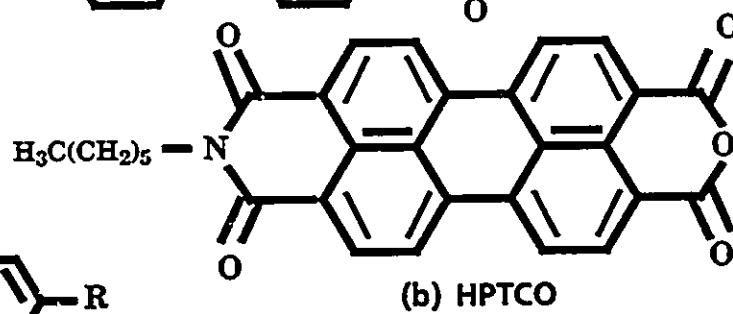
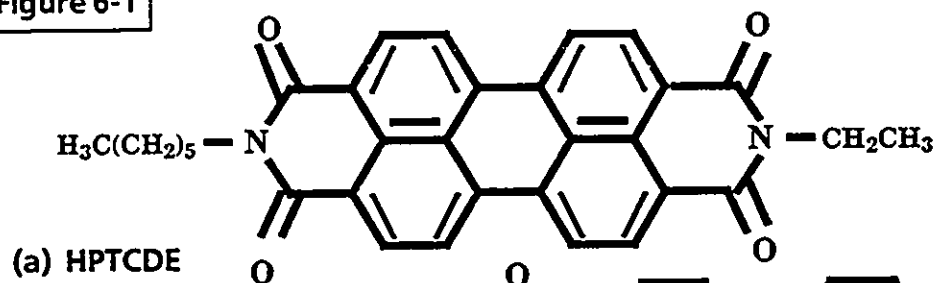
averaged over a large sample region as is the case with infrared spectroscopy, would be found. An AFM instrument can be used to study surface coverage, local defects such as pinholes, cracks, grain boundaries and heterogeneous structures in mixed LB films. Scanning tunneling microscopy (STM) typically requires that the sample under investigation be conductive while AFM can be applied to conductive and non-conductive materials. The force exerted by the tip of the AFM is on the order of 10^{-9} N, and is preferred for imaging thin organic films such as LB monolayers to minimize sample damage^{5b}. It is now known that the force on an organic monolayer can be reduced by imaging under water in a liquid cell⁶. The AFM also has advantages compared to electron microscopy because samples can be imaged directly. For scanning electron microscopy, a conductive overcoat is applied to non-conductive films or a replica is made. A problem with transmission electron microscopy is low contrast for a single LB monolayer and the need to transfer the monolayer to a microscope grid.

In this chapter, atomic force microscopy was used to characterize single LB monolayers of perylenes and phthalocyanine derivatives on mica and silicon wafers. The pigment structures appear in Figure 6-1.

There have been STM reports in the literature concerning vacuum evaporated phthalocyanine films⁷⁻¹⁰. Copper phthalocyanine was sublimed onto Cu(100) at room temperature and high resolution images were obtained for submonolayer coverages in an ultrahigh vacuum (UHV) STM system⁷. The CuPc molecules were flat on the substrate with two different molecular orientations. There was excellent agreement between the model of the charge

- Figure 6-1: Structures of Langmuir-Blodgett materials.
- (a) *N*-hexyl-*N'*-ethyl-3,4:9,10-perylenetetracarboxylic diimide (HPTCDE).
 - (b) *N*-hexyl-3,4:9,10-perylenetetracarboxylic monoimide (HPTCO).
 - (c) 1,4,8,11,15,18,22,25-octabutoxy-29H,31H-phthalocyanine ((BuO)₈H₂Pc).
 - (d) tetra-*tertiary*-butyl metal-free phthalocyanine, ((t-bu)₄H₂Pc).

Figure 6-1



densities of the highest occupied molecular orbitals (HOMOs) and the experimental data. Lead phthalocyanine films⁸ were vacuum evaporated onto a substrate of silicon wafer-SiO_x-Au composition with imaging in air. Different polymorphic forms of PbPc existed depending on the substrate temperature. Crystallites of 100 nm size were observed as well as 15 nm substructures but no molecular resolution was possible. Scanning tunneling microscopy results were presented for vanadyl naphthalocyanine⁹ (VONc) on highly oriented pyrolytic graphite (HOPG) and zinc naphthalocyanine (ZnNc) on MoS₂ substrate¹⁰, both imaged under ambient conditions. Molecular resolution was obtained of VONc and indicated a slipped stack orientation with the oxygen atom pointing towards the HOPG. There was a lattice matching of the VONc with the graphite substrate. In the case of ZnNc, the molecules were stacked and canted with respect to the MoS₂ substrate. In general, it is important to be able to determine the polymorphic form and orientation of phthalocyanine molecules on substrates because this influences the optical and electronic properties. The stacking and molecular orientation is temperature and substrate dependent.

Literature about AFM or STM of Langmuir-Blodgett monolayers of phthalocyanines has been scarce¹¹. A derivatized phthalocyanato-poly-siloxane was transferred to HOPG and gold by the LB technique, then imaged by STM. The polymer rods were parallel to the substrate and aligned in the dipping direction. However, fine structure was not observed and movement was apparent. Porphyrins are biologically important, large organic molecules with some similarities to phthalocyanines. Porphyrin-based molecules with pendant isocyano groups were reacted with epitaxially grown Au(111) on mica and imaged in air using STM¹². The porphyrin molecules were anchored by covalent bonding to the substrate.

The pigment 3,4:9,10-perylenetetracarboxylic dianhydride (PTCDA) was investigated on graphite using video STM¹³. The PTCDA was vacuum evaporated very slowly and formed a monolayer of flat molecules. Initially the PTCDA was coincident with the graphite but approached bulk α -PTCDA as the thickness was increased. High resolution images displayed a herringbone structure with two molecules per unit cell. Crystals of a perylene radical cation salt were prepared electrochemically and were imaged using STM and AFM¹⁴.

There have been numerous AFM and STM experiments performed on fatty acid LB films¹⁵⁻²⁰. STM images of behenic acid on HOPG showed two types of molecular arrangements parallel to the substrate¹⁶. The type II form, with a 6 nm periodicity indicated a rearrangement had taken place on the HOPG following LB deposition. Reorganization and crystallite formation was seen by AFM for LB films of cadmium arachidate on substrates that had been submerged under water for different times¹⁸. As the submersion time increased, bilayers peeled off the substrate and flipped onto existing covered areas to form patches and eventually crystallites. Two LB monolayers of barium arachidate were deposited onto a silanated silicon wafer so that alkyl chains were imaged by AFM¹⁵. Molecular resolution occurred at higher pH values where a large number of barium ions were incorporated into the bilayer giving additional stability to the film. Annealing of the LB films led to LB film dewetting and domains being formed that coexisted with bilayer. In summary, STM and AFM are tools to study the quality of LB films with respect to preparation method, pH, aging and annealing.

Monolayers can also be self-assembled rather than prepared by LB deposition. The types of molecules that form self-assembled monolayers

include trichlorosilanes on silicon²¹, alkanethiols on gold^{22,23} and decanol at the air/gold interface²⁴. The self-assembled monolayers were securely anchored to the gold making them stable to the forces exerted by the STM and AFM procedures.

Phthalocyanines (Pcs) and perylenes are commercially important with a wide range of applications. Both of these classes of materials can be used as photoreceptor pigments in copiers and laser printers for instance. Diphthalocyanines in particular exhibit electrochromic properties changing color when different voltages are applied²⁵⁻²⁷. Perylene and phthalocyanine derivatives are available which are water soluble and can be used as colorants in inks. Some phthalocyanines can reversibly bind gases such as nitrogen dioxide with applications as gas sensors²⁸⁻³².

6.2. EXPERIMENTAL

6.2.1. Preparation of Substrates and Langmuir-Blodgett Films.

A Fromherz³³ trough and dipper housed in a glove box on a terrazzo vibration-free table were used for film compression and transfer. Generally milli-Q water with one additional distillation was used without further treatment (pH ~ 6.3) at ambient temperature (~ 23°C). Two types of substrates, muscovite mica and silicon wafers were used for LB deposition and subsequent atomic force microscopy.

Muscovite mica (#4V-2 grade) was purchased from the Asheville-Schoonmaker Mica Company, Newport News, Virginia. Tweezers and a needle

were cleaned with Aldrich denatured HPLC grade ethyl alcohol (0.2 μm filtered). A sheet of mica was gripped using the tweezers and the needle was used to strip off an upper layer of contaminated mica. Successive layers of mica were peeled in a similar manner until a sheet was obtained with a large area showing a single visible color (thickness) on reflection in visible light. The mica had to be thick enough to support itself and typically gave a purple or yellow color on reflection. A smaller area was cut using a continuously heated platinum wire. The mica piece was clamped into the LB sample holder and immediately immersed in the Mega pure water subphase prior to the spreading of the monolayer.

Polished silicon test wafers of (111) orientation, p-boron doped and 3" diameter were purchased from Wafer Net, San Jose, CA. A diamond-tipped scribe was used to cut the wafers into 2.5 cm X 7.5 cm pieces suitable for our holder and LB trough. Any debris was rinsed off with the Mega pure water. The substrate was immediately immersed in the Mega pure water subphase prior to the spreading of the monolayer.

The two perylenes, *N*-hexyl-*N'*-ethyl-3,4:9,10-perylenetetracarboxylic diimide (HPTCDE) and *N*-hexyl-3,4:9,10-perylenetetracarboxylic monoimide (HPTCO) were synthesized and purified by Professor Nagao³⁴. For spreading onto the water surface, the HPTCDE was dissolved ($\sim 1 \times 10^{-4}$ M) in Burdick and Jackson high purity chloroform. Similarly, the HPTCO was dissolved ($\sim 3 \times 10^{-5}$ M) in B&D high purity chloroform. The compression speed of the trough was (1.9×10^{-3} nm²/molecule)/s for HPTCDE and (1.7×10^{-3} nm²/molecule)/s for HPTCO. Film transfer was carried out at 3.6 mm/min with a constant pressure of 15 mN/m by vertical substrate withdrawal for both HPTCDE and HPTCO on

mica and Si(111). Multilayers were transferred to IR transparent substrates (i.e., ZnS, Ge) and smooth silver films. The latter substrate was used for reflection-absorption infrared spectroscopy. Smooth silver films were prepared in high vacuum by evaporating 110 nm of silver onto Corning 7059 glass slides kept at 200°C. Silver thickness was monitored by an XTC Inficon quartz crystal oscillator. LB films were transferred at a constant pressure of 25 mN/m. The substrate was moved vertically through the gas-liquid interface at a rate of 3.6 mm/min. Up to 4 monolayers were transferred to smooth Ag substrates. Fifteen to thirty LB monolayers were transferred on withdrawal to the IR transmission substrates. Z-type deposition was used for all multilayer transfers with the water surface being cleaned each time before reinsertion of the substrate followed by spreading of a new film.

The 1,4,8,11,15,18,22,25-octabutoxy-29H,31H-phthalocyanine, ((BuO)₈-H₂Pc) was obtained from Aldrich and was used without further purification. For spreading onto the water surface, (BuO)₈H₂Pc was dissolved ($\sim 6 \times 10^{-4}$ M) in Baker Analyzed reagent 1,1,1-trichloroethane. The compression speed of the trough was (3.5×10^{-3} nm²/molecule)/s. Film transfer was carried out at 3.6 mm/min with a constant pressure of 15 mN/m by vertical substrate withdrawal.

The tetra-*tertiary*-butyl metal-free phthalocyanine, ((t-bu)₄H₂Pc) was synthesized in-house³⁵ from 4-t-butyl phthalonitrile in refluxing amyl alcohol, the reaction being promoted by sodium amylate. Purification was by acid pasting³⁶ and contains all of the possible isomers³⁷ which are related by the different relative positions of the t-butyl groups. For spreading onto the water surface, the (t-bu)₄H₂Pc was dissolved ($\sim 5 \times 10^{-4}$ M) in Eastman Kodak ACS spectro grade toluene. The compression speed of the trough was (1.1×10^{-3}

nm²/molecule)/s. Film transfer to the substrate was done at 3.6 mm/min at a constant pressure of 8 mN/m by vertical substrate withdrawal.

6.2.2. FTIR spectrometer and Reflection-Absorption Measurements.

A Bomem DA3 FTIR spectrometer with a MCT liquid nitrogen cooled detector was used to record IR spectra. A Spectra Tech spectral reflectance variable angle accessory was used to obtain RAIR spectra. An incidence angle of 75° to the surface normal was used in all cases. For data analysis, all files were imported to Spectra Calc™ software available from Galactic Industries Corp.

6.2.3. Park Scientific Atomic Force Microscope.

The AFM studies of HPTCDE on mica were carried out using a Park Scientific Instrument scanning force microscope with integrated Si₃N₄ tips. The force constant of the cantilever was determined from geometry and using Young's modulus³⁸. Scanning electron micrographs of the tips indicate that the Si₃N₄ tips have a radius of curvature on the order of 100 nm at the end of the tip. A high resolution image of the muscovite mica substrate was taken in the constant height mode. In the first attempt to image HPTCDE on mica, too large a force of 100 nN was applied which removed the HPTCDE from the substrate. A lower force of 10 nN was used to image a different region of the HPTCDE on mica. The micron sized images were taken in the constant force mode. All of the AFM images were collected in air. The height and distances were calibrated using a displacement meter. The scans of the mica substrate also provided a small-scale calibration since the dimensions of the mica unit cell are well known.

6.2.4. Digital Instruments Nanoscope III SPM.

All images were collected in the tapping mode with a 125 μm silicon probe. A "J" (125 μm) scanner was used in a Nanoscope III MultiMode AFM.

6.3. RESULTS AND DISCUSSION

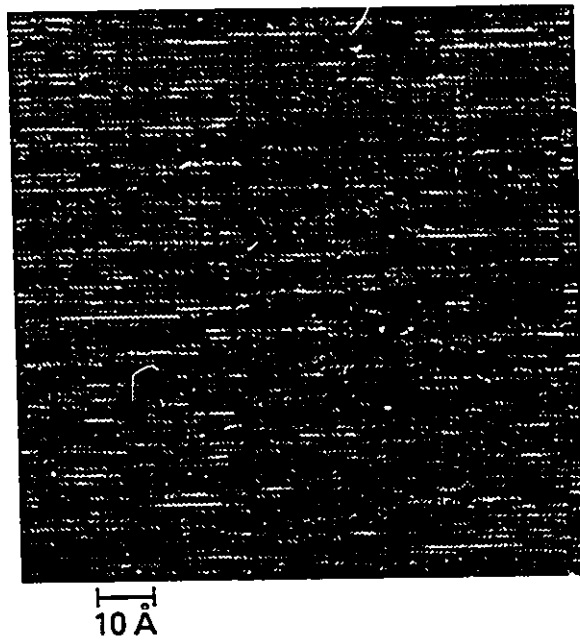
Figure 6-2 is a high resolution AFM image of bare muscovite mica $[\text{KAl}_2(\text{Si}_3\text{Al})\text{O}_{10}(\text{OH})_2]$ displaying atomic scale resolution. A Fourier transform of the image had the two largest peaks at $k_1 = 12.6 \text{ nm}^{-1}$ and $k_2 = 11.5 \text{ nm}^{-1}$ separated by an angle of 129 degrees. Using the k_1 and k_2 values, the calculated unit cell area was 0.21 nm^2 . From the literature^{39,40}, it is known that the surface of mica is a triangular lattice with a spacing of 0.52 nm between the vertices and a surface unit cell area of 0.23 nm^2 .

It was difficult to accurately determine the transfer ratio of HPTCDE to mica as the substrate piece was very small and irregular in shape. The transfer ratio is the area of material removed from the trough divided by the area of substrate used for the deposition. The HPTCDE had a transfer ratio of 1.0 to the Si(111) substrate using z-deposition. At the transfer pressure of 15 mNm^{-1} , the area per molecule was 0.48 nm^2 taken from the surface pressure-area isotherm. As shown in Figure 6-3, if too large a force is applied to the monolayer of HPTCDE on mica, the AFM tip can scrape away the film. One application of the AFM would be as a modifying tool to write features on a submicron scale. The AFM or STM could also be used for nanotechnology⁴¹ to build structures from the bottom up by manipulation and selective placement of atoms.

Figure 6-2: High resolution image of muscovite mica obtained on a Park Scientific AFM.

Figure 6-2

Mica surface



Another region of the LB monolayer of HPTCDE on mica was imaged with a smaller force of 10 nN and the large area image appears in Figure 6-4. Molecular resolution was not observed. Three different height levels were apparent as black, gray and white. The height difference between the black and gray regions was 1.83 ± 0.34 nm measured for seven cross-sections and between the gray and white features was 1.86 ± 0.28 nm using six cross-sections. The HPTCDE does not appear to be coating the mica uniformly. The black areas are the underlying mica substrate, the gray regions HPTCDE monolayer, and the white features are two layers of HPTCDE. The HPTCDE monolayer thickness of $1.83 \text{ nm} \pm 0.34 \text{ nm}$ is consistent with reflection-absorption infrared measurements. The molecular orientation in the LB film has been elucidated through infrared spectroscopy⁴². Using the absorbance ratio between the transmission and reflection-absorption infrared spectra, mean molecular tilt angles of the long and short axes of the chromophore in the LB layers have been determined.

The FTIR transmission and reflection-absorption spectra of HPTCDE are shown in Figure 6-5. HPTCDE dispersed in a KBr pellet corresponds to isotropic molecular orientation. The bands in the region around 1600 cm^{-1} are due to C=C stretching vibrations in the benzene rings. Peaks at 1656 cm^{-1} and 1659 cm^{-1} have been assigned to anti-symmetric carbonyl stretching and symmetric carbonyl stretching respectively⁴². Anti-symmetric carbonyl stretching causes changes in the dynamic dipole moment along the short axis of HPTCDE while symmetric carbonyl stretching changes the dynamic dipole moment along the long axis of HPTCDE. The tilt angle ϕ is defined as the angle between the dynamic dipole moment and the normal to the substrate surface. The tilt angle can be determined using equation 6.142-44.

Figure 6-3: HPTCDE Langmuir-Blodgett monolayer scraped from the mica substrate when the applied force is too large. Park Scientific AFM image.

Figure 6-3

HPTCDE perylene on mica

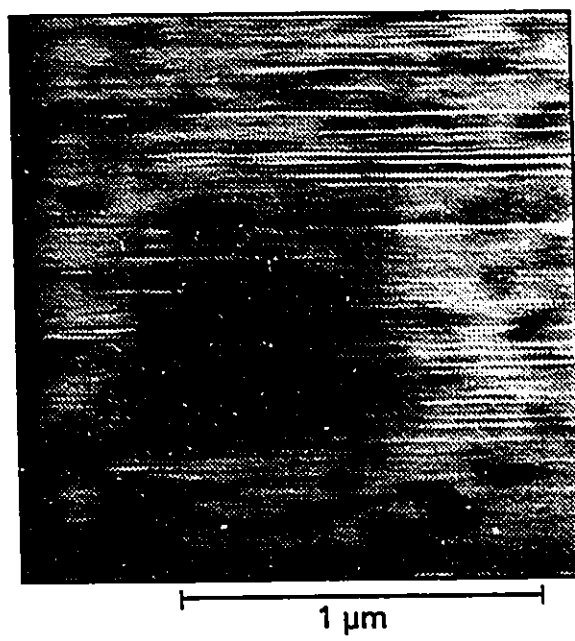


Figure 6-4: HPTCDE Langmuir-Blodgett monolayer on mica imaged with force of 10 nN. Three different heights were observed using the Park Scientific AFM.

Figure 6-4

HPTCDE perylene on mica

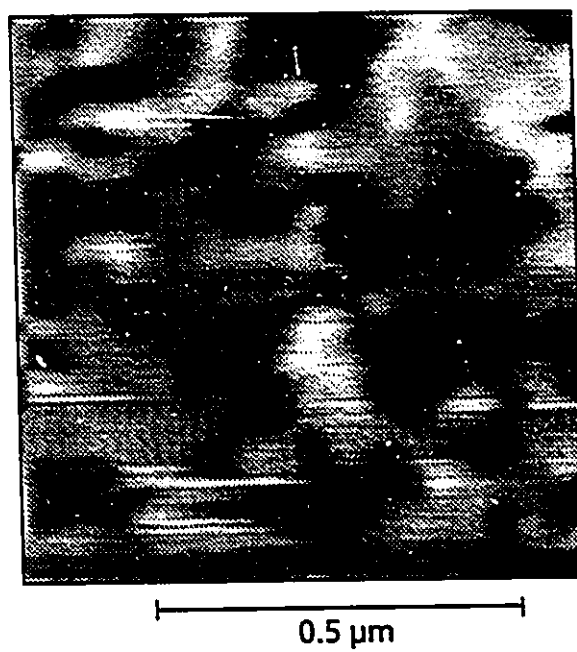


Figure 6-5: FTIR spectra of HPTCDE in the carbonyl stretching region. The transmission and reflection spectra show the change in relative intensity of the symmetric and anti-symmetric C=O stretches.

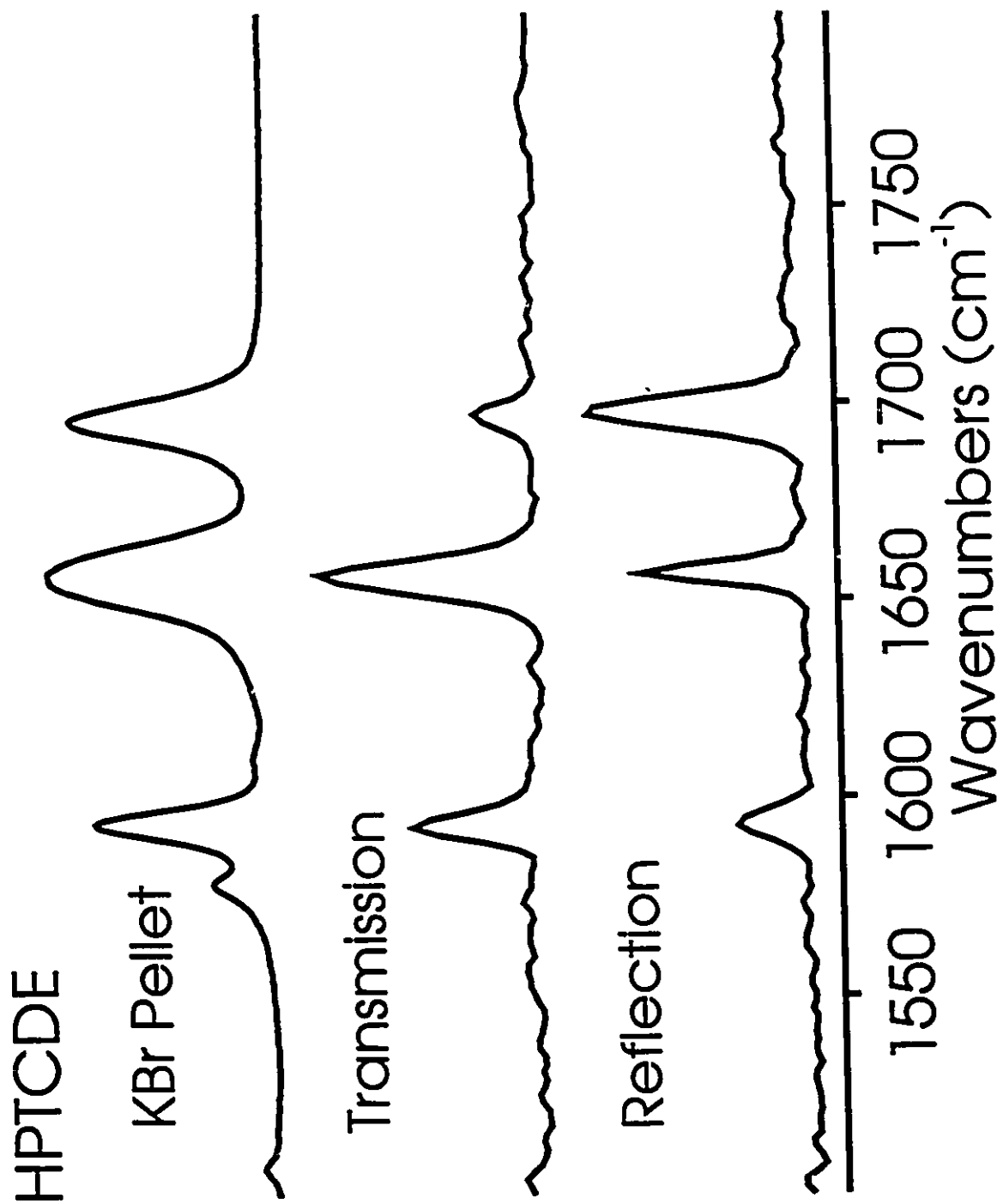


Figure 6-5

$$\frac{A_T}{A_R} = \frac{\sin^2\phi}{2m_z\cos^2\phi + m_x\sin^2\phi} \quad \text{equation 6.1}$$

A_T and A_R are the measured IR absorbance for transmission and reflectance and are normalized to the number of LB layers. m_z and m_x are enhancement factors for light which is polarized normal (z) and parallel (x or y) to the surface. In the RAIRS experiment, $m_x < m_y$ yielding equation 6.2.

$$\frac{A_T}{A_R} = \frac{\tan^2\phi}{2m_z\cos^2\phi} \quad \text{equation 6.2}$$

A method for estimating m_z based on a hypothetical ratio of A_T/A_R for isotropic films has been reported^{42,43}. For HPTCO, the tilt angles with respect to the surface normal were 36 degrees and 64 degrees for the long and short axis respectively. For HPTCDE, the values for the same tilt angles were 60 and 80 degrees respectively. These head-on molecules would form a monolayer about 2 nm in height. The image of the LB monolayer of HPTCDE on Si(111) appears in Figure 6-6. The 1.0 μm scan shows that the film is not homogeneous and there are some voids present.

The transfer ratio of HPTCO to Si(111) by z-deposition was 1.1. At the transfer pressure of 15 mNm⁻¹, the area per molecule was 0.31 nm² taken from the surface pressure-area isotherm. The limiting area⁴² obtained for this molecule using the low compressibility region of the isotherm was 0.24 nm².

Figure 6-7 is the 1.0 μm image of HPTCO. An island structure of HPTCO occurs rather than a continuous film. Assuming that the film formed on Ag is also an island film, it can be concluded that the molecular orientation occurs within the islands of the LB film.

The transfer ratio of $(\text{BuO})_8\text{H}_2\text{Pc}$ to Si(111) by z-deposition was 0.71. At the transfer pressure of 15 mNm^{-1} , the area per molecule was 0.87 nm^2 from the surface pressure-area isotherm. Ordered LB multilayers of octa-*n*-alkoxyl phthalocyanines such as $(\text{BuO})_8\text{H}_2\text{Pc}$ were fabricated on glass and described by others previously⁴⁵. A value of 0.71 nm^2 per molecule was reported⁴⁵ at a surface pressure of 30 mNm^{-1} . X-ray diffraction patterns for some octa-*n*-alkoxy phthalocyanines corresponded to the maximum molecular dimension with the plane of the Pc molecule orthogonal to the substrate⁴⁵. Figure 6-8 is the AFM image of the $(\text{BuO})_8\text{H}_2\text{Pc}$ monolayer on Si(111). The mean surface roughness was low at 0.180 nm .

The transfer ratio of $(t\text{-bu})_4\text{H}_2\text{Pc}$ to Si(111) was 1.3 by z-deposition. The area per molecule at 8 mNm^{-1} was 0.44 nm^2 extrapolated from the surface pressure-area isotherm. Baker and co-workers reported the preparation and properties of tetra-*tertiary*-butyl metal-free phthalocyanine⁴⁶. Kovacs *et al.*⁴⁷ provided further evidence of ordered true monolayers with a perpendicular distance between adjacent molecules of 0.334 nm , 0.547 nm between molecules in the stacking direction and 1.715 nm as the overall in-plane length of the Pc molecule. The structure and morphology of a related material, copper tetra-*tertiary*-butyl phthalocyanine has been investigated using transmission electron microscopy, transmission electron diffraction, X-ray

Figure 6-6: AFM image of HPTCDE Langmuir-Blodgett monolayer on Si(111) wafer. Nanoscope III SPM.

Figure 6-6

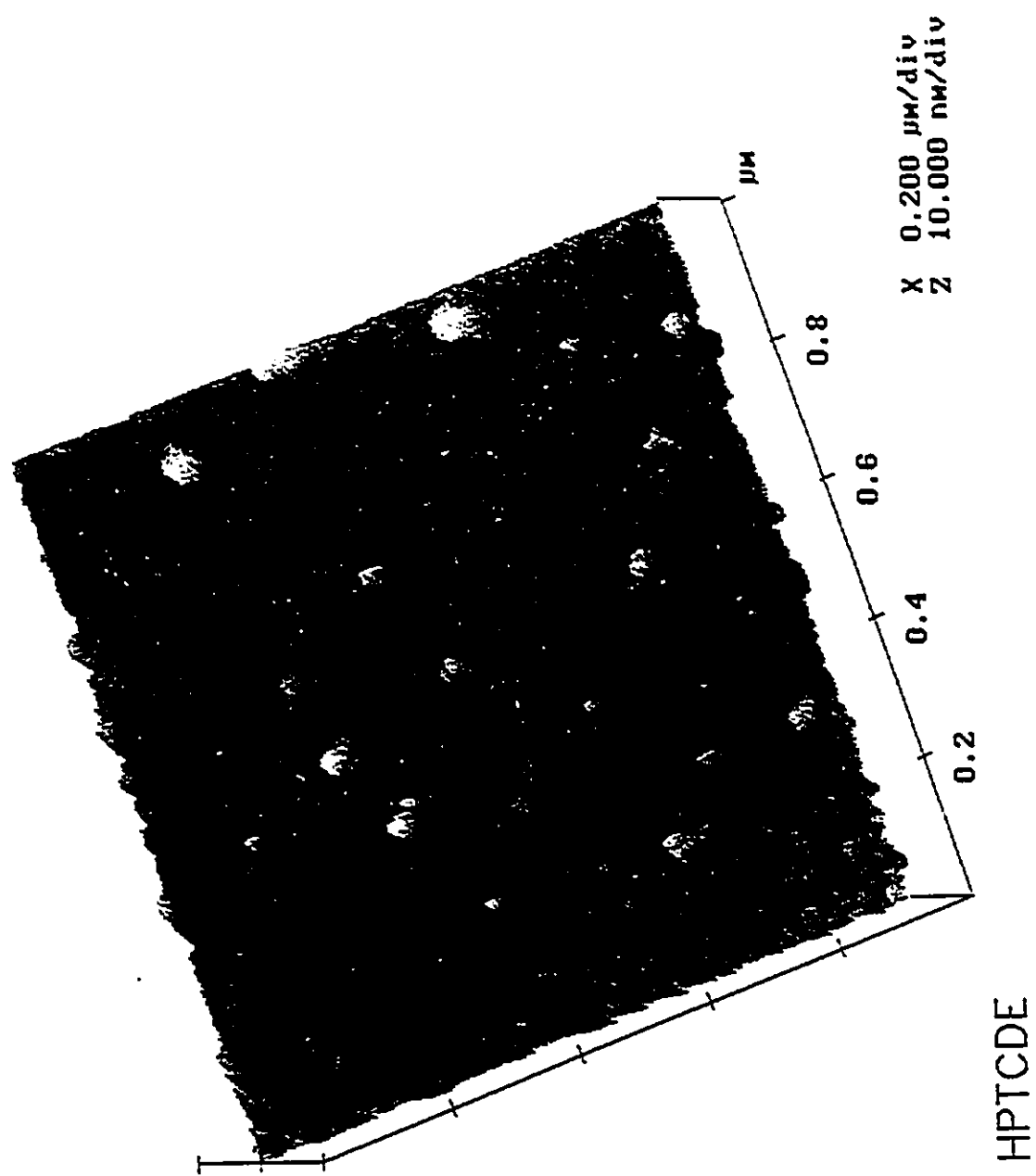
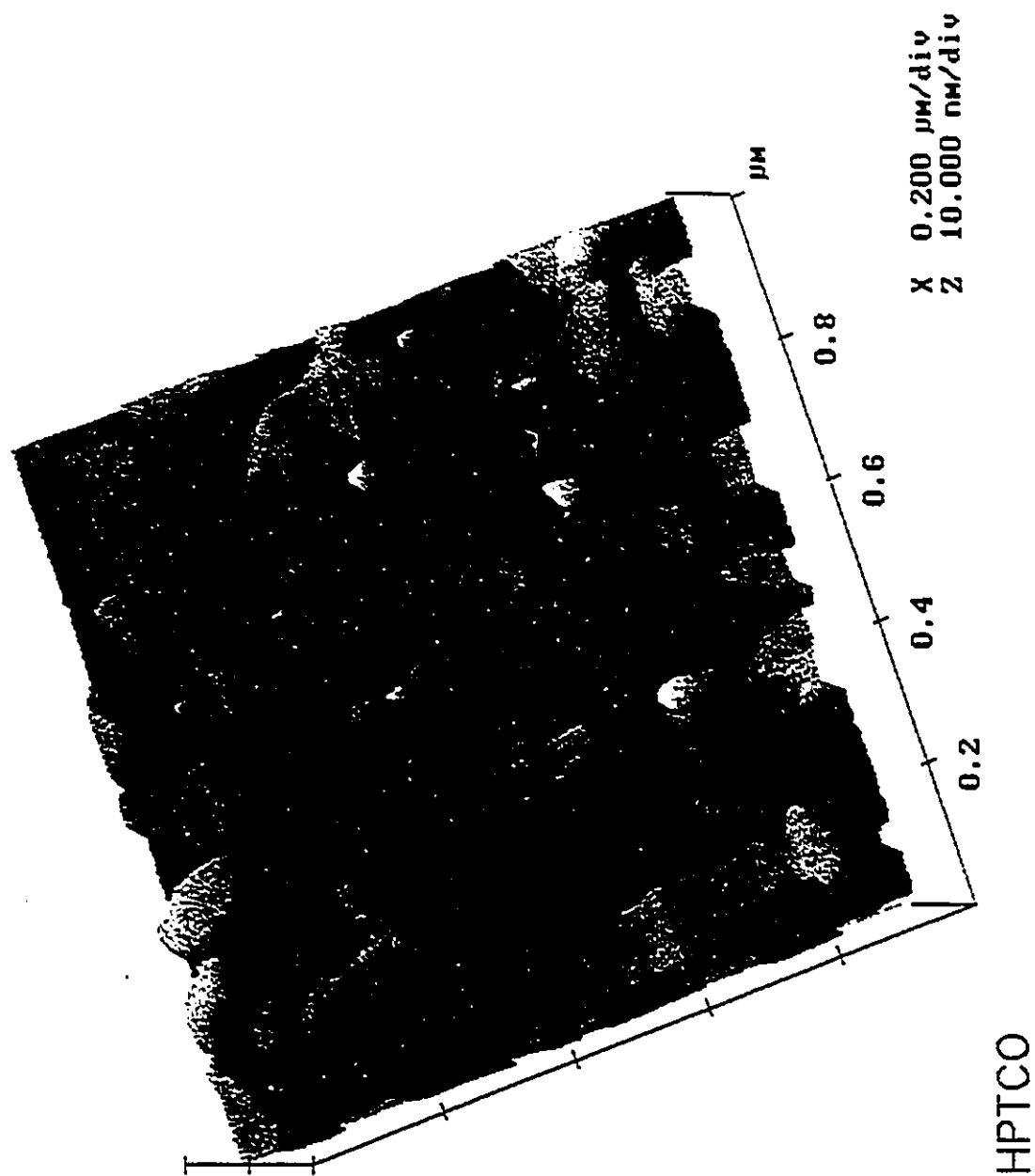


Figure 6-7: AFM image HPTCO Langmuir-Blodgett monolayer on Si(111) wafer. Nanoscope III SPM.

Figure 6-7



diffraction and light microscopy⁴⁸. The transmission electron diffraction patterns of Cu(t-bu)₄Pc had two perpendicular periods corresponding to 0.332 nm and 1.8 nm⁴⁸. Computer-based molecular modeling and a simulation suggested a zig-zag packing for the most frequent isomers⁴⁸. The AFM image of a (t-bu)₄H₂Pc Langmuir-Blodgett monolayer appears in Figure 6-9. Some voids are present but there are regions where the (t-bu)₄H₂Pc is continuous.

The factors affecting lateral resolution of the AFM for LB films have been considered by others^{49,50}. The contact diameter for repulsive mode AFM was calculated taking into account the applied force, tip radius, Young's modulus and Poisson's ratio⁴⁹. Adhesive forces between the tip and the sample increase the contact diameter and decrease the resolution when operating in the contact mode⁴⁹. The best AFM resolution for soft organic molecules in air may be 2-3 nm with small forces applied⁴⁹. Surfaces that are imaged in air are usually covered with an adsorbed layer of water and the adhesive forces between the tip and sample may be greater than the force desired for imaging⁶. One approach to reduce this adhesive force would be to image with the tip and sample immersed in liquid⁶. In this study of LB monolayers of perylenes and phthalocyanines, the fact that molecular resolution was not observed, could be due to a large contact diameter.

Figure 6-8: AFM image of $(\text{BuO})_8\text{H}_2\text{Pc}$ Langmuir-Blodgett monolayer on Si(111) wafer. Nanoscope III SPM.

Figure 6-8

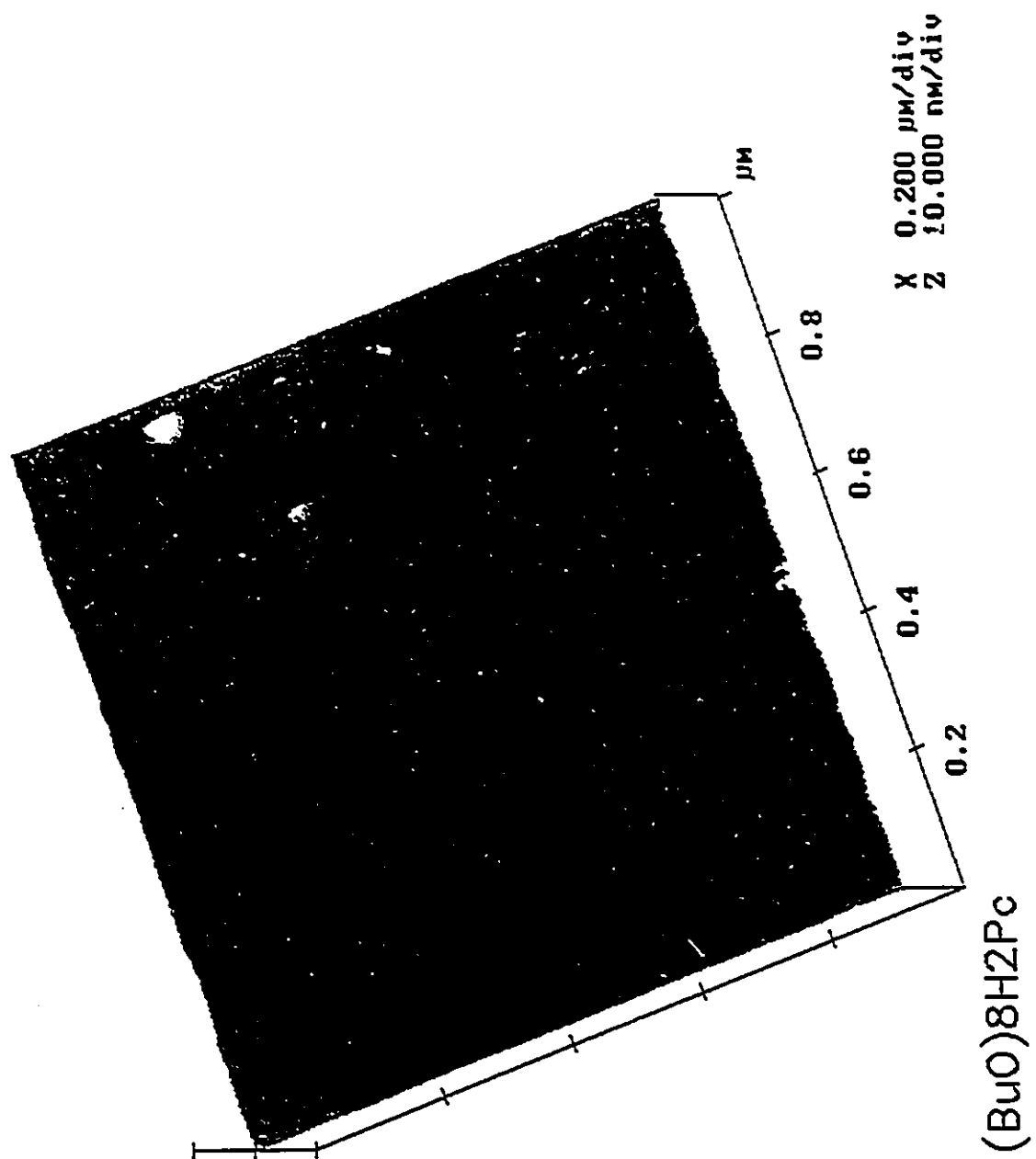
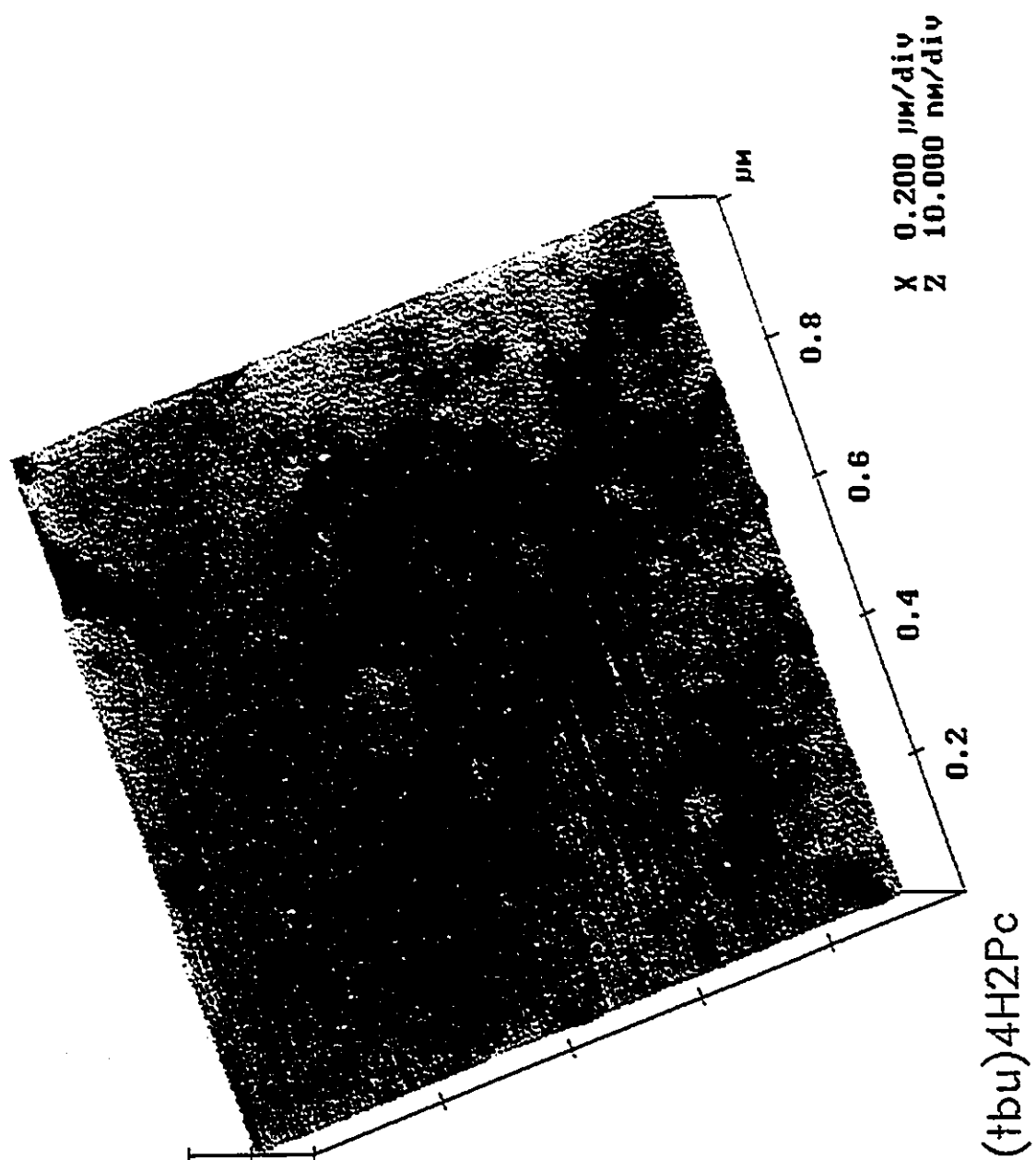


Figure 6-9: AFM image of (t-bu)₄H₂Pc Langmuir-Blodgett monolayer on Si(111) wafer. Nanoscope III SPM.

Figure 6-9



6.4. CONCLUSIONS

The AFM technique has been used to investigate the quality and surface coverage of Langmuir-Blodgett monolayers of important electroactive organic molecules on mica and Si(111) surfaces. With the AFM contact mode, it was possible to determine the monolayer height by indentation. The AFM tapping mode revealed film topography, surface coverage and voids in the nanometer regime. However, molecular resolution was not achieved. Transmission and reflection-absorption FTIR spectroscopy provided an average molecular orientation of HPTCDE with an LB monolayer height in close agreement with the value found using the AFM contact mode. It is important to point out that together, spectroscopy and AFM provide the ideal tool for structural and physical studies of LB films.

Chapter 6 References

1. Roberts, G.; in *Langmuir-Blodgett Films*, Plenum Press, New York, 1990.
2. Ulman, A.; in *An Introduction to Ultrathin Organic Films*, Academic Press, Toronto, 1991.
3. Fankuchen, I. *Phys. Rev.* **1938**, *43*, 909.
4. Bernstein, S. *J. Am. Chem. Soc.* **1938**, *60*, 1511.
- 5a. Umemura, J.; Kamata, T.; Kawai, T.; Takenanka, T. *J. Phys. Chem.* **1990**, *94*, 62.
- 5b. Frommer, J. *Angew. Chem. Int. Ed. Eng.* **1992**, *31*, 1298.
6. Drake, B.; Prater, C. B.; Weisenhorn, A. L.; Gould, S. A. C.; Albrecht, T. R.; Quate, C. F.; Cannell, I. S.; Hansma, H. G., *Science* **1989**, *243*, 1586.
7. Lippel, P. H.; Wilson, R. J.; Miller, M. D.; Woll, Ch.; Chiang, S., *Phys. Rev. Lett.* **1989**, *62*(2), 171.
8. Pester, O.; Mrwa, A.; Hietschold, M., *Phys. Stat. Sol. A* **1992**, *131*, 19.
9. Yanagi, H.; Kouzeki, T.; Ashida, M. *Langmuir* **1993**, *9*, 771.
10. Manivannan, A.; Nagahara, L. A.; Yanagi, H.; Kouzeki, T.; Ashida, M.; Maruyama, Y.; Hashimoto, K.; Fujishima, A., *Thin Solid Films* **1993**, *226*, 6.
11. Rabe, J. P.; Sano, M.; Batchelder, D.; Kalatachev, A. A., *Journal of Microscopy* **1988**, *152*(2), 573.
12. Luttrell, D. K.; Graham, J.; DeRose, J. A.; Gust, D.; Moore, T. A.; Lindsay, S. M., *Langmuir* **1992**, *8*, 765.
13. Ludwig, C.; Gompf, B.; Glatz, W.; Petersen, J.; Eisenmenger, W.; Mobius, M.; Zimmerman, U.; Karl, N., *Z. Phys. B - Condensed Matter* **1992**, *86*, 397.
14. Bar, G.; Magonov, S. N.; Cantow, H. J.; Dietrich, M.; Heinze, J., *Synth. Met.* **1991**, *41-43*, 2335.
15. Bourdieu, L.; Ronsin, O.; Chatenay, D., *Science* **1993**, *259*, 798.
16. Kuroda, R.; Kishi, A.; Yamano, A.; Hatanaka, H.; Matsuda, K.; Eguchi, K.; Nakagiri, T., *J. Vac. Sci. Technol. B.*, **1991**, *9*(2), 1180.
17. Hansma, H. G.; Gould, S. A. C.; Hansma, P. K.; Gaub, H. E.; Longo, M. L.; Zasadzinski, J. A. N., *Langmuir* **1991**, *7*, 1051.
18. Schwartz, D. K.; Viswanathan, R.; Zasadzinski, J. A. N.; *J. Phys. Chem.* **1992**, *96*, 10444.

19. Viswanathan, R.; Schwartz, D. K.; Garnæs, J.; Zasadzinski, J. A. N., *Langmuir* 1992, 8, 1603.
20. Zasadzinski, J. A. N., *Microbeam Analysis* 1991, 367.
21. Bourdieu, L.; Maaloum, M.; Silberzan, P.; Ausserre, D.; Coulon, G.; Chatenay, D., *Ann. Chim. Fr.* 1992, 17, 229.
22. Alves, C. A.; Smith, E. L.; Porter, M. D., *J. Am. Chem. Soc.* 1992, 114, 1222.
23. Edinger, K.; Golzhauser, A.; Demota, K.; Woll, Ch.; Grunze, M., *Langmuir* 1993, 9, 4.
24. Yeo, Y. H.; McGonigal, G. C.; Yackoboski, K.; Guo, C. X.; Thompson, D. J., *J. Phys. Chem.* 1992, 96, 6110.
25. Yamamoto, H.; Noguchi, M. and Tanaka, M., *Jpn. J. Appl. Phys. Pt. 2 Lett.* 1984, 23, L221.
26. Nicholson, M., *Information Display* 1984, 2, 4.
27. Riou, M.; Auregan, M.; Clarisse, C., *J. Electrochem. Soc.* 1985, 187, 349.
28. Baker, S.; Roberts, G. G.; Petty, M. C., *IEE Proc. I* 1983, 130, 260.
29. Wohltjen, H.; Barger, W. R.; Snow, A. W.; Jarvis, N. L., *IEEE Trans. Electron Devices* 1985, ED-32, 1170.
30. Clavijo, R. E.; Battisti, D.; Aroca, R.; Kovacs, G. J.; Jennings, C. A.; *Langmuir* 1992, 8, 113.
31. Souto, T.; Aroca, R.; DeSaja, J. A.; *J. Raman Spectrosc.* 1991, 22, 349.
32. Rodriguez-Mendez, M. L.; Aroca, R.; DeSaja, J. A.; *Chem. Mater.* 1993, 5, 933.
33. Fromherz, P. *Rev. Sci. Instrum.* 1975, 46, 1380.
34. Nagao, Y.; Misono, T., *Dyes Pigm.* 1984, 5, 171.
35. Moser, F. H.; Thomas, A. L. in *Phthalocyanine Compounds*, Reinhold, London, England, 1963.
36. Loutfy, R. O., *Can. J. Chem.* 1983, 61, 72.
37. Smith, K. M. in *Porphyrins and metalloporphyrins*, Elsevier Scientific Publishing Company, Amsterdam, The Netherlands, 1975.
38. Albrecht, T.R., *Ph.D. Thesis*, Stanford University, 1989.
39. Brindley, G.W.; Brown, G., in *Crystal Structures of Clay Minerals and Their X-Ray Identification*, Mineralogical Society, London, 1984.

40. Klein, C.; Hurlburt, Jr., C. S., in *Manual of Mineralogy*, John Wiley & Sons, Toronto, 1977.
41. Drexler, E.; Peterson, C.; Pergamit, G., in *Unbounding the Future: the nanotechnology revolution*, Morrow and Co. Inc., New York, 1991.
42. Johnson, E.; Aroca, R. *J. Phys. Chem.* (submitted).
43. Umemura, J.; Kamata, T.; Kawai, T.; Takenaka, T. *J. Phys. Chem.* **1990**, *94*, 62.
44. Hansen, W. N. *J. Opt. Soc. Am.* **1968**, *58*, 380.
45. Cook, M. J.; Dunn, A. J.; Daniel, M. F.; Hart, R. C. O.; Richardson, R. M.; Roser, S. J. *Thin Solid Films* **1988**, *159*, 395.
46. Baker, S.; Petty, M. C.; Roberts, G. G.; Twigg, M. V.; *Thin Solid Films* **1983**, *99*, 53.
47. Kovacs, G. J.; Vincett, P. S.; Sharp, J. H.; *Can. J. Phys.* **1985**, *63*, 346.
48. Kalvoda, L.; Brynda, E., *Thin Solid Films* **1993**, *232*, 120.
49. Weihs, T. P.; Nawaz, Z.; Jarvis, S. P.; Pethica, J. B., *Appl. Phys. Lett.* **1991**, *59*, 3536.
50. Burnham, N. A.; Dominguez, D. D.; Mowery, R. L.; Colton, R. J., *Phys. Rev. Lett.* **1990**, *64*(16), 1931.

CHAPTER 7: OVERALL SUMMARY, CONCLUSIONS AND FUTURE OUTLOOK

7.1 Overall Summary and Conclusions

A discussion and conclusions have been presented in the experimental sections: Chapter 4, Chapter 5 and Chapter 6. The key points will be summarized here.

Phthalocyanines and perylenes are important charge generation materials which are used in organic photoreceptors. Several crystalline polymorphs exist for titanyl phthalocyanine and vanadyl phthalocyanine. The polymorphic form is affected by heating, solvents and processing conditions. X-ray powder diffraction is commonly used to identify polymorphs and it has been shown that FT-Raman spectra can be used to distinguish polymorphs. Polymorphs exhibit different physical properties and photosensitivity. FT-Raman spectra were presented for four TiOPc reference materials that had previously been identified by X-ray powder diffraction. Films of titanyl phthalocyanine were vacuum evaporated onto glass held at -30°C to 240°C. The TiOPc was amorphous from -30°C to room temperature and pure type II TiOPc was present from 102°C to 240°C. FT-Raman spectra were collected of vacuum evaporated vanadyl phthalocyanine deposited on glass substrates held from -30°C to 240°C. The vanadyl phthalocyanine is amorphous at room temperature and at 240°C is type II. FT-Raman frequencies of both TiOPc and VOPc were assigned based on information from model compounds and other phthalocyanines. It was therefore, demonstrated that FT-Raman spectroscopy could be applied to thin solid vacuum evaporated films.

Since the Raman scattering intensity is weak for thin solid films, surface-enhanced Raman scattering was used to increase the intensity in the near-IR. Molecular modeling suggested a number of metals should give SERS using 1064.1 nm excitation. Copper and gold metal island films were prepared and characterized as FT-SERS substrates. The enhancement factor was approximately 100. It was initially shown that FT-SERS could be obtained for 3 nm vacuum evaporated phthalocyanine and perylene films on metal island structures. FT-SERS was then demonstrated for single Langmuir-Blodgett monolayers on copper and gold island films. The experimental results suggested the organic materials were physisorbed on the metal island films with electromagnetic enhancement. Surface-enhanced resonance Raman spectra were presented for comparison using visible laser excitation.

The trend in the experimental work was to study thin solid films on smaller and smaller scales. Thin vacuum evaporated films were studied, then Langmuir-Blodgett monolayers and finally the atomic force microscope was used to characterize the structure of the LB monolayers. Langmuir-Blodgett monolayers of two perylenes, HPTCDE and HPTCO were transferred to atomically flat substrates of mica and Si(111) wafers. For comparison, a transmission infrared spectrum and a reflection-absorption infrared spectrum were measured of a monolayer of HPTCDE on IR substrates. The HPTCDE film on mica had three regions of different thicknesses measured using the AFM with the step height $1.83 \pm .34$ nm in agreement with the orientation inferred from transmission IR and RAIRS measurements. If the force on the sample is too great the LB monolayer can be scraped from the film. Four different LB monolayers on Si(111) were examined using a tapping mode AFM. The materials considered were HPTCDE, HPTCO, CuTTPc and $(\text{BuO})_8\text{H}_2\text{Pc}$.

Molecular resolution was not obtained. The AFM was an excellent probe for local defects in the LB films. In contrast, techniques such as X-ray diffraction and infrared spectroscopy give results averaged over an area of sample. An advantage of AFM over STM is that lower force can be exerted on the sample and a conductive sample is not necessary.

7.2 Future Prospects

Returning to the model calculations of SERS enhancement factors at 1064.1 nm for various metals reported in Table 3-2, it can be seen that other elements than copper and gold should produce FT-SERS of a similar magnitude. The calculations were carried out for a specified set of input parameters including morphology. Future modeling could be done with different morphologies. An optimum morphology for FT-SERS enhancement could be selected and the challenge would be to experimentally produce these structures. This author carried out some limited experiments to check the morphology of 20 nm mass thickness vacuum evaporated films of indium, vanadium, chromium and aluminum on glass that had been held at 200°C during deposition. Electron micrographs revealed closely packed spheres of less than 0.15 microns diameter for indium. The 20 nm mass thickness chromium consisted of isolated somewhat spherical structures on glass with a typical diameter of about 0.3 microns. There was a lot of space between the centers of the spherical structures. The 20 nm mass thickness vanadium on glass had a distribution of shapes ranging from spherical to cubic with a lot of space between the centers. The aluminum film consisted of closely packed spheres of less than 0.15 microns diameter. It was assumed that an aluminum oxide layer was formed on removal from the vacuum chamber.

The future of FT-Raman spectroscopy can be considered. It is expected that Raman spectroscopy in general will be used more routinely as a complementary technique to infrared spectroscopy. The major advantage of FT-Raman spectroscopy compared to normal Raman spectroscopy is reduced fluorescence. Also since some materials absorb in the visible region, it may be desirable to collect data away from resonance. There presently are many infrared digital libraries available for compound identification. In the near future it is expected Raman digital libraries will be common. Computer-assisted spectral interpretation and intelligent systems have been applied to infrared data bases and should be useful for Raman data sets. FT-Raman results reported in the experimental section were obtained using the 1064.1 nm Nd/YAG laser line. If materials still exhibit fluorescence at this wavelength there is an opportunity to move to an even longer wavelength with a Nd/YLF laser. Reduced fluorescence can be compromised for a gain in scattering intensity if the shorter wavelengths of a tunable Ti-sapphire laser are used. FT-Raman will have applications for on-line measurements or remote sensing.

Atomic force microscopy and scanning tunneling microscopy have become popular for examining local structures on the micron to nanometer scale. Whenever an LB film is prepared, its properties must be characterized before it can be used in an application. AFM could be applied to mixed monolayers to determine if aggregates are formed or a homogeneous mixture. There appears to be some interest in the literature towards self-assembled monolayers and organized structures¹. In practice, these materials may be easier to fabricate than Langmuir-Blodgett films and fit in with the idea of nanotechnology and building structures from the bottom-up. Two examples of self-assembled structures are self-assembled vesicles to deliver drugs and a

self-assembled sandwich of electronically active materials¹. The STM can also be used to move molecules and atoms and could be used to fabricate structures from the bottom up.

Chapter 7: References

1. Service, R. F., *Science* **1994**, *265*, 316.

Appendix I: Sample output of the prolate enhancement factor for (t-bu)₄H₂Pc on a gold hemi-spheroid

THE VALUE OF ϵ_0 IS 1.00.
 THE WAVELENGTH OF LASER EXCITATION IS 1064.1 NM.
 THE WAVELENGTH OF SCATTERED LIGHT IS 1148.0 NM.
 THE SPECTRAL SHIFT IS 686.8 WAVENUMBERS.
 THE DIELECTRIC CONSTANT AT THE LASER WAVELENGTH IS $-48.787 + 3.637I$.
 THE DIELECTRIC CONSTANT AT THE SCATTERING WAVELENGTH IS $-58.634 + 4.781I$.
 THE LENGTH OF THE SEMI-MAJOR AXIS IS 38.0 NM.
 THE LENGTH OF THE SEMI-MINOR AXIS IS 33.0 NM.
 THE ASPECT RATIO OF THE PROLATE SPHEROID IS 1.15.

DISTANCE FROM TOP OF SPHEROID (NM)	ENHANCEMENT FACTOR
0.00	0.155E+03
0.50	0.135E+03
1.00	0.118E+03
1.50	0.103E+03
2.00	0.911E+02
2.50	0.806E+02
3.00	0.716E+02
3.50	0.639E+02
4.00	0.572E+02
4.50	0.513E+02
5.00	0.463E+02
5.50	0.419E+02
6.00	0.380E+02
6.50	0.345E+02
7.00	0.315E+02
7.50	0.289E+02
8.00	0.265E+02
8.50	0.244E+02
9.00	0.225E+02
9.50	0.208E+02
10.00	0.193E+02
10.50	0.179E+02
11.00	0.167E+02
11.50	0.155E+02
12.00	0.145E+02
12.50	0.136E+02
13.00	0.128E+02
13.50	0.120E+02
14.00	0.113E+02
14.50	0.107E+02
15.00	0.101E+02
15.50	0.957E+01
16.00	0.907E+01
16.50	0.862E+01
17.00	0.820E+01

Appendix I continued:

Sample output of the prolate enhancement factor for (t-bu)₄H₂Pc on a gold hemi-spheroid

DISTANCE FROM TOP OF SPHEROID (NM)	ENHANCEMENT FACTOR
17.50	0.781E+01
18.00	0.745E+01
18.50	0.711E+01
19.00	0.680E+01
19.50	0.651E+01
20.00	0.624E+01
20.50	0.599E+01
21.00	0.576E+01
21.50	0.554E+01
22.00	0.534E+01
22.50	0.514E+01
23.00	0.496E+01
23.50	0.479E+01
24.00	0.463E+01
24.50	0.448E+01

VITA AUCTORIS

Carol Ann Jennings was born in 1958 in Toronto, Ontario. She graduated from Alderwood Collegiate Institute in 1977. From there she went to the University of Toronto where she obtained a B.Sc. in Chemistry in 1981. From 1982-1984 she held a position at the University of Toronto. During 1985-1986 she completed a M.Sc. in Chemistry at the University of Windsor. She became a member of the research staff at Xerox Research Centre of Canada in 1986. During 1989 to 1990 she successfully completed three graduate courses at the University of Waterloo in polymer chemistry as a part-time special student. In 1990 she entered a Ph.D. program as a part-time student at the University of Windsor. In May of 1994 Carol transferred from the Xerox Research Centre of Canada to the Research and Technology group of Xerox Graphics Systems. She expects to complete all the requirements for a Ph.D. in 1994.